THESIS FOR THE DEGREE OF DOCTOR OF PHILOSOPHY

Non-covalent Modification of Graphene and MoS_2

Synthesis and Characterization of Charged Molecules and Two-Dimensional Materials

STEFFEN BRÜLLS

Department of Chemistry and Chemical Engineering

CHALMERS UNIVERSITY OF TECHNOLOGY

Gothenburg, Sweden 2020

Non-covalent Modification of Graphene and MoS_2
Synthesis and Characterization of Charged Molecules and Two-Dimensional Materials

STEFFEN BRÜLLS
ISBN: 978-91-7905-334-5

Doktorsavhandlingar Chalmers tekniska högskola
Nya serie nr 4801
ISSN0346-718X

Department of Chemistry and Chemical Engineering
Chalmers University of Technology
SE-412 96 Gothenburg
Sweden
Telephone + 46 (0)31-772 1000

Cover:
Graphical representation of four selected cationic molecules embedded between graphene/MoS_2. Steffen Brülls in collaboration with the artist Susanne Brix.

Printed by Chalmers Reproservice
Gothenburg, Sweden 2020

Non-covalent Modification of Graphene and MoS_2

Synthesis and Characterization of Charged-Molecules and Two-Dimensional Materials

Steffen Brülls

Department of Chemistry and Chemical Engineering
Chalmers University of Technology

Abstract

Graphene is a material of superlatives. It has unique properties, which are explored in various areas of interdisciplinary research. Graphene can improve the properties of other materials or even give them new functions and is therefore a suitable candidate for different sensor applications. While covalent functionalization of graphene comprises the outstanding properties of graphene, non-covalent modification of graphene does not affect the outstanding properties of graphene. Next to graphene there are other two-dimensional materials such as molybdenum disulfide in the focus of research, which increases the scope of applications for two-dimensional materials.

This thesis presents the synthesis of a series of neutral and charged π-conjugated systems with a different amount of either benzimidazole or pyridine moieties. The molecules differ in the size of their π-conjugated system, the amount of charges, and the counter ions. Selected molecules were used to non-covalently functionalize either graphene or molybdenum disulfide. The new two-dimensional materials were characterized by Raman spectroscopy, X-ray photoelectron spectroscopy, photoluminescence spectroscopy, atomic force microscopy and Time-of-Flight secondary ion mass spectrometry. Both, neutral and charged molecules can interact with graphene/ molybdenum disulfide *via* intermolecular forces. Computational studies support experimental observations and helped to gain more insight about the intermolecular attraction between the π-conjugated systems and graphene. Lastly, the non-covalently functionalized graphene was used to fabricate FET-devices, which showed strong p-doping of the underlying graphene by the π-conjugated systems.

To summarize, we showed the non-covalent functionalization of graphene and molybdenum disulfide with π-conjugated molecules and the influence of structural and electrochemical parameters on the interaction with graphene or molybdenum disulfide. The results presented in this thesis can be the basis of novel sensors on the nanoscale such as a pH-meter or a humidity sensors.

Keywords: Graphene, molybdenum disulfide, functionalization, intermolecular interactions, cation, anion, charged π-conjugated systems, non-covalent interactions, doping, sensors.

List of Publications

This thesis is based on results from the following publications that will be referred to their Roman numerals in the text.

I. **Evidence for Electron Transfer between Graphene and Non-covalently Bound pi-Systems.** Steffen M. Brülls, Valentina Cantatore, Zhenping Wang, Pui Lam Tam, Per Malmberg, Jessica Stubbe, Biprajit Sarkar, Itai Panas, Jerker Mårtensson, Siegfried Eigler, *Chem. Eur. J.* **2020**, *26*, 6694-6702. DOI: 10.1002/chem.202000488

II. **Interaction between Non-covalently Bound mono-, tri- and hexacationic π-conjugated Systems and Monolayer Graphene**. Steffen M. Brülls, Valentina Cantatore, Pui Lam Tam, Per Malmberg, Elisabet Ahlberg, Itai Panas, Siegfried Eigler, Jerker Mårtensson, *Manuscript in preparation.*

III. **Fluorescent pi-conjugated Hexacations for Moleculare Doping of Monolayer MoS_2.** Steffen M. Brülls, Philipp Rietsch, Zhenping Wang, Qing Cao, Jerker Mårtensson, Siegfried Eigler, *Manuscript in preparation.*

IV. **Fluorescence of a chiral pentaphene derivative derived from the hexabenzocoronene Motif**. Philipp Rietsch, Jan Soyka, Steffen Brülls, Jasmin Er, Katrin Hoffmann, Julia Beerhues, Biprajit Sarkar, Ute Resch-Genger, Siegfried Eigler. *Chem. Commun.* **2019**, *55.* 10515-10518. DOI: 10.1039/c9cc05451k

Contribution Report

The author has made the following contribution to the papers:

I. Lead author. Formulated the research problem, designed the study together with S.E. and J. M.. Synthesis, characterization and purification of all molecules. Synthesis of two-dimensional materials, coordinating experimental work and performed analysis (AFM, Raman spectroscopy). Wrote the majority of the manuscript and analyzed the results together with S.E. and J. M..

II. Lead author. Formulated the research problem, designed the study together with S.E. and J.M.. Synthesis, characterization and purification of all molecules. Synthesis of two-dimensional materials, coordinating experimental work and performed analysis (Raman spectroscopy, cyclic voltammetry). Performed the DFT calculations under supervision of V.C.. Wrote the majority of the manuscript and analyzed the results together with S.E. and J.M..

III. Lead author. Formulated the research problem, designed the study together with S.E.. Synthesis, characterization and purification of all molecules. Synthesis of two-dimensional materials, coordinating experimental work and performed analysis (Raman spectroscopy, PL spectroscopy). Wrote the majority of the manuscript and analyzed the results together with S.E..

IV. Co-author. Contributed to the outline of the study. Synthesis, characterization and purification of some molecules (40%). Contribution to the synthesis part of the manuscript.

Related publications, not included in the thesis:

1. **Organic Electron Acceptors Comprising a Dicyanomethylene-Bridged Acridophosphine Scaffold: The Impact of the Heteroatom**. T. A. Schaub, S. M. Brülls, P. O. Dral, F. Hampel, H. Maid, M. Kivala, *Chem. Eur. J.*, **2017**, *23*, 6988-6992.
   DOI: 10.1002/chem.201701412

2. **On-tissue Chemical Derivatization of Catecholamines Using 4-(*N*-methyl) Pyridinium Boronic Acid for ToF-SIMS and LDI-ToF Mass Spectrometry Imaging.** I. Kaya, S. M. Brülls, J. Dunevall, E. Jennische, S. Lange, J. Mårtensson, A. G. Ewing, P. Malmberg, J. S. Fletcher, *Anal. Chem.* **2018**, *90*, 22, 13580-13590.
   DOI: 10.1021/acs.analchem.8b03746

3. **Metal-Organic Frameworks with Hexakis(4-carboxyphenyl)benzene-Extensions to Reticular Chemistry and Introducing Foldable Nets.** Francoise M. Amombo Noa, Erik Svensson Grape, Steffen M. Brülls, Ocean Cheung, Per Malmberg, A. Ken Inge, Christine J. McKenzie, Jerker Mårtensson, Lars Örström, *J. Am. Chem. Soc.* **2020**, *142*, 20, 9471-9481.
   DOI: 10.1021/jacs.0c02984

List of Abbreviations and Acronyms

2D	Two-dimensional
Å	Ångström (10^{-10} m)
ACN	Acetonitrile
AFM	Atomic force microscopy
BF_4^-	Tetrafluoroborate anion
°C	Degree centigrade
calc.	Calculated
CASTEP	Cambridge Serial Total Energy Package (basis set in DFT)
Cl^-	Chloride anion
CV	Cyclic voltammetry
CVD	Chemical vapor deposition
DCM	Dichloromethane
DDQ	2,3-Dichloro-5,6-dicyano-1,4-benzoquinone
δ	Chemical shift (NMR)
d	Doublet (NMR)
equiv.	Equivalents
FET	Field-effect transistor
F_4TCNQ	2,3,5,6-tetrafluoro-7,7,8,8-tetracyanoquinodimethane
FWHM	Full width at half maximum
g	Gram
GGA	Generalized gradient approximation (functional in DFT)
h	Hour
HBC	Hexa-*peri*-hexabenzocoronene
HPB	Hexaphenyl benzene
HRMS	High-resolution mass spectrometry
I^-	Iodide anion
J	Coupling constant (NMR)
l	Liter
μ	Micro (10^{-6})
m	Meter, milli (10^{-3}); multiplet (NMR)
MALDI	Matrix-assisted laser desorption/ionization

MSI	Mass spectrometry imaging
min	Minute
Mp	Melting point
MS	Mass spectrometry
m/z	Mass-to-charge ratio
n	Nano (10^{-9})
NADH	Nicotinamide adenine dinucleotide
NMR	Nuclear magnetic resonance spectroscopy
OTf^-	Triflate anion
oxo-G	Graphene oxide with defined surface structure
PAH	Polycyclic aromatic hydrocarbon
PBE	Perdew-Burke-Ernzerhof (functional in DFT)
PL	Photoluminescence
ppm	Parts per million
PVA	Polyvinyl alcohol
q	Quartet (NMR)
r-oxo-G	Reduced graphene oxide with defined surface structure
s	Second; singlet (NMR)
t	Triplet (NMR)
TCNE	Tetracyanoethylene
TCNQ	7,7,8,8- tetracyanoquinodimethane
THF	Tetrahydrofuran
ToF-SIMS	Time-of-flight secondary ion mass spectrometry
TTF	Tetrathiafulvalene
XPS	X-ray photoelectron spectroscopy

Table of Contents

Page

1. Introduction and Background

1.1 Graphene - Material of Superlatives

The material graphene is in the centre of a fast growing interdisciplinary field of research between natural sciences and material sciences.[1] It is also the best studied two-dimensional material (2D).[2] Graphene research focuses on applications in nanotechnology and device fabrication.[2-5] In 2004, the researchers Andre Geim and Konstantin Novoselov from the University of Manchester published the *Scotch* tape procedure for the preparation of graphene. Single layers of graphene were obtained by exfoliating graphite crystals. Their analyses of single-layer graphene reviled some of its outstanding properties like the highest yet known charge carrier mobility value.[6] In recognition to this research, Andre Geim and Konstantin Novoselov were honored with the Nobel Prize in Physics in 2010.[7-8] Graphene is one of the thinnest material ever obtained and at the same time the strongest known material.[9] Its electrical[10] and thermal conductivity[11] are higher than in any other material. Graphene is elastic and impermeable to any molecules[12] and almost transparent.[13] These unique properties can be explained by the structure of graphene.[14] The 2D-material consists of a one-atom-thick layer of solely carbon atoms, arranged in a honey comb lattice with a C-C bond length of 1.42 Å (Figure 1).

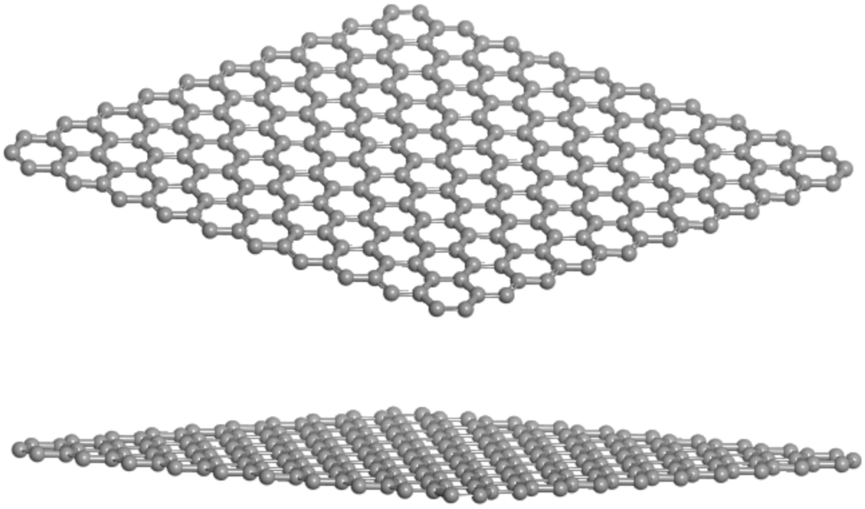

Figure 1: Optimized structures of single-layer graphene from two different perspectives in top view (top) and side view (bottom), showing the hexagonal arrangement of the carbon atoms in the lattice.

When stacked on top of each other, several sheets of graphene form the material graphite with an interlayer distance of 3.35 Å.[15] All carbon atoms in the graphene lattice are sp^2-hybridized as in some other carbon allotropes like fullerenes[16] and carbon nanotubes.[17] However, not all sp^2-hybridized carbon allotropes have the same properties. Because of graphene's structure and associated properties, graphene is expected to be a promising candidate for many applications in the future.[18-22] Its broad spectrum of unique properties allows graphene to be used in a series of different applications, including amongst others high-frequency transistors,[23] highperformance capacitors,[24] transparent electrodes,[25] sensors[26-29] and energy applications.[30-31] Different chemical modifications of the carbon materials fullerenes[32-35] and carbon nanotubes [36-38] have been published. These studies show that the electronic properties of carbon allotropes can be influenced by modifying the carbon lattice chemically. Recently, an increased interest in chemical modification of graphene can be observed to overcome problems in production, storage, handling and processing. The modification of graphene changes its electronic[39-41] and photoelectrical properties[42] and has an impact on the solubility and stability of the material.[43-49] In addition to the already mentioned challenges, pristine graphene has properties that makes it less favourable for some interesting electronic applications. Semiconducting materials profit from a high stability in high frequency, high power, high temperature and other harsh environmental conditions. A wide band gap semiconductor in comparison is defined with a band gap greater than 2.2 eV[50] between valence band (VB) and conduction band (CB) like the materials silicon carbide and gallium nitride (third generation of semiconductors, Figure 2B). The band gap describes the energy difference between the valence band of electrons and the conduction band in insulators and semiconductors. It is therefore the amount of energy, which is required to excite a valence electron of an atom to a conduction band to move free in the crystal lattice as a charge carrier. The literature explains for metals an overlapping of the valence band (VB) and conduction band (CB; Figure 2A). The energy level between VB and CB is called Fermi level E_f. In contrast, graphene has a zero band gap (Figure 2C). That means that the Fermi level E_f of graphene is at the Dirac point, which is the crossing-point between valence band and conduction band. In recent years there has been an increased interest in the engineering of the band structure of graphene to open up the band gap.[51] Both p- and n-doping of graphene are feasible methods to introduce a semiconducting gap to graphene based materials, which is called band gap opening. This can be done by single atom doping, chemical modification and electrostatic field tuning. n-doping occurs when the dopants transfer one or more electron (electron donor) to graphene and the dopant molecules are therefore reduced and may become neutral. That leads to an increased Fermi level E_f of graphene (E_f lies in conduction band of the material). The conductivity of the doped material is increased because the transferred electron is fed into the conduction band of graphene. In an analogue fashion, p-doping materials accept one or more electrons (electron acceptor) and leave a hole in the valence band of graphene, corresponding to a decrease of its Fermi level E_f (Figure 2D) and band gap opening. The dopant becomes less positive or neutral. The positively charged holes are consequently the charge carriers in p-doped materials.[52]

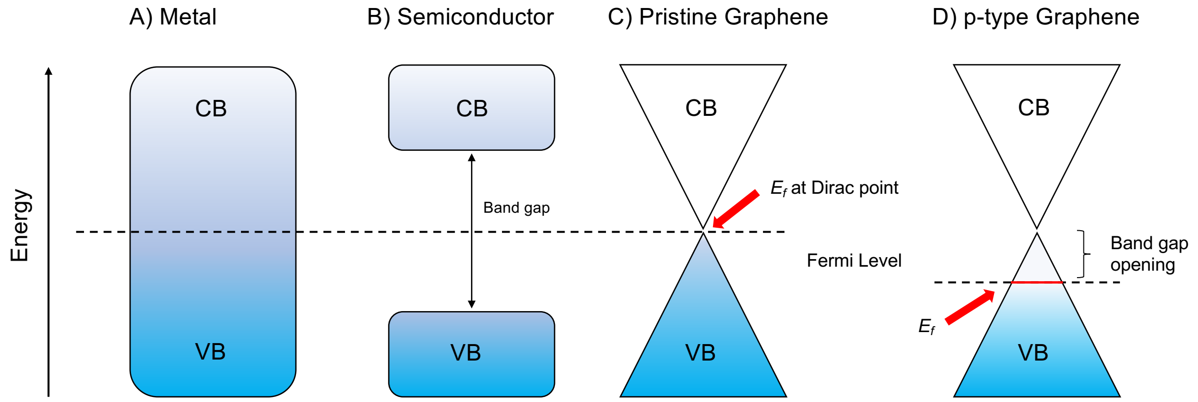

Figure 2: Schematic band structures with the respective valence (VB) and conduction band (CB) of A) a metal with band overlapping, B) a semiconductor with a band gap, C) pristine graphene with a zero bandgap and D) p-type graphene with band gap opening. Pristine graphene has its Fermi level E_f at cross-over point (Dirac point), while the Fermi level E_f is lowered for positively charged graphene.

1.2 Two-Dimensional Materials

Next to the already mentioned graphene, other 2D materials such as layered double hydroxides,[53] molybdenum disulfide (MoS_2) or more general transition metal dichalcogenides (TMDs),[54] black phosphorus,[55] arsenene, antimonene and bismutene,[56] have been described in the literature. These materials have various elemental compositions, which influence their structure as well as their chemical and physical properties. In the same fashion as graphene, there is a boom in research focusing on the tuning of these materials. Depending on the future type of applications, different 2D materials can be chosen and combined and graphene may not be the first choice, but one component. Most semiconducting applications are handicapped by the already mentioned zero-band gap in pristine graphene. Another promising 2D material, however with a band gap is molybdenum disulfide.[57] Molybdenum disulfide is one member of the layered transition metal dichalcogenides.[58] In the general formula MX_2 of TMDs, M refers to a transition metal (elemental group IV to VI) and X to a chalcogen like sulfur, selenium or tellurium.[59] One layer of molybdenum atoms is sandwiched between layers of sulfide ions (Figure 3). One single layer of molybdenum disulfide is 6.5 Å thick.[60] Crystalline MoS_2 exists in both hexagonal and rhombohedral symmetry, and for both symmetries are the molybdenum atoms in the center of a trigonal prismatic coordination sphere and bonded to six sulfide ions. In contrast, the sulfur atoms have a trigonal pyramidal geometry and are each bonded to three molybdenum atoms.[61] Analogously to the link between graphene and graphite, several layers of molybdenum disulfide can stick on top of each other to form molybdenite (bulk MoS_2). The layers are held together by van der Waals interactions, in a similar way as in graphite. Similar to graphene and graphite, the optical and electronic properties of monolayered MoS_2 and bulk MoS_2 however differ.[62-67] For example, transforming bulk MoS_2 to monolayer MoS_2 leads to an increase of the direct bandgap from 1.29 eV to 1.90 eV.[68-69] In a similar way to graphene can the unique properties of MoS_2 be used for potential applications in emerging technologies like solar cells,[70-75] detectors [76-81] and sensors.[82-86]

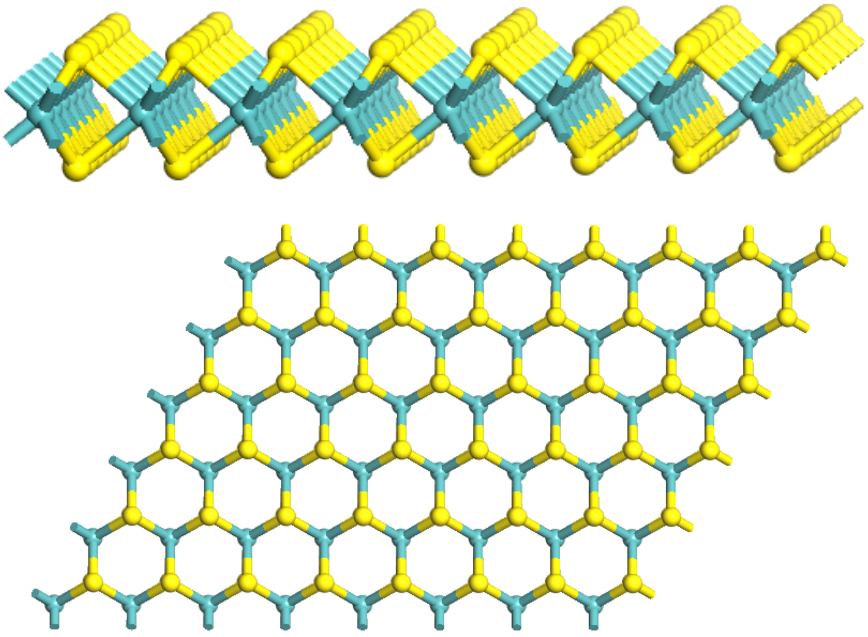

Figure 3: Three-dimensional optimized structures of MoS_2 from two different perspectives (yellow: sulfur atoms, blue: molybdenum atoms). The side view (top) shows the Mo-S bridge site and top view (bottom) shows the hexagonal arrangement of the sandwiched molybdenum layer.

1.3 Functionalization of Two-Dimensional Materials

The functionalization of 2D materials introduces new chemical and physical properties. This allows the properties of two-dimensional materials to be tailored to best satisfy the requirements set by sought-after technologies and applications. Graphene can be modified[52] by covalent bonding of molecules to the graphene or by non-covalent bonding of molecules on the surface of graphene (Figure 4).[40] Covalent modification of graphene can be performed by single atom doping[52] or addition of molecules to its unsaturated structure (i.e. functionalization with diazonium reagent). Both can result in truncation of the conjugation system of graphene that compromises some of its outstanding properties. In contrast, the structure of graphene remains in a first approximation unaffected when modified non-covalently.

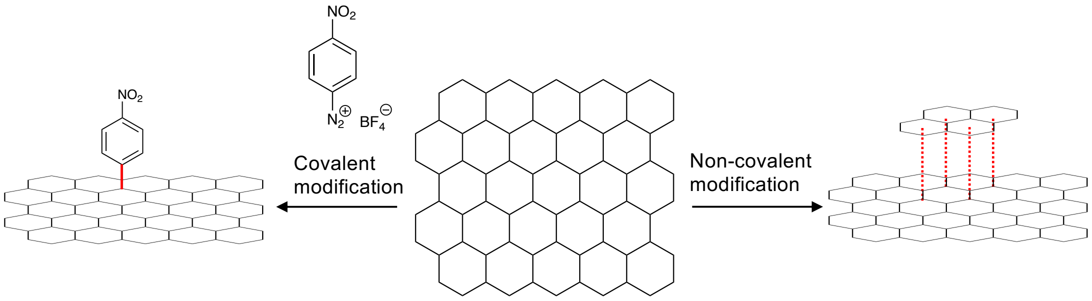

Figure 4: Schematic representation of covalent functionalization for graphene with diazonium reagent (left side) and non-covalent functionalization of graphene with pyrene (right side, dotted line).

The advantage of the non-covalent modification is that it can be used when a preservation of the high conductivity is required.[40] The best studied chemically modified derivative of graphene is graphene oxide. It is a 2D material related to graphene and consists of a hexagonal σ-framework of carbon atoms, which is functionalized with oxo-functional groups such as epoxy-, hydroxyl, carbonyl- and carboxyl-groups. No exact structure or chemical formula can be given for graphene oxide since it depends on the manner in which the graphene oxide is prepared.[87] The first step of the preparation of graphene oxide is the oxidation of graphite, followed by an aqueous work-up and purification to isolate graphite oxide. In a last step, a delamination process forms single layers of graphene oxide from graphite oxide.[88] During the oxidation process defects are introduced in the carbon lattice of the formed graphene oxide.

All three previously mentioned polymorphs of molybdenum disulfide have different physical properties and therefore already the different synthesis approaches have an dramatical impact on the properties of MoS_2[89] by creating defects or introducing negative charges to the lattice. Even a pressure dependency of the quality of MoS_2 during the synthesis process of CVD MoS_2 was studied.[90] The surface modification is another strategy to tune the properties of MoS_2 in a similar way to other layered transition metal dichalcogenides (TMDs). This can be performed in a similar fashion to graphene in both a non-covalent and a covalent approach.[91] This field of research however needs greater exploration. Doping of MoS_2, particularly chemical, is highly versatile to control its optical properties.[92] The intensity of the photoluminescence[89] of MoS_2 can be tuned by surface functionalization of single layer MoS_2 with for example p-type dopants.[92]

Currently, there are a number of applications of functionalized graphene and MoS_2. Both unmodified graphene[26-29] as well as non-covalently modified graphene[93-97] have been used for sensor applications. By non-covalently attaching a maltose-aminopyrene derivative on graphene, the protein concanavalin A has been detected selectively and with high sensitivity.[97] In another application, a material with electrocatalytic activity was assembled by non-covalent adsorption of a water-soluble iron porphyrins on graphene.[93] Also the non-covalent adsorption of Prussian blue on graphene gave materials with high electrocatalytic activity.[94] This growing research area however benefits from novel molecules suitable for the non-covalent modification of graphene. In addition, the non-covalent interaction between adsorbent and graphene has to be studied in more depth. MoS_2 behaves here in a similar way. Both pristine[98] and modified MoS_2 were used for sensor applications.[99-101] and the effect of molecular doping of MoS_2 was computational studied. [102] The controlled exfoliation of MoS_2 was used to develop thin film humidity sensors[103] and MoS_2 nanoparticle hybrid materials were used as a electrochemical sensing platform to detect bisphenol A.[104] This highlights the versatility of these interesting class of materials.

2. Theory and Methodology

2.1 Preparation of Two-Dimensional Materials

The two materials discussed in this thesis, graphene and MoS_2, can be synthesized by different methods. The following sections will discuss the most prominent methods for the preparation of these two-dimensional materials containing the mechanical cleavage of both graphite,[6, 105] and molybdenite,[106-110] the reduction of graphene oxide[111] and the chemical vapor deposition (CVD) of graphene[112-113] and MoS_2.[110, 114-117]

2.1.1 Mechanical Cleavage of Graphite and molybdenite

Several attempts have been performed to prepare graphene by exfoliation during writing with a graphite pencil.[118-124] However this method produced graphitic films (several layers of graphene) which behave like bulk graphite. And the extraordinary properties of graphene are just present in monolayers of graphene.[6] Andre Geim and Konstantin Novoselov were the first to exfoliate single-layer graphene from bulk graphite by using a tape of the brand *Scotch* suitable for device preparation.[6] The process of this so-called *Scotch* tape method is as follows. At first, the adhesive tape is pressed (Figure 5A) against the bulk graphite to transfer few layers of graphene to the tape (Figure 5B). The tape, now with the few layers of graphene is transferred (Figure 5C) by pressing the tape against the substrate surface of choice and gently peeling the tape off (Figure 5D). In this way, a single layer of atoms is achieved. It has been shown that graphene on top of a SiO_2/Si substrate can be detected under an optical microscope due to a strong color contrast arising from the air-graphite-SiO_2 interface.[125-126] For the exfoliation of MoS_2 bulk material, the literature gives various approaches, which are in principle similar to the exfoliation of graphite.[106-110]

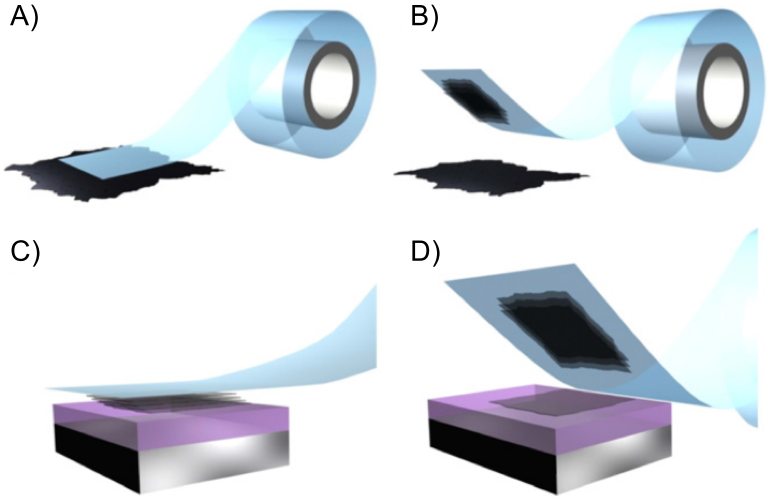

Figure 5: Mechanical exfoliation of graphene with the Scotch tape method.[127] Reprinted with permission.

2.1.2 Reduction of Graphene Oxide

Graphene oxide is a 2D material like its analogue graphene. It consists of a hexagonal σ-framework of carbon atoms that is decorated on both sides with oxo-functional groups, such as epoxy-, hydroxyl, carbonyl- and carboxyl-groups at edges (Scheme 1).[128] The oxo-functionalized graphene oxide (oxo-G) can be applied to a silica wafer (Si/300nm SiO_2) *via* the Langmuir-Blodgett technique[129] and further treated with reducing agents to potentially produce a high quality of graphene. It has been shown that black graphene-derived materials can be produced from yellowish graphene oxide by the use of different reducing agents.[130] The density of lattice defects of reduced oxo-functionalized graphene (r-oxo-G) can be determined with statistical Raman spectroscopy.[131] It is however hard to quantify the efficiency of the chemical reduction of graphene oxide with too many defects. Also, the graphene surface can be contaminated by reaction byproducts/residues. Another way of reducing graphene oxide is the thermal disproportionation.[132] Here are mobile oxo species formed, which might etch already existing lattice defects in the material. Thermal reduction of graphene also avoids the introduction of impurities from the reducing agents.

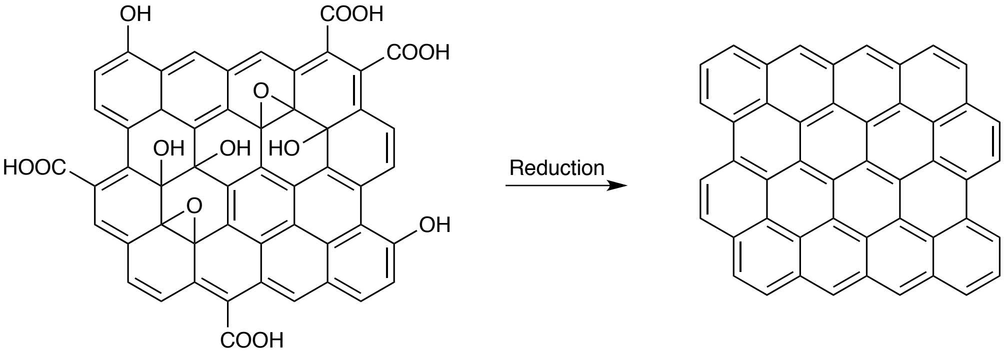

Scheme 1: Reduction of graphene oxide removes the oxo-functionalities to obtain graphene .

2.1.3 Graphene Preparation by Chemical Vapor Deposition

Chemical vapor deposition (CVD)[112, 133] is one of the most favored techniques to produce graphene of a high quality on surfaces. CVD graphene neither suffers from in-plane vacancy defects nor oxo-functional groups on the basal plane, although grain boundaries are present.[112] The formed numbers of layers of graphene as well as the formation mechanism changes by using different transition metals[112-113] such as nickel,[134] palladium,[135] ruthenium,[136] iridium[137] or copper.[138] The CVD formation process is divided into three main stages. At the outset of the process is the active transition metal surface covered with native oxide (Figure 6A). Usually polycrystalline copper foils are used as substrate, since they provide a high yield of monolayer graphene. In a first step the transition metal is annealed at around 1000 °C to remove the native oxide layer. Subsequently, under a CH_4/H_2 atmosphere, graphene starts to grow at several positions on the transition metal surface (Figure 6B). In the last step neighboring graphene flakes start to touch and form grain boundaries (Figure 6C).[112] The thermal expansion coefficients of graphene and copper are different. This causes wrinkling of graphene on the copper substrate during the cooling process. Suitable alternatives to copper are germanium substrates.[139] Due to the similar thermal expansion coefficients of germanium and graphene, fewer wrinkles form upon cooling. The interaction forces between graphene and germanium are also lower than the interaction forces between graphene and copper. It is therefore easier to transfer the graphene to other substrates. CVD MoS_2 films are prepared in a similar fashion to graphene with molybdenum containing compounds, such as MoS_2 powder[117] or molybdenum based film,[114-115] and ammonium thiomolybdate films.[116]

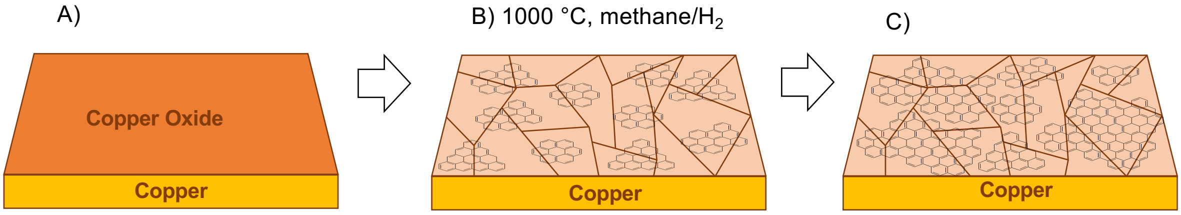

Figure 6: Illustration of CVD process in three stages. A) In the first stage the copper surface is covered with copper oxide. B) After annealing to 1000 °C under a CH_4/H_2 atmosphere, graphene starts to grow on the copper surface. C) In the last stage start the graphene flakes to touch each other and form grain boundaries.

2.2 Mechanisms

The syntheses of the molecules prepared and studied in this thesis are based on organic reactions, such as palladium catalyzed cross-coupling, nucleophilic substitution, electrophilic aromatic substitution, cyclotrimerization and condensation reactions. The cyclotrimerization reaction, the palladium catalysed cross-coupling reaction and the condensation between a carboxylic acid and a diamine were key reactions in the synthetic routes for several different molecular targets presented in this thesis and were carried out several times. However, the reaction conditions had to be adopted for each molecular target. Therefore, these reactions are described in more detail below.

2.2.1 Cyclotrimerization Reaction

The (2+2+2) cyclotrimerization reaction of alkynes is an useful synthetic strategy to construct a benzene skeleton.[140] The cyclotrimerization reaction is catalyzed by a transition metal complex with molybdenum,[141] cobalt,[142-143] rhodium,[144] or ruthenium as the metal catalyst.[145] During the cyclotrimerization reaction three chemical bonds are formed in one chemical operation.[140] A wide variety of alkynes can be transformed with the cyclotrimerization reaction. It is possible to cyclotrimerize acetylene as well as mono- and disubstituted alkynes. Depending on the catalyst, different pathways have been proposed. The mechanisms for cyclotrimerization using cobalt complexes as catalysts, mostly of the type $CpCoL_2$ (L = ligand, Cp = cyclopentadiene), has been discussed in literature (Scheme 2).[146]

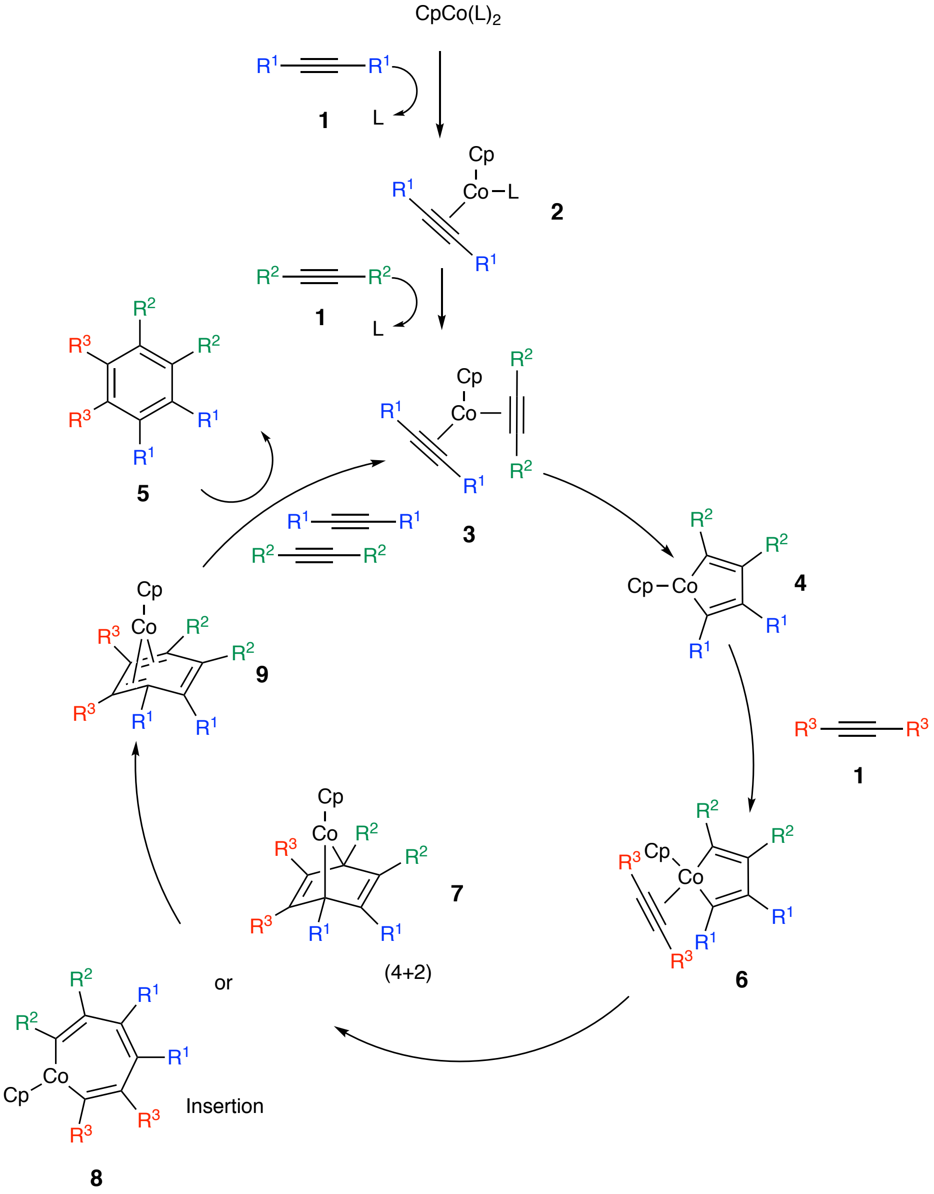

Scheme 2. Mechanism of cyclotrimerization reaction.

Density functional theory (DFT) calculations have been performed to understand the mechanism of the reaction.[147] Initially one alkyne molecule **1** forms a complex **2** with the catalyst precursor CpCoL$_2$ by substituting one of its ligands. An example of the ligand is triphenylphosphine. Then, another alkyne substitutes a second ligand in the Co-complex **2** in an activation process to form the active catalyst **3**. The active catalyst **3** undergoes an oxidative cyclization to yield the cobalt cycle **4**. The transformation of that complex into the final product **5** is not yet fully understood. However, extended Hükel theory calculations indicate the formation of **6**, where the alkyne lies parallel to the C$_\beta$-C$_\beta$ bond of the metallacycle.[148] The next step could in principle result in any of two possible intermediates. Complex **6** undergoes an (4+2) Diels-Alder reaction to form **7** or it undergoes an insertion reaction that results in complex **8**. However, complexes **7** and **8** have both been deemed unlikely based on DFT calculations.[146] The product is released from **9** by ligand exchange with two alkynes reforming the active catalyst **3**.

2.2.2 Phillips-Ladenburg Reaction

Benzimidazole is the benzo derivative of a heterocyclic aromatic compound, imidazole.[149-150] The benzimidazole core structure is a common fragment in many biological active compounds and has appeared in a variety of medical studies.[151-152] The first synthesis of benzimidazole was published in 1872.[153] A huge variety of different synthetic strategies have been describes since then.[150] In 1928 Phillips described the synthesis of benzimidazole by refluxing *o*-phenylenediamine and monobasic acid in hydrochloric acid, which is known as Phillips-Ladenburg reaction.[154] Benzimidazole was then obtained by neutralizing the reaction mixture with ammonium hydroxide. A modified version of this condensation reaction allows the formation of benzimidazole derivatives using an excess of organic acids.[155] Fatty acids and acetic acid are condensed with *o*-phenylenediamine to yield its corresponding benzimidazole derivatives. Various conditions have been reported for the condensation reaction between trimesic acid and *o*-phenylenediamine.[156-159] The strategy described in this thesis is based on the Phillips-Ladenburg reaction described by Phillips (Scheme 3).[154] But instead of hydrochloric acid, phosphoric or polyphosphoric acid were used to introduce one, three or six benzimidazole moieties in just one chemical operation. The mechanism for the reaction in both methods is the same. The mechanism of the underlying condensation reaction in polyphosphoric acid has been recently discussed. The rate determining step is the initial formation of a carboxylic acid phosphate ester. [160]

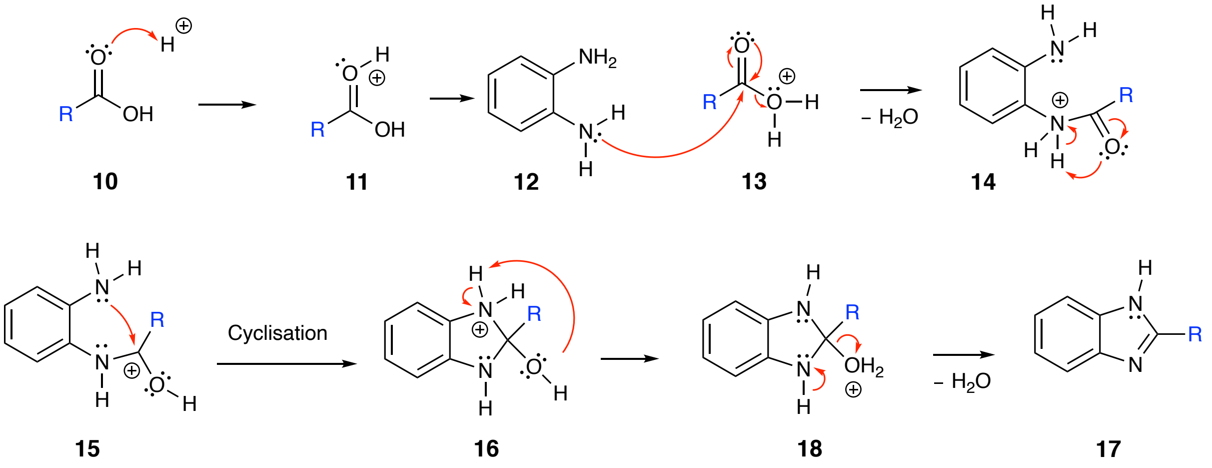

Scheme 3. Mechanism of benzimidazole formation via Phillips-Ladenburg reaction.

Initially the carboxylic acid **10** is protonated by the presence of an acid to form **11**. A nucleophilic attack of one of the amino groups of *o*-phenylenediamine **12** on the protonated acid **13** (equilibrium between **11** and **13**) leads to *N*-acylated intermediate **14**. The carbonyl group of **14** is protonated to form **15**, followed by a nucleophilic attack by the other amino group of **15** on the carbonyl carbon (The diamine of **14** and **15** are also protonated in equilibrium). This leads to a second *N*-acylation and completes the ring closure to obtain **16**. Benzimidazole **17** is formed by the dehydration of intermediate **18**. During the benzimidazole condensation reaction, two water molecules are formed.

2.2.3 Palladium-catalyzed Reactions

In Palladium-catalysed cross-coupling reactions carbon-carbon (or carbon-hetero atom) bonds are formed between the two coupling partners.[161] One coupling partner is an organic halide (or pseudo halide, e.g. tosylate or triflate) R-X (R: organic fragment, X: I, Br, Cl) and the other one is an organometallic compound R'-M (R': organic fragment, M: main group element, here palladium). In 2010 Richard F. Heck, Ei-ichi Negishi[162] and Akira Suzuki[163] were honoured with the Nobel prize in Chemistry for their development on palladium-catalysed cross coupling reactions. The Sonogashira cross coupling reaction was a key reaction in the preparation of several of the compounds discussed in this thesis.[164] The Suzuki coupling was also a significant reaction used extensively in the preparation of compounds explored in this work. The mechanism for both cross-coupling reactions can schematically be explained by the same catalytic cycle (Scheme 4).

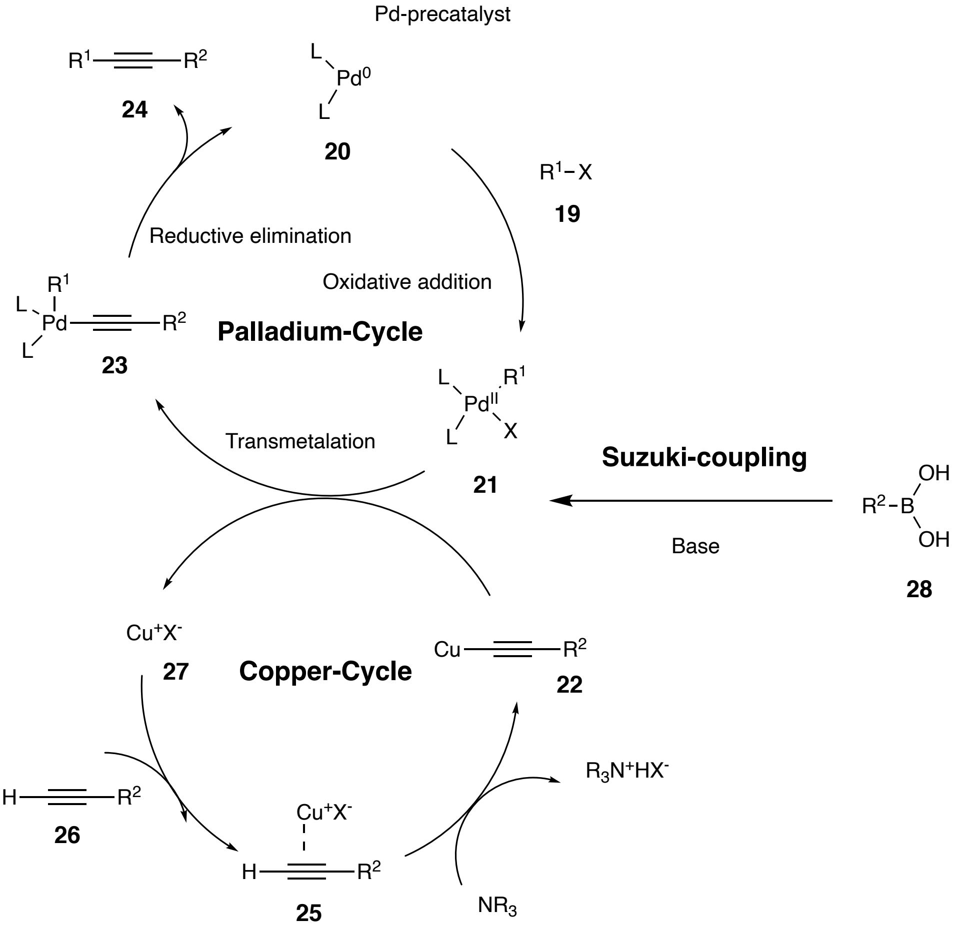

Scheme 4. General mechanism for Sonogashira and Suzuki-Miyaura reactions. L = phosphane, base, solvent, alkyne.

However, the Sonogashira cross coupling reaction used to form a carbon-carbon bond between a terminal alkyne and an aryl or vinyl halide and requires a copper co-catalyst. Thus, a second catalytic cycle where copper acts as the catalyst is connected to the palladium cycle (Scheme 4).[165-166] The reactions also require a base, as here illustrated using tertiary amine.

Other amines or inorganic bases however show a similar behavior. The initial step of the palladium-cycle is a fast oxidative addition (OA) of an aryl or vinyl halide R^1-X **19** to the active palladium-catalyst **20**. The initial palladium precatalyst is usually based on a 14-electron Pd^0L_2 in which palladium has the initial oxidation state 0. After the oxidative addition step, palladium has in the new formed complex **21** the oxidation state II. A rate-determining transmetalation between complex **21** and a copper acetylide **22**, formed in the copper-cycle, leads to a new palladium species **23**. The formation of copper acetylide **22** in the copper-cycle is explained later. The next step in the palladium-cycle is a *cis-trans* isomerization, followed by the final step, the reductive elimination from the palladium species **23** to form the internal alkyne **24** and the Pd^0- precatalyst **20**. The copper-cycle is not yet fully understood. It has been proposed that the presence of a base (here tertiary amine) removes the proton from the terminal alkyne **25** coordinated to a copper(I) ion in an η2-complex (*π*-alkyne complex).[167] This complex is formed between a terminal alkyne **26** and a copper halide **27**. However, commonly used amines are not basic enough to deprotonate the alkyne. The acidity of the acetylenic proton is increased by the π-coordination to copper(I). The copper acetylide **25** formed upon deprotonation by the base enters into the already discussed transmetalation step in the palladium-cycle above.

2.3 Intermolecular Interactions between π-conjugated Molecules

The functionalization of 2D materials allows the properties of 2D materials to be tailored to best satisfy the requirements set by sought-after technologies and applications. Graphene, as previously mentioned, can be modified[52] by covalent bonding of moieties or by non-covalent interactions.[40] In contrast to the covalent modification of graphene, the structure of graphene remains in a first approximation chemically unaffected when modified non-covalently. The advantage of the non-covalent modification is that it can be used when a preservation of the high conductivity is required.[40] The chemical cohesion is given by intermolecular forces.

Attractive intermolecular interactions can be divided into hydrogen bonding, ionic bonding, ion-dipole bonding, ion-induced dipole bonding, dipole-dipole bonding, dipole-induced dipole bonding and van der Waals forces (amongst others dispersion interactions). In comparison to intramolecular forces, that holds a molecule together, intermolecular forces are weaker (Figure 7). The van der Waals forces are based on four major contributions: the Pauli exclusion principle, Keesom interaction, Deby forces and London dispersion interactions. The Pauli exclusion principle is a quantum mechanical principle, which states that certain particles cannot be at the same place at the same time. It is therefore the origin of repulsive forces. Keesom interactions occur between a partial positive charged dipole δ^+ and another partial negative charged dipole δ^- in permanent dipoles. Hydrogen bonding interactions are a special type of dipole-dipole interaction with a strong binding affinity and orbital controlled geometry. The interaction between a permanent dipole and an induced dipole of an initially non-polar molecule results from the Deby forces. London dispersion forces occur when the electrons in an atom form a temporary dipole. This temporary dipole itself can induce a dipole in another atom and is therefore sometimes called induced dipole-induced dipole interaction. It can occur in polar and nonpolar molecules and is part of the van der Waals forces. The van der Waals interactions are omnipresent between atoms, molecules and surfaces that are close to each other. Depending on the source, Deby forces are also included in the van der Waals forces.

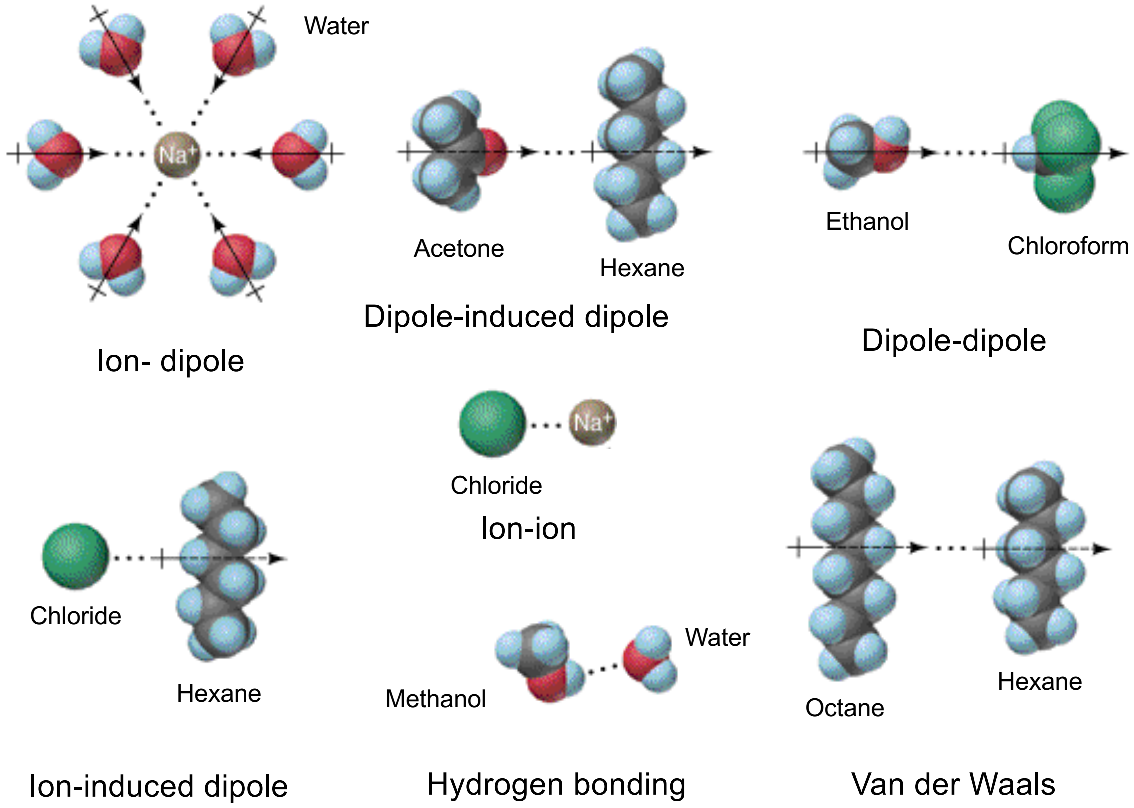

Figure 7: Overview of different intermolecular interactions between molecules and ions.[168]

Hydrogen bonds are electrostatic attractions between the lone pair on an electron rich atom (donor) such as nitrogen, oxygen or fluorine and a hydrogen atom. Hydrogen bonding between a molecule and graphene oxide sheets has been used to attach adsorbents non-covalently. The strength of a hydrogen bond depends on its binding partners, the distance and the angle.[169] Several hydrogen bonds add up to an even stronger attraction compared to a single hydrogen bond. It has been shown that nano hybrid materials can be assembled with graphene oxide and poly(vinyl alcohol) (PVA).[170] Here, the oxo-functional groups of graphene oxide interact with the hydroxyl groups of the PVA chains to form a strong hydrogen bonding network. The same phenomena have been utilized with other graphene oxide hybrid materials.[171-173] The interactions between aromatic molecules and graphene *via* aromatic interactions has been studied extensively. The dispersive versus electrostatic contributions to the total binding energies between aromatic molecules and graphene were computed. At larger distances the binding energy consists mostly of dispersive interactions, while in equilibrium bonding distance dispersive and electrostatic interactions contribute to the total binding energies between aromatic molecules and graphene.[174]

The terms π-π stacking and π-π interactions are often misleading.[175] They do not describe the forces that lead to the interaction of aromatic molecules. It has been shown that the π-electron density of most aromatic systems leads to a quadrupole moment with a partial positive charge at the boundaries and a partial negative charge above and beneath the aromatic system.[176-179] Two of these aromatic systems would therefore avoid stacking on top of each other as this would result in greater repulsion (Figure 8A). The terms π-π stacking and π-π interactions however would suggest that. Two aromatic systems with the same quadrupole moment interact *via* off-center parallel stacking (Figure 8B) or *via* edge-to-face interaction (Figure 8C). Electron-withdrawing groups on an aromatic system lead to inverse polarization, the partial negative charge at the center is relocated to the edges of the aromatic system. An electron-rich aromatic system and an electron-deficient aromatic system can therefore interact with each other *via* face-centered stacking.[180] This interaction is referred to as an aromatic donor-acceptor interaction (Figure 8D).

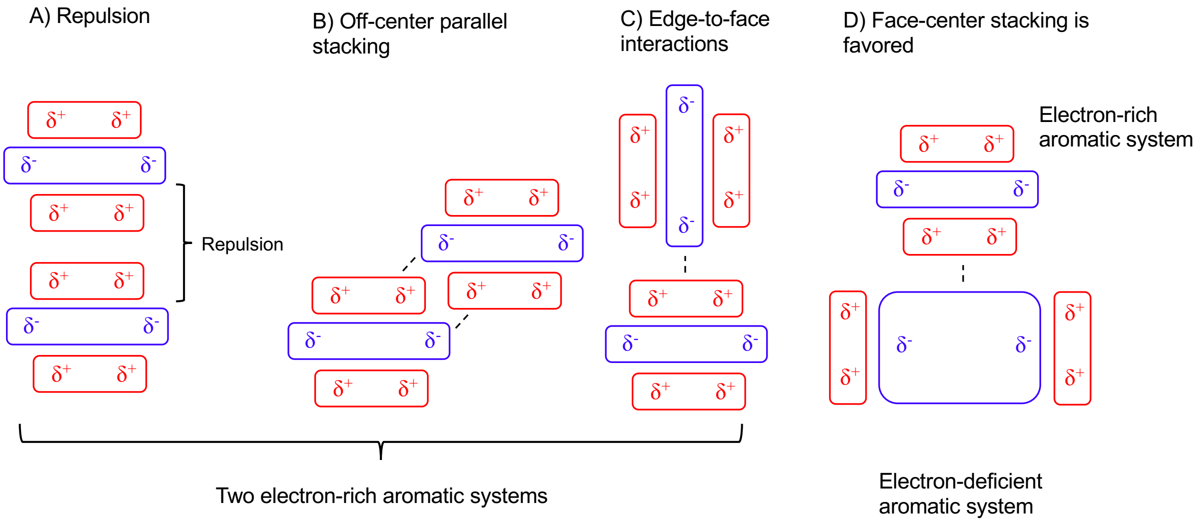

Figure 8: Possible interactions of two aromatic systems including A) the electromagnetic repulsing between the partial negative charges above and beneath an aromatic system (face-center stacking is disfavored). B) Off-center parallel stacking and C) edge-to-face interactions between aromatic systems with the same quadrupole moment. D) The interaction between an aromatic system and electron-deficient aromatic molecules via face-centered stacking.

The intermolecular interactions in hybrid materials between graphene and respective molecules have been discussed. In the following section, some recent developments and applications of graphene hybrid materials with respect to their intermolecular interactions will be discussed. Non-covalently bound fluorescein on graphene oxide and graphene samples showed a fluorescence quenching effect, which is studied by fluorescence quenching microscopy.[181] Subsequently, the fluorescein layer is removed by rinsing the graphene samples with ethanol or water and the fluorescence of the molecule itself is observed once again. In another project, biocompatible compounds like lactoferrin or chitosan were bound to both graphene oxide and graphene.[182] This introduced antibacterial properties from the native lactoferrin or chitosan to the new hybrid materials. Additionally, doping with lactoferrin helps to form stable dispersions and the fabrication of large area films by solvent evaporation techniques. Other scientists have showed that non-covalently modified graphene can also be used to build up novel electrochemical sensors. By binding a virus-specific antibody non-covalently on the surface of graphene, the functionalized material can be used to detect a pathogenic virus through antibodyantigen interactions.[183] Organic dyes comprise mostly of a π-conjugated system and can therefore interact with graphene *via* aromatic interactions. In literature, that interaction has been computational studied e.g. by a hybrid material of highly fluorescent Rhodamine 6G and graphene.[184] Graphene hybrid materials have shown promise as pH sensors. pH-sensitive materials have been assembled by non-covalently binding pyrene-terminated positively charged polymers non-covalently onto graphene.[46] These materials reveal different solubilities in both aqueous and organic solvents at different pH-values. By changing the pH-value of the material solution a precipitation of the hybrid material has been observed.

2.4 Non-covalent Modification of Graphene and MoS_2

Studies of non-covalently modified graphene by selective binding of molecules are limited. The interaction between graphene and π-conjugated molecules has been studied computationally,[185] however the literature does not yet show which parameter of the π-conjugated molecules influence the interaction with graphene. Therefore, a series of suitable molecules with structural variations needs to be synthesized to study the interaction between graphene and these π-conjugated molecules in depth. A bigger π-conjugated system is expected to interact more strongly with graphene than a molecule with a smaller surface because of larger dispersion and electrostatic interactions, which are in sum stronger than the Pauli repulsions. In the case of a cationic charged π-conjugated system, donor-acceptor interactions between the electron rich graphene and the cationic molecules are also favorable. The interaction between graphene and an electron rich π-conjugated system should be unfavorable. The amount of charges in these π-conjugated molecules should also have an influence on the interaction with graphene, since the donor-acceptor interactions are increased.

The protonation or alkylation of nitrogen atoms in benzimidazole and pyridine derivatives, can form molecules with positive charges. For different steric or solubility demands the structure of the alkyl chains can be varied. Various counterions, such as iodide (I^-), chloride (Cl^-), tetrafluoroborate (BF_4^-) and triflate (OTf^-) can be added to compensate the charge of charged π-conjugated systems, the influence of different counter-ions on the interaction with graphene can be investigated. A chemical compound containing an organic ion is an organic salt. The organic salts in this thesis are named by the following term: $(\text{name of cation})^{n+}(\text{anion})_m{}^{1-}$, were n is the amount of positive charges from the cation and m the amount of anions. Different counterions have different electrostatic interactions to their counterions. Halides like iodide and chloride coordinate strongly to their counterions while tetrafluoroborate and triflate ions are weakly coordinating. Means to control of these parameters should provide tools to specifically influence the properties of the novel non-covalently modified graphene materials. Suitable model molecules are shown in Scheme 5.

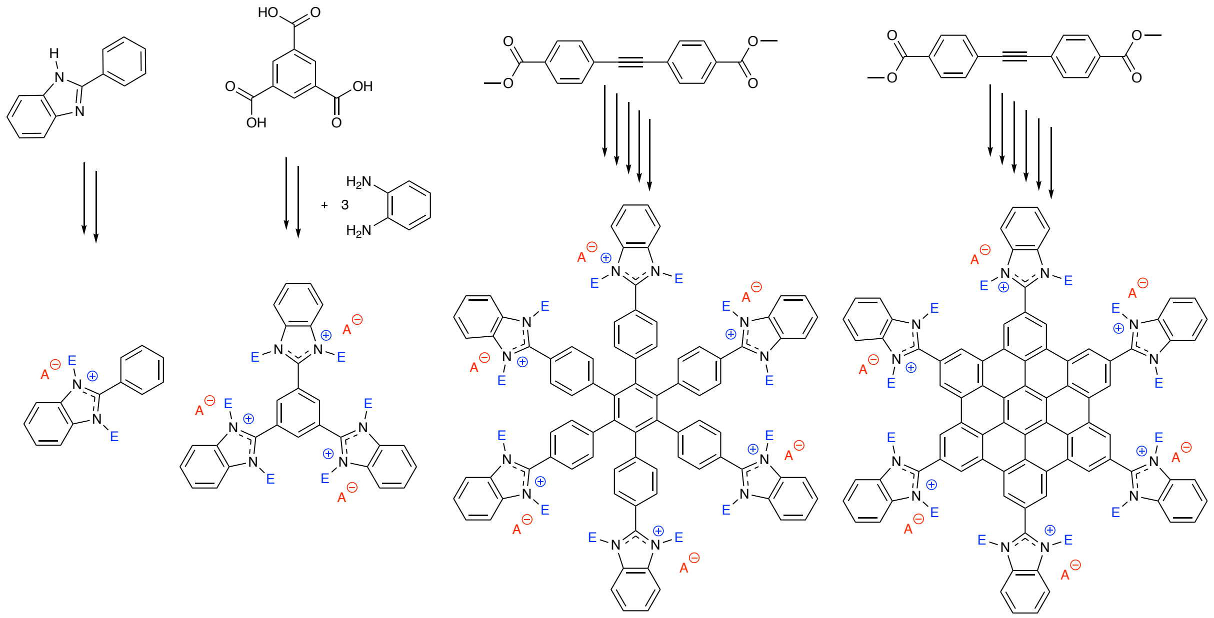

Scheme 5: Indicated synthesis of suitable model molecules to study the influence of several parameters on the interaction of these aromatic systems with graphene (E=electrophile (blue), A=anion (red)).

The salts of triflic acid result from the alkylation of methyl trifluoromethansulfonate and ethyl trifluoromethansulfonate. The triflate ion has a moderately strong binding affinity for their counter cation, but the binding is weaker than halide counter ions.[186] Tetrafluoroborate (BF_4^-) derivatives can be obtained via alkylation reactions with trimethyloxonium tetrafluoroborate and triethyloxonium tetrafluoroborate. These compounds are called "Meerwein's salts"[187-188] and are one of the strongest alkylation agents available.[186] Tetrafluoroborate anion has an even weaker binding affinity than the triflate anion. Alkylation reactions with the selected alkylating agent result in one positive charge per heteroatom in the π-conjugated system. The alkylation of three or six heteroatoms leads to trications or hexacations, respetively. It is expected that studies of graphene hybrid materials with the same cation, but various counterions will reveal information about the influence of counterions on the binding affinity of cationic π-conjugated system to graphene. As an example, changing the degree of protonation of the dopant is expected to influence the charge density of graphene. This can be used as starting point for the development of pH-sensitive sensors. These π-conjugated molecules will allow for the selective detection of protons, which is necessary for a pH sensor (Scheme 6).

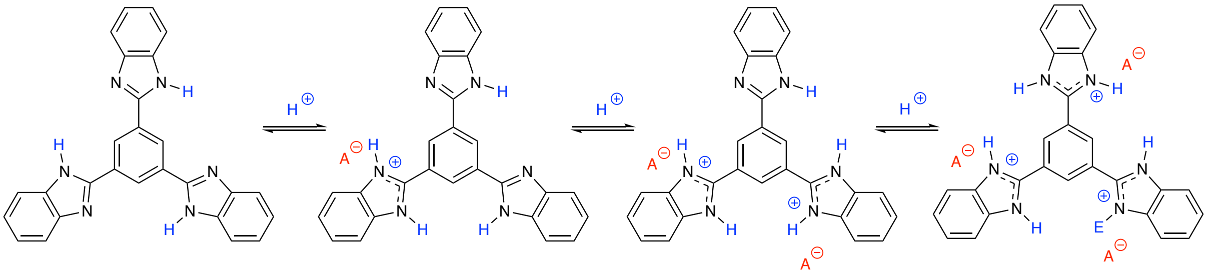

Scheme 6. Protonation of benzimidazole moieties – leading to a pH depending change of the charge density of graphene.

Hexaphenyl benzene (HPB) derivatives and its oxidized hexa-*peri*-hexabenzocoronene (HBC) derivatives are other core structures for the doping of graphene. Both, HPB and HBC systems have extended π-conjugated systems, which can interact via intermolecular forces with graphene. In contrast to most HBC derivatives, their HPB precursors are soluble and have also been intensively studied in literature.[189] HPB consists of a central benzene core surrounded by six aromatic moieties to form a nonplanar propeller-like structure.[190] The properties of unsubstituted HPB can be tailored by the substituents in *para* and *meta* positions.

Another class of polycyclic aromatic hydrocarbons are the so-called hexa-*peri*-hexabenzocoronene derivatives. Hexa-*peri*-hexabenzocoronene (HBC) is a planar graphene-like molecule, which has been well studied[191-197] and is used in organic electronics or optoelectronic devices.[198-200] HBC is a small and well defined model compound for graphene and can be amongst others computational studied as a representative of graphene. The interaction between two HBC molecules or HBC and graphene are therefore of a similar nature to the intermolecular interaction between two graphene layers in a graphite crystal. An aromatic intermolecular interaction such as dispersive and electrostatic interactions lead to self-assembly[201] and make it possible to form both graphitic nanotubes or coils from HBC derivatives (Figure 9).[202-203]

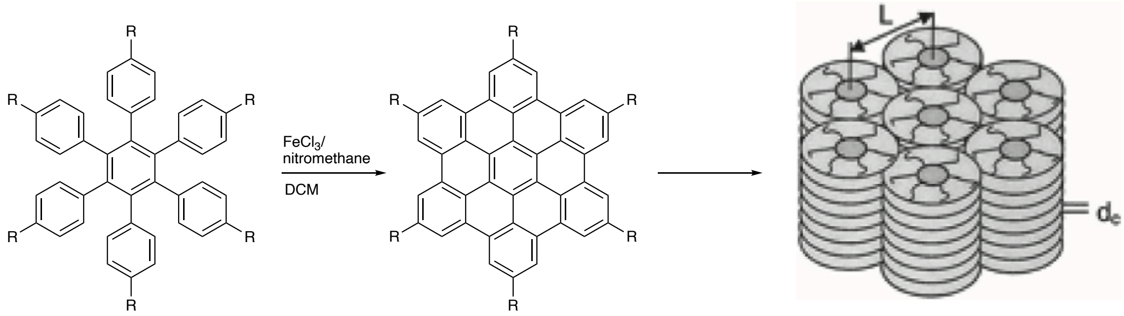

Figure 9. Schematic Synthesis of HBC derivatives with long alkyl chains (R=alkyl). The self-assembly of several HBC derivatives due to intermolecular interactions leads to graphitic nanotubes or coils.[204] Reprinted with permission.

However, the strong tendency to self-assemble is also responsible for the poor solubility of HBC derivatives in most solvents. The poor solubility makes HBC and many of its derivatives difficult to purify, analyze and characterize. However, the solubility can be greatly improved by introducing specific substituents at the periphery of HBC that prevent the self-association. Other properties of HBC, such as redox potentials, can be tuned in the same way by decorating the periphery with suitable substituents. Klaus Müllen pioneered the development of HBC derivatives. His research synthesized and characterized soluble HBC derivatives with alkyl-substitution in *para* position[192-193, 205-208] and studied also hexa-*tert*-butyl-hexa-*peri*-hexabenzocoronene **29**, a HBC derivative functionalized with six *tert*-butyl groups.[209] It has been shown that the substituents in *para* position are critical for the success of the oxidation of HPB derivatives. The Scholl oxidation has been performed with electron donating groups (EDG), as it is the case for alkyl-substituents in *para* position which makes the HPB core susceptible to oxidation by both $FeCl_3$ and 2,3-dichloro-5,6-dicyano-1,4-benzoquinone (DDQ).

In contrast, electron withdrawing groups (EWG) deactivate the π-conjugated system by lowering the HOMO energy. In that case are stronger oxidizing agents required.
While the oxidation of hexa(*p*-iodophenyl)benzene **30** to hexa(*p*-iodophenyl)-*peri*-hexabenzocoronene **31** is described ($FeCl_3$ dissolved in nitromethane), the oxidation of the bromine derivative hexa(*p*-bromophenyl) benzene **31** cannot be performed under the same conditions due to the more electron-withdrawing character of the bromines.[210] In the case of HPB derivatives with acetyl esters, a slightly electron withdrawing group, a large amount of $FeCl_3$ is necessary to oxidize the molecule.[200] Coordination of the Lewis acid to the carbonyl group of the ester makes this group even more electron withdrawing. Electron-deficient arenes bearing bromine, fluorine and CF_3 groups can be oxidized by using a mixture of the oxidant DDQ as an oxidant in combination with triflic acid.[211] The literature however does not always give a full purification or characterization details of these compounds, due to solubility issues. Recently, it has been shown that if the substituents in *para* position are very bulky, like in the case of porphyrin functionalized HPB, the oxidation of the HPB molecule does not work under the so far described conditions.[212]

3. Methods

3.1 Characterization of Molecules and Functionalized Two-Dimensional Materials

Evidence for the identity of organic molecules discussed in this thesis were collected using proton, carbon and fluorine nuclear magnetic resonance spectroscopy (NMR),[213] melting point analysis as well as high resolution mass spectroscopy (HRMS) and time-of-flight secondary ion mass spectrometry (ToF-SIMS). This thesis focuses on characterization techniques such as NMR,[213] cyclic voltammetry, UV-Vis spectroscopy, fluorescence spectroscopy, X-ray photoelectron spectroscopy,[214] Raman spectroscopy[215-218] and atomic force microscopy (AFM)[219].

3.2 Nuclear Magnetic Resonance Spectroscopy

Nuclear Magnetic Resonance (NMR) spectroscopy is a technique to determine the molecular structure and the purity of a compound or mixtures. In case of a known structure NMR spectroscopy can be used to study physical properties at the molecular level such as conformational exchange, solubility and diffusion. The Nobel Prize in Chemistry 1991 was awarded to the chemist Richard Robert Ernst for his development of Fourier transformation NMR spectroscopy.[220] The principal of NMR spectroscopy is based on the physical observation that nuclei are perturbed in a strong constant magnetic field and respond by an electromagnetic signal. The frequency of this electromagnetic signal is characteristic for the nucleus and depends on the strength of the applied magnetic field, the chemical environment of the nucleus and the magnetic properties of the studied isotope. The most commonly studied nuclei, ^{1}H and ^{13}C, contain an odd atomic mass number (number of protons and neutrons), which leads to a nuclear magnetic moment and angular momentum. These isotopes have a nuclear spin and are not NMR silent in comparison to nuclides with an even number of nuclei. The first step in an NMR experiment is the polarization of the magnetic nuclear spin in a constant magnetic field B_0. This alignment is perturbated by a radio-frequency (RF) pulse. The oscillation frequency of the RF pulse depends on the applied magnetic field B_0 and the nuclei of observation. After the RF pulse is applied. Precession of the charged nuclei occurs with the nuclei's intrinsic Larmor frequency. This does not involve the transition between spin states or energy levels.[221] The frequency of the resonance is collected and recorded as chemical shift, which describes the resonant frequency of a nucleus relative to a standard in a magnetic field. Nuclei in a different chemical environment give different chemical shifts. The NMR spectroscopy is therefore a technique to study the structure of molecules.[222] The NMR spectrometer consists of a electromagnet, which is responsible for the constant magnetic field B_0 around the NMR sample. A RF generator delivers the RF pulse to perturbate the polarization of the magnetic nuclear spin. The oscillating resonant frequency is then transferred over an amplifier to the detector and processed with a computer. The compound to be examined is dissolved in a deuterated solvent and filled in an NMR tube. Deuterated solvents are used to avoid the swamping of the solvent signal. Deuterium nuclei are NMR silent in a ^{1}H NMR experiment and do therefore not give any NMR signals.

3.3 Raman Spectroscopy

Raman spectroscopy is a fast and nondestructive characterization technique.[216, 223-228] It gives high resolution characterization of surfaces and materials such as graphene and modified graphene[215] as well as MoS_2. Raman spectroscopy can analyze, amongst others, the number of graphene layer,[229] doping,[230] chemical functionalization[231] and density of lattice defects.[131] The Raman spectrometer excites a sample with a laser beam at a specific wavelength. The light interacts with molecular vibrations of the sample. This leads to a relative shift of the photon emission with lower energies (Stokes scattering) or higher energies (Anti-Stokes scattering) than the excitation wavelength. The emitted light is detected and gives information about the vibrational modes of the sample. The Raman spectra of carbon based 2D materials show characteristic features (Figure 10).[218]

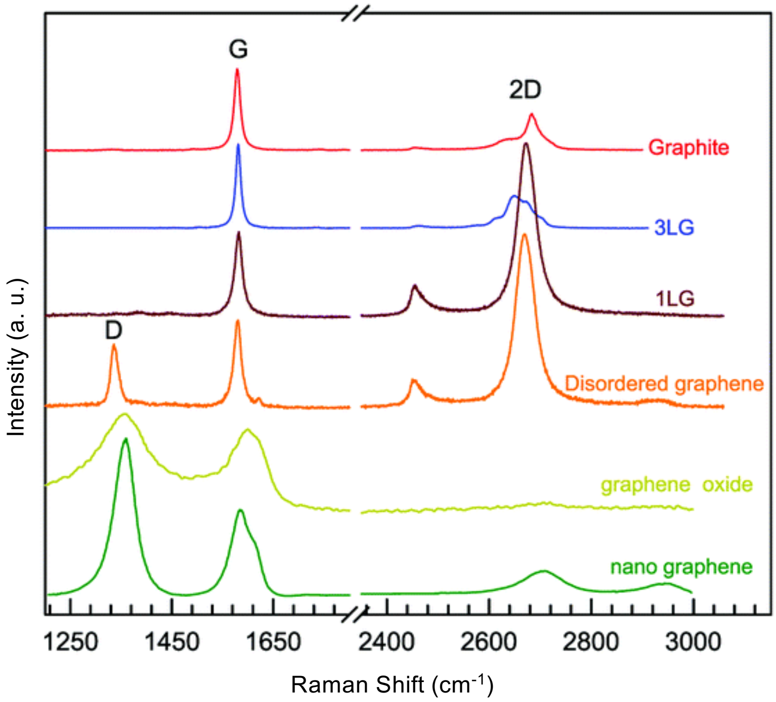

Figure 10: Raman spectra of different graphene based material including single-layer graphene (1LG).[216] Reprinted with permission.

The position, symmetry and intensity of the peaks in the Raman spectrum give information about the structure and the electronic properties of the carbon based material. The Raman spectrum of graphene shows two distinct peaks at about 1584 cm^{-1} (G peak) and 2700 cm^{-1} (2D peak), respectively. When working with silica as substrate, a sharp peak at about 520 cm^{-1} is associated with crystalline silicon[232-234] and the broad peak between 900-1000 cm^{-1} stems from the amorphous silicon dioxide on the silica wafer.[235] The G peak corresponds to a primary in-plane vibration mode in the graphene lattice and is the only mode originating in a first-order Raman scattering process. The 2D peak corresponds to a second-order overtone of a different in-plane vibration.[236] The 2D shows for pristine graphene a higher signal intensity than the G peak. The position of the 2D peak is dependent on the wavelength of the excited laser.[237] A peak at 1340 cm^{-1} (D peak) starts to appear when defects are introduced to the graphene lattice. This peak also depends on the laser excitation energy and also results from a second-order Raman scattering process.[237] An increase in the intensity of the D peak in the Raman spectrum indicates an increased defect density.[131, 238] The 2D peak in the Raman spectra has its maximum intensity for single-layer graphene and shows a reduced intensity for multi-layer graphene and graphite (Figure 10). Mathematical fitting of the raw Raman spectra allows for extraction of parameters such as the full width at half maximum (FWHM) Γ of a peak, the peak position x, and the peak intensity I. The analysis of the FWHM of the G peak and 2D peak are important and gives information about the number of graphene layers in the sample.[238] The Γ_G values should be between 12 cm^{-1} and 51 cm^{-1} and the Γ_{2D} values should be less than 50 cm^{-1} for single-layer graphene. Also, the ratio between the intensities for the G and 2D peaks (I_G/I_{2D}) carries information.[239] The smaller the defect density of the graphene lattice, the smaller is the I_G/I_{2D} ratio.[240] The doping effect on the Raman spectrum of graphene has been previously studied.[217, 230] The application of a negative top-gate voltage leads to a n-doping effect, while the application of a positive voltage leads to a p-doping effect on graphene. Starting from the Dirac point both, n- and p-doping lead to a stiffening of the G peak by decreasing the FWHM Γ_G of the G peak. Doping of graphene also influences the 2D peak in the Raman spectrum. Doping leads to peak broadening (increasing of FWHM Γ_{2D}) of the 2D peak and change in its peak position x_{2D}.[230]

In a similar way to the characterization of graphene with Raman spectroscopy, both MoS_2 and functionalized MoS_2 can be studied and characterized.[241-246] Four first-order Raman peaks can be observed for bulk MoS_2 at 32 cm^{-1} (E_{2g}^2), 286 cm^{-1} (E_{1g}), 383 cm^{-1} (E_{2g}^1) and 408 cm^{-1}(A_{1g}). The E_{2g}^2 band arises from the vibration of S-Mo-S layer against an adjacent layer and the E_{1g} band is from the vibration of S-Mo-S layer on a basal plane. The E_{2g}^1 band comes from the opposite vibration of two sulfur atoms with respect to the Mo atom (in-plane vibrations). The A_{1g} band is associated with out-of-plane vibrations from sulfur atoms in opposite directions.[247] In mono-layer MoS_2 are the E_{2g}^1 and A_{1g} bands the most prominent peaks are at around 385 cm^{-1} and 404 cm^{-1} (Figure 11).[69] These two bands however shift when having two or three MoS_2 layer on top of each other and are therefore an important identification criteria for mono-layer MoS_2. For mono-layer MoS_2 a frequency difference between E_{2g}^1 and A_{1g} of 19.2 cm^{-1} is reported. The frequency difference between E_{2g}^1 and A_{1g} for two-layer MoS_2 is 22.3 cm^{-1} and 24.4 cm^{-1} for three-layer MoS_2.[69, 92, 248]

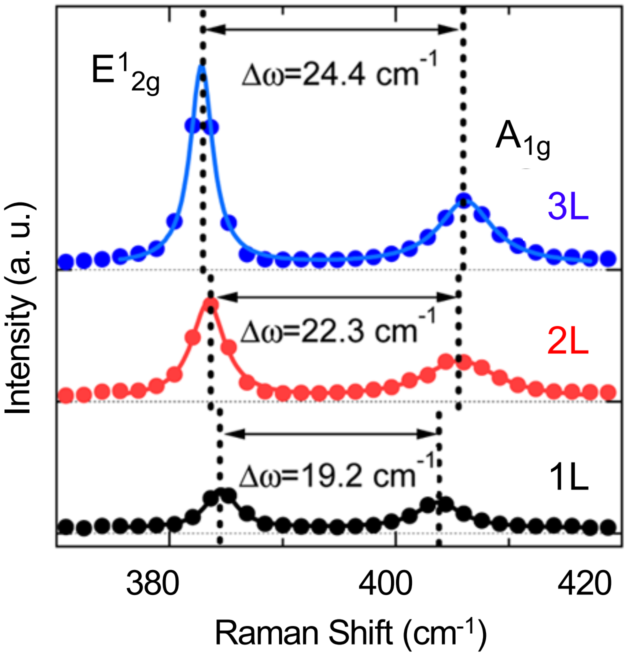

Figure 11: Raman spectra of one-layer, two-layer and three-layer MoS_2, showing a distinct difference in frequencies between the $E_{2g}{}^1$ and A_{1g} peaks for all 3 materials.[92] *Reprinted with permission.*

3.4 X-Ray Photoelectron Spectroscopy

X-ray photoelectron spectroscopy (XPS) is a powerful tool to analyze the surface of materials quantitatively and qualitatively.[249] The sample is irradiated with a beam of X-rays. Upon irradiation with X-ray, electrons are released. The kinetic energies of the electrons being released during the irradiation are measured. Typically, two types of spectra are recorded in XPS studies.[250] The survey scan reveals the overall composition of the sample. Various elements emit electrons of different energies and the XPS spectrum gives therefore information about the elemental composition of a sample. A narrower scan provides information about the chemical state of each element. The XPS spectrum of graphite mainly gives one non-symmetric peak for the electrons from the sp^2-hybridized carbon atoms C 1s at around 284.4 eV and a low intensity peak at 191.4 eV.[251-253] The XPS spectrum of graphene depends on its substrate and the C 1s peak in the case of silica the is at 284.6 eV.[254] The observed binding energy is consistent with the sp^2-hybridized character of the carbon present in graphene, together with minor contribution from certain oxidized states that cannot be completely avoided during the preparation.[254-255] Other observed signals correspond to silicon (Si) and oxygen (O), at 104 eV and 533 eV, respectively,[256] originating from the SiO_2-intersurface in between the graphene layer and silicon substrate. Comparison among the XPS spectra of pristine graphene, functionalized graphene and the neat molecules on silica confirms the non-covalent adsorption of the molecular systems on graphene. Nitrogen (N) is one of the most studied heteroatoms in doped carbon containing materials and a nitrogen atom containing compound non-covalently bound to graphene shows a N 1s signal, which arises from the molecule itself. A small nitrogen

N1s signal is observed for CVD graphene at 400 eV,[256] likely corresponding to adsorbed molecular nitrogen is also found in the spectra of pure CVD graphene samples. Due to its low intensity, the signal from the molecular nitrogen is supposed to have negligible effects on the XPS studies in the N1s region. A shift of the N 1s peak between a sample of the molecule on silica and a sample of the molecule on non-covalently bound to graphene can be interpreted as an effect of the interaction between the non-covalently bound molecule and graphene. This can give information about the doping of graphene by non-covalently bound molecules.[257] In the case of graphene functionalization with charged molecules, different counterions introduce other elements such as iodine (I), sulfur (S), boron (B) and fluorine (F) to the surface of graphene and can be detected. XPS studies were performed in this thesis to analyze the non-covalent functionalization of graphene and the doping effect of non-covalently bound molecules on graphene.

The doping of graphene with an electron deficient molecule has been studied previously with XPS in the literature.[258-259] While the N1s peak of tetracyanoethylene (TCNE) is at 400.4 eV, the N 1s peak of TCNE on graphene is shifted to 398.8 eV. The charge-transfer from graphene to TCNE is interpreted as a result of p-doping of graphene. In an analogue way has tetrathiafulvalene (TTF) been deposited onto graphene and showed two S 2p signals. One signal at 163.5 eV is for the neutral TTF[260] and one signal at 164.7 eV[261] corresponds to the positively charged TTF due to n-doping of graphene.

3.5 Mass Spectrometry

Time-of-flight secondary ion mass spectrometry (ToF-SIMS) is a fast but destructive analytical technique to analyze the surface of materials.[262] ToF-SIMS gives information about the elemental content and the molecular composition of a surface. Both atoms and molecules can be determined simultaneously. The surface of a sample is bombarded by a focused primary ion beam. This causes the emission of particles. A small amount of these particles (< 1%) is ionized to positively or negatively charged ions the so-called secondary ions. The mass/charge ratios of these secondary ions are detected by a mass spectrometer. In the case of already charged molecules, can the ionization lead to the acquirement or loss of at least one electron. The detection limit of ToF-SIMS is very low (ppb, fmol) and ToF-SIMS can detect both positively and negatively charged ions between 0-1000 Da. Mass spectrometry imaging (MSI) has emerged into a powerful tool for the simultaneously mapping of multiple species. It allows the distribution of molecules on a surface to be monitored. The focused primary ion beam scans the sample surface and acquires spectra at different locations on the sample surface.

Matrix-assisted laser desorption/ionization (MALDI) is an ionization technique in mass spectrometry that is used to determine and detect molecules with a large mass (mass range: 600 to 750,000 Da). During the sample preparation, the analyte is mixed with a suitable matrix molecule and applied to a metal plate. The matrix absorbs the energy from the used laser and helps to ionize the analyte. Therefore, the matrix should have its maximum adsorption at the same wavelength as the operated laser from the MALDI. In the next step the sample is irradiated with a pulsed laser, which causes the fragmentation and desorption of both the analyte and matrix molecules. This is followed by protonation or deprotonation of the analyte. The ions are then detected with a mass spectrometer. MALDI is widely used with ToF spectrometer due to the large detection range. MALDI-ToF mass spectrometry is often the only way to analyze insoluble PAH with a molecular weight of >2000 Da.[263] The matrix for the analysis of PAH such as HBC derivatives was TCNQ chosen because it is a strong electron acceptor and has its maximum adsorption at 337 nm The same wavelength of the operated laser from the MALDI. Other tested matrix molecules showed a lower signal-to-noise ratio. However, the even stronger electron accepting 2,3,5,6-tetrafluoro-7,7,8,8-tetracyanoquino dimethane ($TCNQF_4$) did not show an increase signal-to-noise ratio. The used matrix was mixed with the analyte in a ratio up to 1:500 and suspended in water. After sonification of the suspension, the sample was applied onto the MALDI sample holder and the solvent was evaporated before analyzation. The homogeneous mixing of analyte and matrix is essential for a successful analysis. The group of Klaus Müllen has reported the poor solubility of hexa(4-iodo)-*peri*-hexabenzocoronene **31**.[264] It is a solid, which cannot be dissolved in common solvents. For its purification, **31** is washed with methanol to remove unreacted $FeCl_3$, side products and starting material. So far, no other purification method has been reported. The molecule however was successfully detected using MALDI-ToF mass spectrometry.

3.6 Cyclic Voltammetry of Organic Molecules

Cyclic voltammetry is a dynamic electrochemical method to measure and study the redox properties of molecules.[265-267] In a cyclic voltammetry experiment, a potential is applied to an electrode. The linear rate of change in voltage over time is called scan rat (V/s). The standard set-up for a cyclic voltammetry experiment consists of a three-electrode cell including reference electrode, counter electrode and working electrode. While the potential of the three-electrode cell is measured between working electrode and reference electrode, the current of the three-electrode cell is measured between working electrode and counter electrode. The recorded data are plotted as current versus applied potential. If the reduction potential of an analyte is reached, the current increases. The decrease in current that follows on the initial increase reflects the decrease in concentration of the reducible analyte. If the reduction event of a species is reversible, the reduced species will be re-oxidized during the reverse scan. That can be observed by an increased current with reverse polarity to the reduction event. The more symmetric the reduction and re-oxidizing events are, the more reversible the analyzed process. The peak current is directly proportional to the square root of the scan rate. The diffusion of analyte molecules can cause an adsorption of the molecules on the surface of the working electrode. This physical process is described in the Randles-Sevcik equation (1)[268]

$$i_p = 0.4463 \cdot nFAC\left(\frac{nFvD}{RT}\right)^{\frac{1}{2}} \tag{1}$$

where ip is the current maximum, n is the number of electrons transferred in the redox event, F is the Faraday constant, A is the electrode area, C is the concentration, v is the scan rate, D is the diffusion coefficient, R is the Gas constant and T is the temperature. This equation can be used to extract the diffusion coefficient D from a cyclic voltammogram. Adsorption of the analyte on the surface of the working electrode decreases the peak current. The reversible electrode reaction (E) is described by an equilibrium between the reducing agent, R, and the oxidizing agent, O.[269] The oxidizing agent can undergo in a second step a nonreversible chemical reaction (C), which is described by the rate constant k_{EC}. A combination of both steps is called electrolysis reaction (EC reaction, Figure 12).

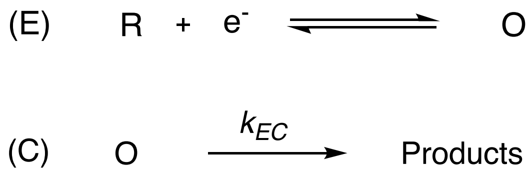

Figure 12: Overview of the EC mechanism. The reversible formation of O in the electrode reaction (E) is subsequentially followed by an irreversible chemical reaction (C).

3.7 Photophysical Characterization of Organic Molecules and MoS$_2$

The interaction between light and matter is a fundamental physical process. Light can be described as an electromagnetic radiation as well as a particle, the so-called photon. This concept is called wave-particle duality. The energy of photons is described by the Planck's equation (2):

$$E = h \cdot \nu = \frac{hc}{\lambda} \tag{2}$$

h is the Planck's constant, ν is the frequency of the electromagnetic wave, c is the speed of light in vacuum and λ is the wavelength.[270] Photoluminescence (PL) is a physical process in which a molecule absorbs and re-emits a photon. The interaction between the electrical component of light and electrons in a molecule change the charge distribution of the molecule and result in an excited state. The energy of the light needs to match the energy difference between ground state and excited state of the molecule. This phenomena is described by Bohr´s frequency condition (3).[270]

$$\Delta E = E_{final} - E_{initial} = h \cdot \nu \tag{3}$$

The excited electron in the so-called Franck Codon state relaxes subsequent to the lowest vibrational level of the singlet excited state (released as heat), which has the same spin multiplicity as the ground state and are called S$_1$, S$_2$, …, S$_N$. The relation between matter and light is displayed in the Jablonski diagram in Figure 13.

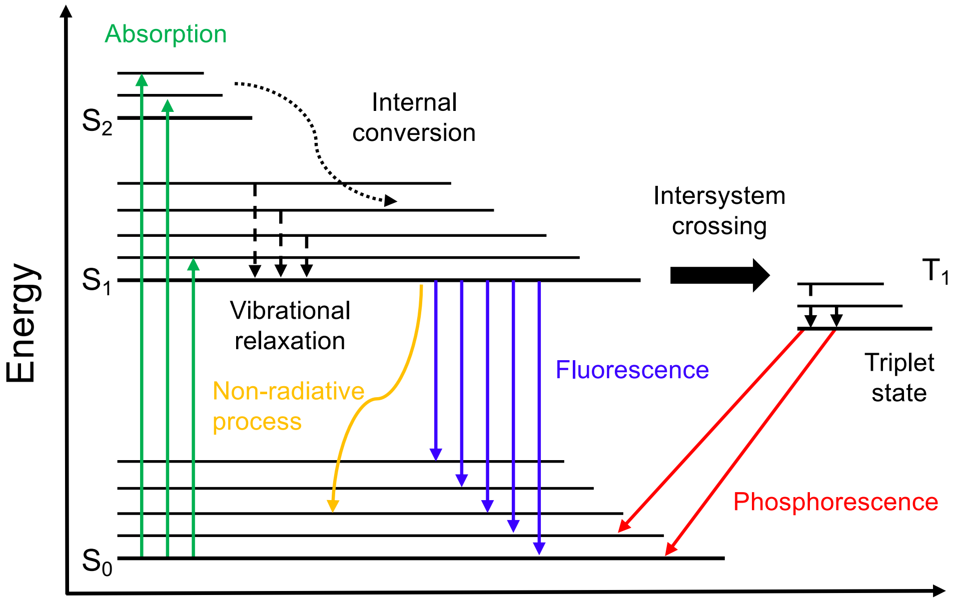

Figure 13: One form of the Jablonski diagram. The thick horizontal lines represent the energy levels of singlet (S_n) or triplet states (T_n) and the thin horizontal lines represent the vibrational energy levels. The diagram shows the principal luminescence processes of excited organic molecules.

Electrons in a higher electronic excited state can relax back to the ground state by either a radiative- or non-radiative processes. The radiative process is a singlet to singlet electronic relaxation, were the molecule emits a photon from the excited state and goes back to the ground state, S_0. This process is called fluorescence and the typical lifetime of standard fluorescent dyes, such as fluorescein, is on the nanosecond scale. The non-radiative processes are either intersystem crossing or internal conversion. The intersystem crossing, were the spin multiplicity is changed from a singlet to a triplet state (or other spin multiplicity) leads to a photon emission called phosphorescence. Phosphorescence is more unlikely to occur due to the change of spin and therefore has a typical lifetime of milliseconds to hours, longer than that of fluorescence.[271] The internal conversion brings the molecule to a lower spin state without energy loss followed by vibrational relaxation to the lowest vibrational level.[272] Photons that match the energy gap of the analyte are adsorbed and bring the molecule to an excited state. The sample has the complementary color of the absorbed light. The intensity difference between received and transmitted light is measured. The absorption of a sample is, according to the Lambert-Beer rule, directly proportional to the concentration of the sample c, the thickness of the cuvette l and the molar absorptivity ε (4)[270]

$$A = \log\frac{I_0}{I} = \varepsilon \cdot c \cdot l \tag{4}$$

The Stokes shift of a molecule describes the difference in energy between the position of its band maxima of the absorption and emission spectra of the same electronic transition. The excited molecule loses energy due to molecular vibrations. Therefore the emitted light has a larger wavelength compared to the excitation wavelength. UV-Vis spectroscopy is used to characterize the absorption of different organic salts in liquid and solid state. It is a nondestructive and nonintrusive method to study the optical and electronic properties of molecules and materials.

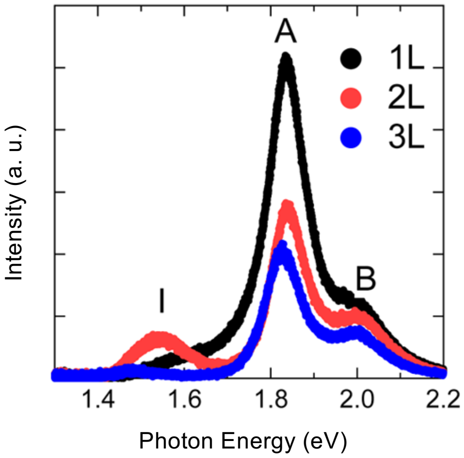

Figure 14: PL spectra of monolayer (1L), two-layer (2L) and three-layer (3L) MoS_2. The two main peaks A and B arise from the direct band gap transition, while the peak I is due to the indirect band gap transition.[92] Reprinted with permission.

In the case of the semiconducting MoS_2, a strong photoluminescence has been detected for monolayer MoS_2.[273] The enhancement of the photoluminescence is a factor of 10^4 stronger for monolayer MoS_2, compared to bulk MoS_2. This can be explained by transition from the indirect-gap bulk MoS_2 to the direct-gap nature of monolayer MoS_2.[274] The synthetic method of MoS_2 impacts the intensity of the photoluminescence, and variation has been reported.[89] The PL spectrum of monolayer MoS_2 has two main peaks at approximately 1.85 eV (A) and 2.05 eV (B; Figure 14). Both peaks arise from a direct band gap transition and their energy differences at the band maxima corresponds to a valence-band splitting. The peak intensity is inversely proportional to the number of MoS_2 layers on top of each other. Another weaker PL peak (I) is observed at lower energies for two-layer (2L) and three-layer (3L) MoS_2. This peak comes from an indirect band gap transition.[273-274] The A peak is associated to a exciton peak (approximately 1.88 eV) and a negative trion peak (approximately 1.84 eV) in a Lorentzian fitting. The chemical doping of MoS_2 changes the spectral weight of these two peaks and leads therefor to a shifting of the A peak.[92] While treatment of MoS_2 with p-type dopants like $TCNQF_4$ and TCNQ showed a drastic increase of the photoluminescence in monolayer MoS_2 as well as a blue shift of the peak energy from the PL spectrum. In contrast, n-type dopants like nicotinamide adenine dinucleotide (NADH) caused a suppression of the PL intensity monolayer MoS_2 and a red shift of the peak energy from the PL spectrum. The intensity enhancement of the photoluminescence was explained with an extraction of electrons and the decrease of the photoluminescence was explained with an injection of electrons.[92] Another example for the enhancement of the PL of monolayer MoS_2 can be done by surface functionalization with gallium nanoparticles. This showed a 9.2 times increased photoluminescence for monolayer MoS_2.[275]

3.8 Atomic Force Microscopy

Atomic Force Microscopy (AFM) is a versatile imaging technique, which is used to analyze surfaces and gain information about the topology of a surface.[276] It is the most powerful tool to study the thickness of graphene flakes and films since its height detection resolution is up to 0.1 nm (Figure 15). The AFM consists of a cantilever on which a sharp tip is mounted. This tip scans the sample surface in X/Y direction, while a laser beam is shining on the cantilever. The deflection of the laser gives information about the interaction between the tip and the sample surface. The AFM can operate in several imaging modes according to the nature of the tip motion: contact mode, non-contact mode, and tapping mode (intermitted mode). The terms contact mode and non-contact mode already explain that the cantilever tip has physical contact or no physical contact to the sample surface. The cantilever is vibrated or oscillated in tapping mode and has periodic contact to the sample surface. Van der Waals forces, dipole-dipole interactions and electrostatic forces with the sample surface change the oscillation frequency. A feedback loop is needed to maintain a constant oscillation frequency. The tapping mode is preferred for functionalized 2D materials since it can better cope with impurities such as adsorbed dirt on the cantilever tip or scratched samples.

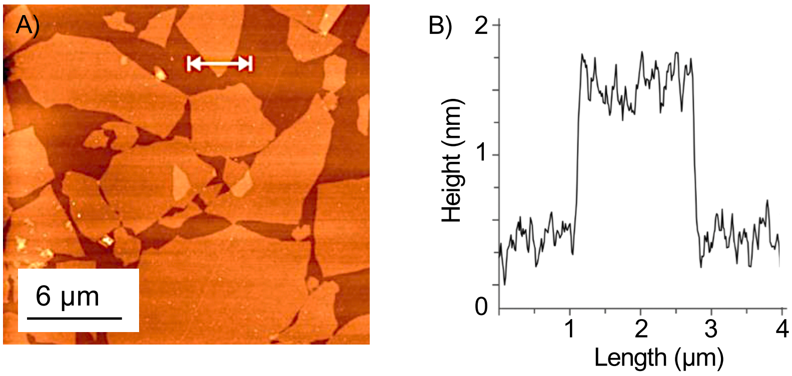

Figure 15: A) AFM image of a silica wafer (Si/300nm SiO_2) coated with oxo-G and B) height profile of an oxo-G flake along the white arrow is shown, showing a flake thickness of approximately 1.4 nm.

4. Hypothesis and Aims

This thesis is based on three major ideas. First, graphene and MoS_2 can be non-covalently functionalized by cationic π-conjugated systems. Second, different anionic counter ions result in a different binding affinity between the cationic π-conjugated systems and graphene or MoS_2. And third, the number of positive charges and/or the size of the π-conjugated system will affect both the binding strength and doping ability. From these ideas the following aims can be derived:

- Synthesis and characterization of a series of cationic π-conjugated systems (monocationic, trication and hexacationic) with different counterions.

- Develop of a method to non-covalently functionalize graphene and MoS_2 non-covalently with cationic π-conjugated systems and their uncharged precursors.

- Find analytical tools to characterize and study the non-covalent interactions between cationic π-conjugated systems and graphene (and MoS_2).

- Study the binding affinities between the π-conjugated systems and graphene.

5. Results and Discussion

5.1 Synthesis and Characterization of Organic Molecules

To study the doping effect of non-covalently bound cationic molecules on graphene, a series of π-conjugated molecules was synthesized. These systems are adhered to graphene *via* van der Waals forces, here in particular *via* dispersion forces. Orbital hybridization between the π-conjugated molecules and graphene makes also a substantial contribution. The comparison between molecules with a small, medium or large π-conjugated structures will help to reveal the structure-property relationships of the non-covalent interactions between charged π-conjugated molecules and graphene. This thesis focusses on different synthetic routes and strategies for the synthesis of imidazole, imidazolium and pyridinium derivatives as well as hexaphenylbenzene (HPB) and hexa-*peri*-hexabenzocoronene (HBC) derivatives.

5.1.1 Synthetic Strategies

Imidazole and its benzo derivative benzimidazole can be obtained *via* various of different synthetic approaches.[277] The condensation reaction between a carboxylic acid and a diamine (see mechanism in 2.2.2) is favoured, because it is an easy and fast method to build up a series of different imidazole derivatives from commercial available starting materials. Imidazole and its derivatives can undergo an *N*-alkylation reaction to introduce an alkyl chain to the molecular structure. This intermediate can undergo a second *N*-alkylation reaction to obtain a cationic benzimidazolium molecule. Imidazole and its derivatives can also undergo a twofold *N*-alkylation in one-pot synthesis. Sometimes it is however more practical to perform a double *N*-alkylation in two separate reaction steps. The *N*-alkylation reaction of a pyridine moiety leads to a cationic pyridinium compound.

There are two main synthetic strategies to prepare HPB derivatives (Scheme 7). The first strategy is used to obtain star-shaped HPB derivatives. Here, three diphenylacetylene derivatives **32** (functionalized in *para*-position) are cyclotrimerized in a transition metal catalysed reaction to HPB derivatives **33**.[278] The substitution pattern of HPB derivatives can be designed individually by the choice of the respective alkynes. The second route is based on the Diels-Alder reaction between diphenylacetylene derivative **32** and a cyclopentadienone derivative **34** and is used for the synthesis of HPB derivatives with different symmetries.[279-280] The use of diyne derivatives **35** in cyclotrimerization reactions yield another class of hexaarylbenzene derivatives **36**. It has been also shown that dialkynes like 1,4-bis(4'-(*tert*-butyl)phenyl)-buta-1,3-diyene **37** can also react with cyclopentadienone derivative **38** to form arylethynylene(pentaaryl)benzene derivative **39** (Scheme 7).[281] Molecules, created either *via* the Diels-Alder reaction or the cyclotrimerization reaction can be oxidized yielding molecules with a more planar molecular geometry. A discussion about geometric properties will be introduced in the following chapter.

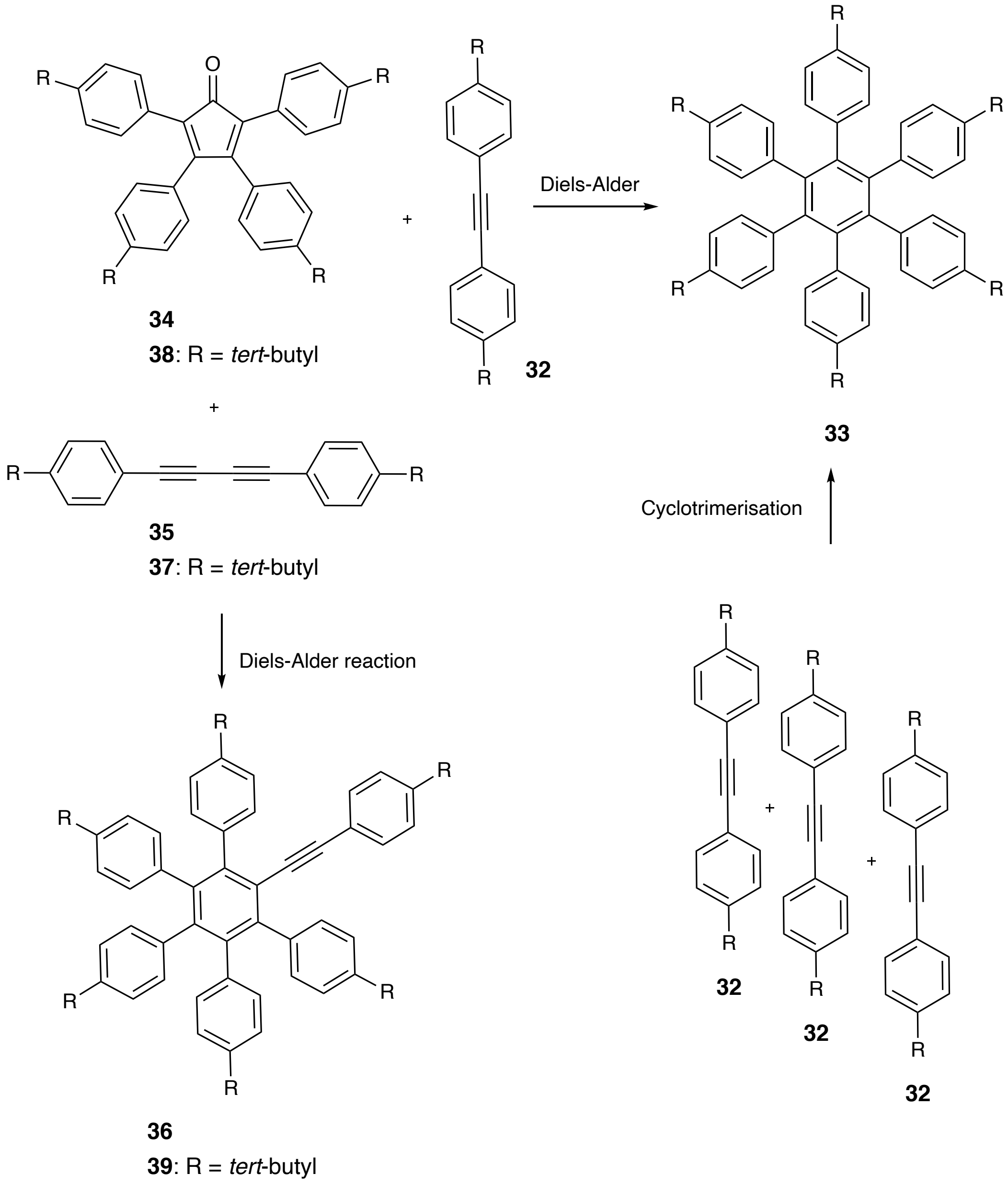

Scheme 7. Schematic synthesis of HPB via Diels-Alder reaction or cyclotrimerization reaction.

In principle there are two main strategies to synthesize HBC derivatives **40**. In the first one, HPBs with tailored periphery **41** are oxidatized under Scholl conditions (Scheme 8). In the second strategy, the six-fold iodinated hexa(4-iodo)-*peri*-hexabenzocoronene **31**[264] is used as starting material for further palladium catalyzed cross coupling reactions. One example is the Sonogashira-cross coupling between compound **31** and six 1-tetradecyne molecules to obtain a soluble HBC derivative in high yields (82%).[210] **31** however is synthesized from molecule **30** *via* Scholl oxidation (Scheme 8). Therefore, the Scholl oxidation is a key step for both strategies. The Scholl reaction was reported for the first time in 1910.[282] It is a dehydrogenation reaction induced by Lewis acids, such as $AlCl_3$, that results in a condensed ring system.[283-284] Protocols for the Scholl oxidation with various Lewis acids and solvent combinations have been reported, for example $CuCl_2/AlCl_3$, $Cu(OTf)_2/AlCl_3$ in CS_2,[193] or with $FeCl_3$ dissolved in nitromethane.[207] The common Lewis acid $FeCl_3$ was one of the first reagents used for this cyclization reaction.[285] However, the best oxidation conditions have not yet been standardized.

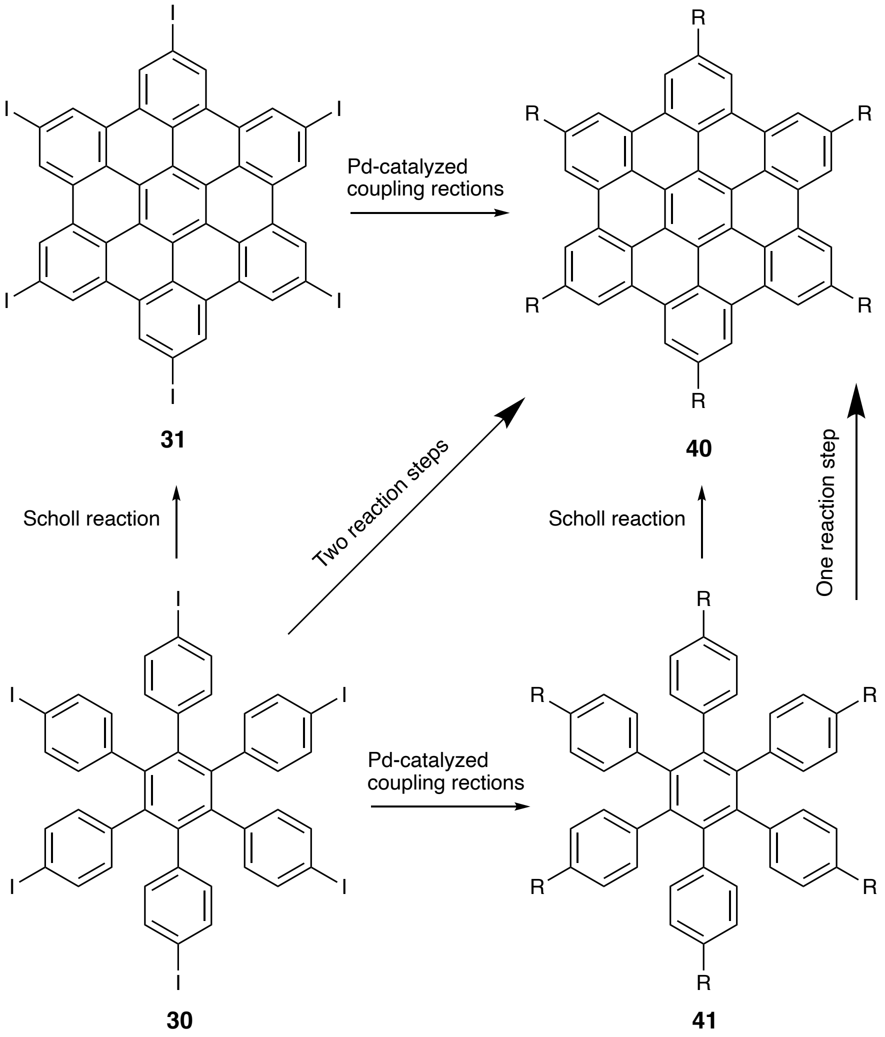

*Scheme 8. Synthesis of hexa-peri-hexabenzocoronene derivatives **40** via two different synthetic routes.*

5.1.2 Synthesis and Synthetic Outcomes

The C_6 symmetric hexa(*p*-iodophenyl)benzene **30** was chosen as a key intermediate, for the subsequent palladium catalysed cross-coupling reactions, to build up a series of the hexaphenyl benzene derivatives (**41**). These derivatives were later used to non-covalently functionalize graphene and monolayer MoS_2. For the synthesis of hexaphenylbenzene, **42**, diphenylacetylene, **43** reacts in a transition metal catalysed cyclotrimersation reaction (Scheme 9).[278] The use of catalyst bis(acetonitrile)dichloropalladium(II) gave **42** in 82% yield after a reaction for 24 h under inert atmosphere at room temperature. **42** was subsequently iodinated in a second step with bis(trisfluoroacetoxy)iodobenzene, **44** and elemental iodine in the absence of light to obtain the key intermediate **30** in 70% yield.[286] The presence of light did not result in product formation. Hexa(*p*-iodophenyl)benzene, **30** is used for the reaction with 4-ethynylpyridine **45** to form **46** (**HexaPyCC**) as shown in Scheme 10.[287]

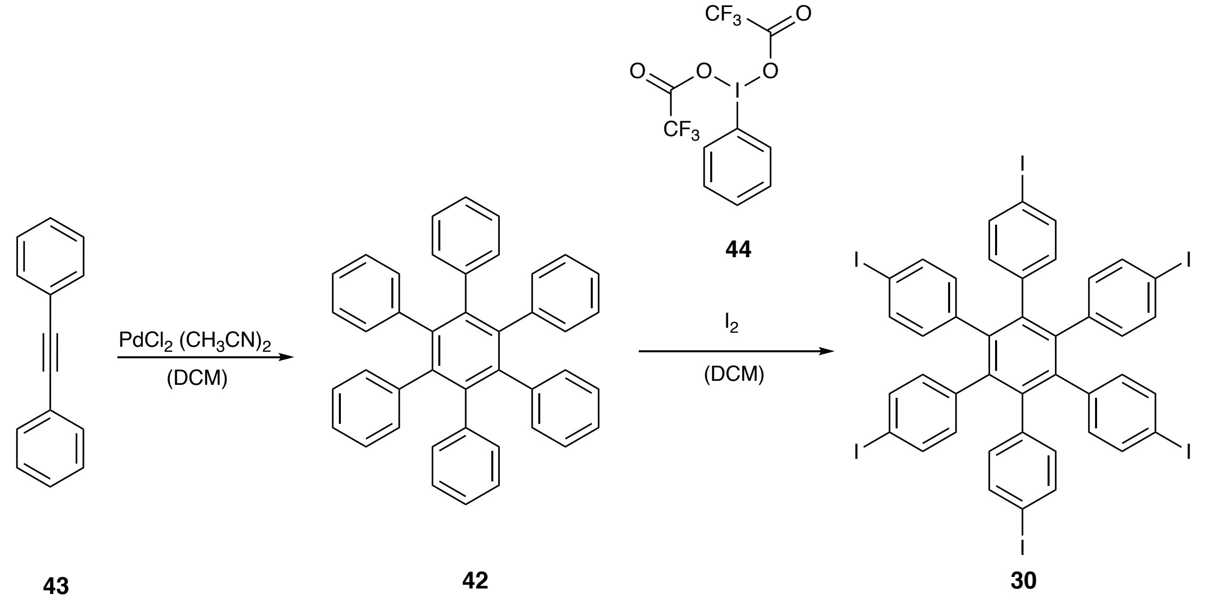

*Scheme 9. Synthesis of key compound **30** via iodination reaction of hexaphenylbenzene **42**.*

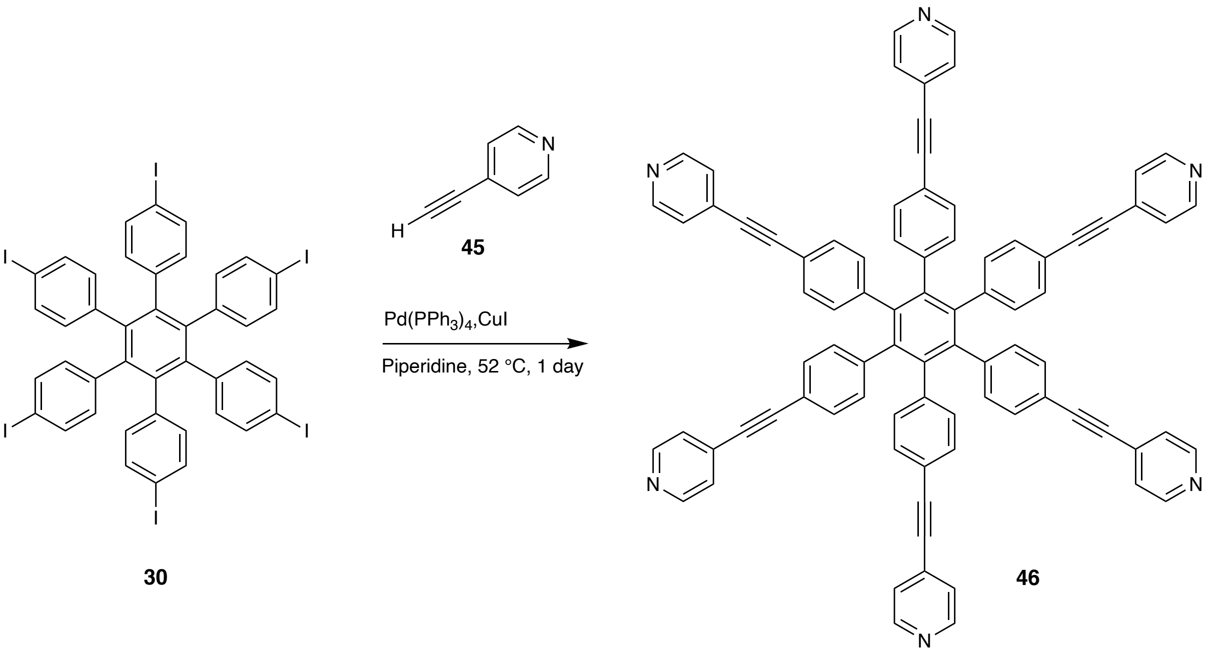

*Scheme 10. Synthesis of **46** via six-fold Sonogashira-Hagihara cross-coupling reaction between h*exa(p-*iodophenyl)benzene **30** and 4-ethynylpyridine **45**.*

In this thesis, I show a different synthetic method which results in improved yield when compared to published protocols. **30** was allowed to react in the presence of 12 equivalents of **31**, using tetrakis(triphenylphosphine)palladium(0) and copper iodide as catalysts in piperidine as solvent. The reaction mixture was heated to 52 °C and stirred for 24 hours. The four times and five times coupled products could be identified in the reaction mixture *via* NMR studies and MS analysis. Therefore, the Sonogashira-Hagihara reaction is not quantitative. The reaction mixture was purified *via* column chromatography giving the 5- and 6-times (**46**) substituted products in 29% and 30% yield, respectively. Altering the reaction time or the stoichiometric amount of **45** did not result in a higher yield. Molecule **30** was also reacted under the same conditions with 3-ethynylpyridine to receive another star-shaped pyridine functionalized **41**, however in lower yields. Further, the pyridine moiety of **46** can be alkylated using different alkylation agents to form pyridinium functionalities with different counterions and alkyl chains. Another pyridine functionalised HPB derivative, **47** (**HexaPy**), has been synthesized using a palladium catalysed Suzuki cross-coupling reaction (Scheme 11).[288]

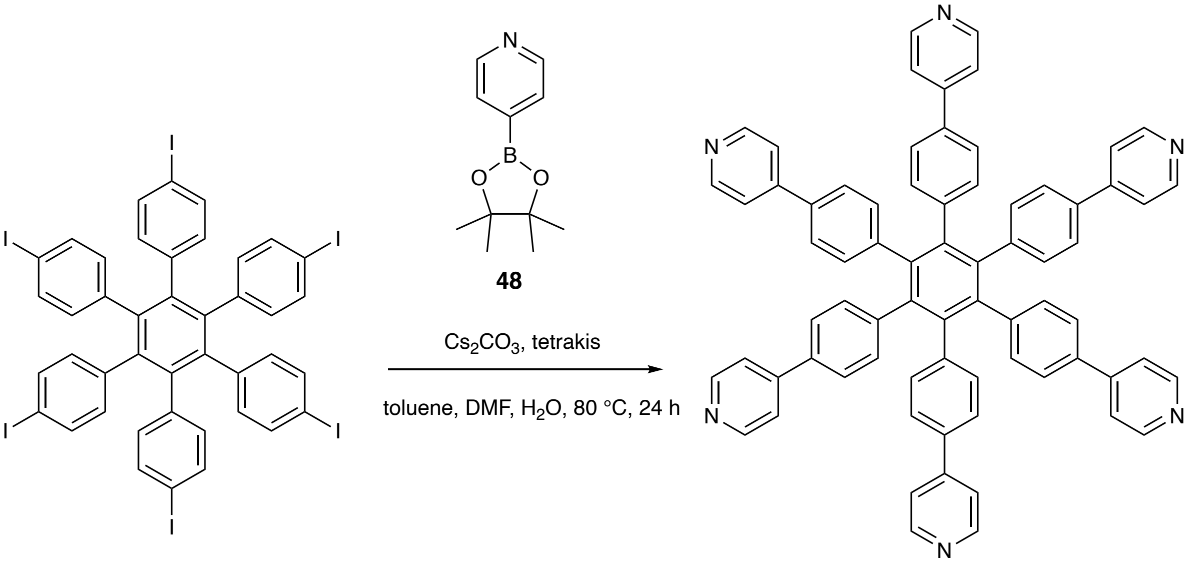

30 **47**

Scheme 11. Synthesis of HPB ***47*** *by six-fold Suzuki cross-coupling reaction between hexa(p-iodophenyl)benzene* ***22*** *and 4-pyridine boronic acid pinacol ester* ***48****.*

During this work the protocol was modified to increase the yield of **47** from 50% to 70%. Thus **30** is allowed to react together with 4-pyridine boronic acid pinacol ester **48** in the presence of a catalytic amount of tetrakis(triphenylphosphine)palladium(0) and caesium carbonate in a mixture of toluene and dimethylformamide at 80°C for 24 hours.

Another key HPB compound in this thesis is hexa(*p*-carboxyphenyl)benzene **49**, which can undergo condensation reactions together with diamines. The product of this reaction is a HPB derivative modified with six benzimidazole moieties in *para* position. In contrast to trimesic acid, **49** is not commercially available and had to be synthesized (Scheme 12). The synthesis of **49** commences with the preparation of 1,4-bis(*p*-carbomethoxybenzene)-1,2-acetylene **50**. This acetylene was obtained from methyl-4-iodobenzoate **51** in a palladium catalyzed Sonogashira-Hagihara cross-coupling reaction with trimethylsilylacetylene **52** in 90% yield in a single step.[289-290] This was possible, because the trimethylsilyl (TMS) protecting group was removed under the performed reaction. Trimethylsilylacetylene **52** is used instead of acetylene, because it has the benefit of being a liquid. It is also more electron rich and therefore a better coupling partner in this reaction. Acetylene **50** was subsequently cyclotrimerized in a second reaction step using $Co_2(CO)_8$ as the catalyst to form hexa(*p*-carbomethoxyphenyl)-benzene **53** in 95% yield.[291] It was crucial to use only a small amount of solvent, even if the starting material did not dissolve completely. Otherwise a conversion of the starting materials could not be observed. A possible explanation is that the reaction requires high concentrations of the acetylene derivatives to push the equilibrium towards the catalytically active bis(acetylene)cobalt complex (see section 2.2.1). The hexaester, **53** is deprotected with potassium hydroxide in a mixture of tetrahydrofuran and methanol to obtain hexa(*p*-carboxyphenyl)benzene **49** in 95% yield.

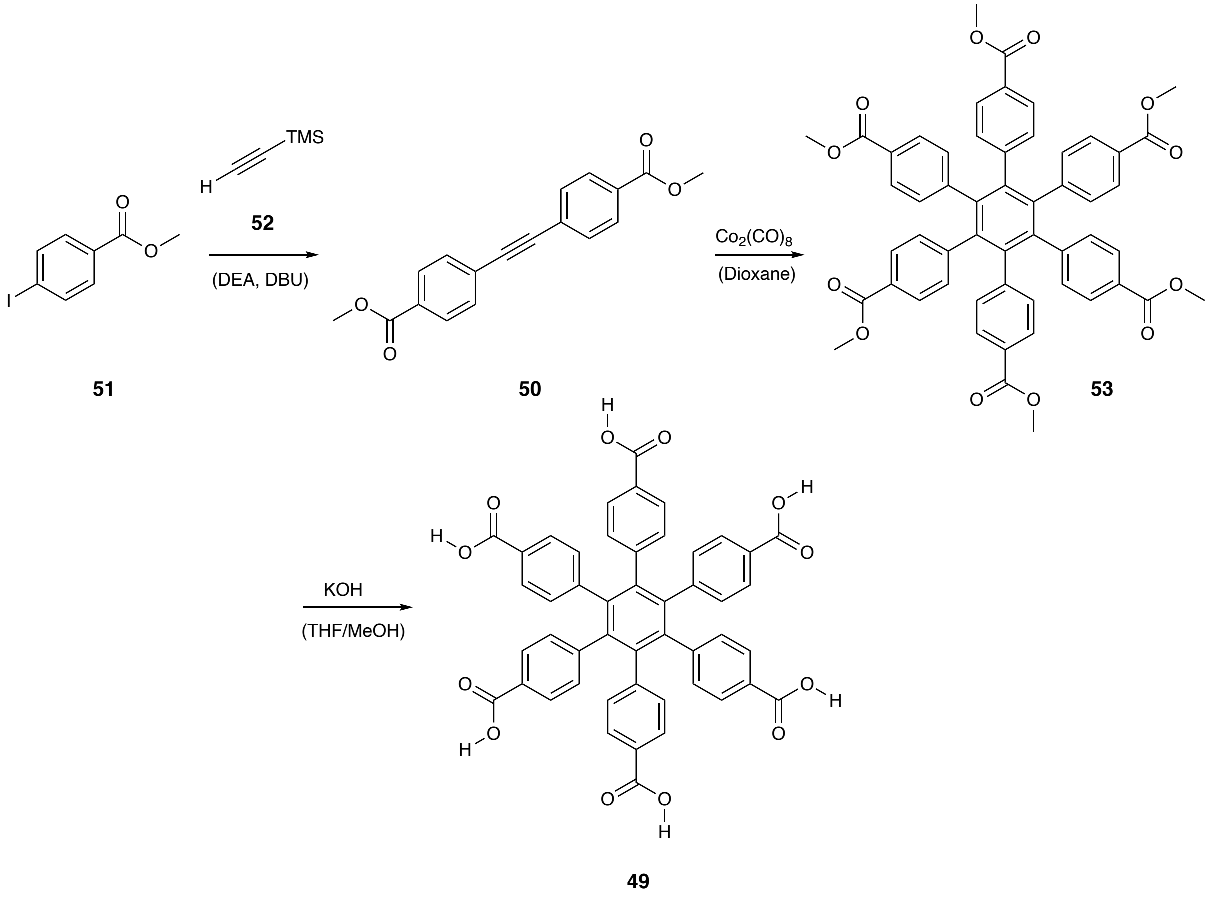

*Scheme 12. Synthesis of hexa(p-carboxyphenyl)benzene **49**, one of the significant compounds in this thesis.*

2-Methylbenzimidazole **54** (**MeBim**) and 2-phenylbenzimidazole **55** (**PhBim**) were chosen as small π-conjugated systems with a single benzimidazole moiety (Figure 16). Both molecules can interact with graphene *via* intermolecular interaction such as dispersive and electrostatic interactions. Previous studies of 2-phenylbenzimidazole **55** revealed its planar nature from the crystal structure and computational studies.[292] Both, benzimidazole derivatives **54** and **55** are commercially available or could be synthesized *via* condensation reaction between benzoic acid and *o*-phenylenediamine. The benzimidazole moieties of **54** and **55** can undergo further functionalization.

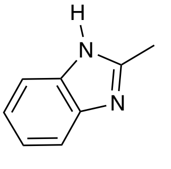

54

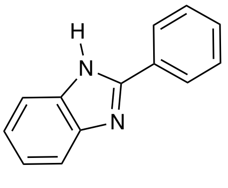

55

*Figure 16. Lewis structures of neutral molecules 2-methylbenzimidazole **54** and 2-phenylbenzimidazole **55**.*

1,3,5-tris(benzimidazolyl)benzene **56** (**TriBim**) is another key structure in this thesis. The medium sized π-conjugated molecule consists of a central benzene ring, which is meta-trisubstituted with three benzimidazole moieties. It is expected that both the benzene core as well as the benzimidazole moieties can interact *via* intermolecular interactions with graphene. In contrast to **54** and **55** is **56** not commercially available but readily accessible *via* condensation reaction of trimesic acid **67** with *o*-phenylenediamine **68** in poly phosphoric acid (Scheme 13). The reaction is reported in the literature and can be performed either by heating the reaction mixture with an ordinary heating plate or by using a microwave reactor.[156, 158, 293] The synthesis using microwave heating is faster and results in a higher product yield. In this thesis, a previously reported microwave based protocol[159] was applied to obtain the molecule **56** in 40% yield.[294]

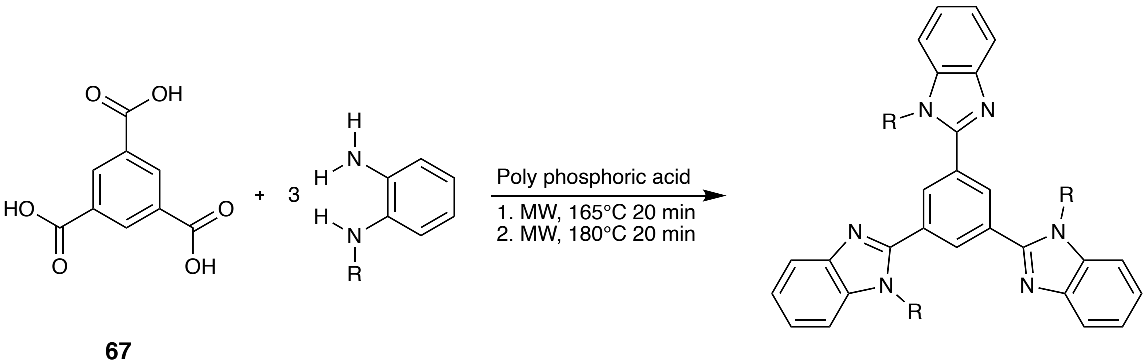

67

68: R = H
69: R = -methyl

56: R = H
70: R = -methyl

*Scheme 13. Synthesis of 1,3,5-tris(benzimidazolyl)benzene **56** and 1,3,5-tris(N-methyl-benzimidazolyl)benzene **70**.*

This protocol could also be applied using *N*-methyl-1,2-phenylenediamine **69** to form 1,3,5-tris(*N*-methyl-benzimidazolyl)benzene **70**. However, a lower yield of product was obtained (10%) in this case. The condensation reaction between hexa(*p*-carboxyphenyl)benzene **49** and *o*-phenylenediamine **68** was attempted employing microwave heating and similar conditions as for the synthesis of **56** but did not result in any product formation. Therefore, the reaction conditions had to be modified. Instead of mixing hexa(*p*-carboxyphenyl) benzene **49** and *o*-phenylenediamine **68** initially in poly phosphoric acid, only hexa(*p*-carboxyphenyl) benzene **49** was dissolved in poly phosphoric acid and heated for six hours at 100 °C. This step was necessary to form the initial carboxylic acid phosphate hexaester (see section 2.2.2). The ester intermediate is then allowed to react with 6.6 equivalents of diamine **68** at 180 °C (Scheme 14).

The work-up protocol was the same as for the synthesis of *C_3* symmetric **56** and gave *C_6* symmetric hexa(2-benzimidazolyl-1,4-phenylene)benzene **71** (**HexaBim**) and the target compound was obtained in 33% yield. The analogous condensation reaction between hexa(*p*-carboxyphenyl)benzene **49** and *N*-methyl-1,2-phenylenediamine **69** was in spite of several attempts not successful. Hexa(4-phenyl-2-benzimidazolyl)benzene **71** was also not accessible *via* coupling reaction between hexa(*p*-iodophenyl)benzene **30** and benzimidazole.

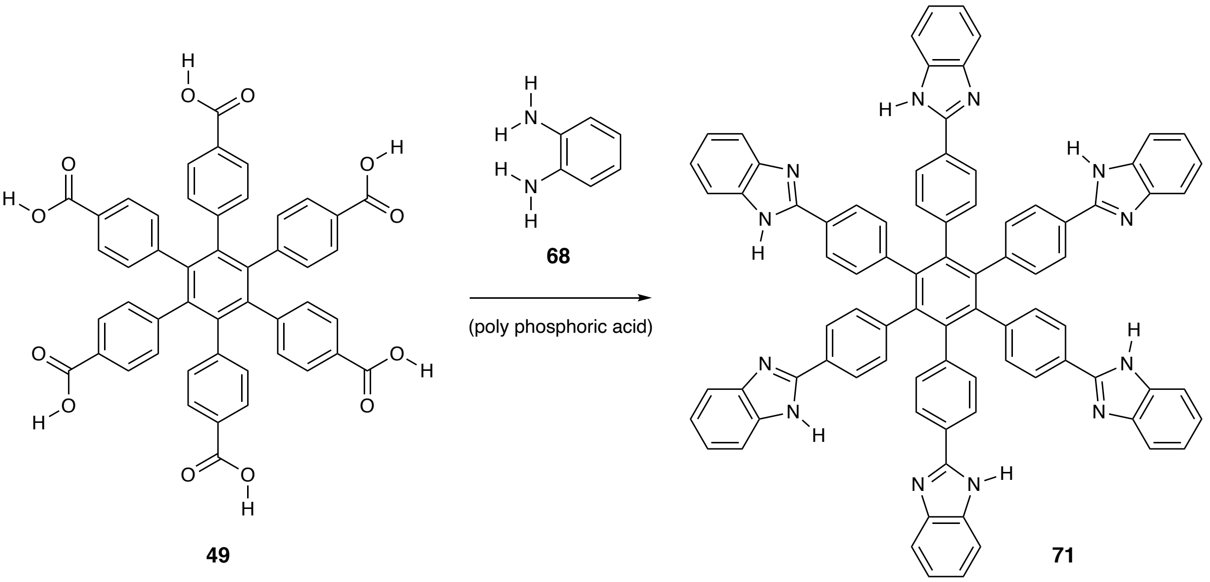

*Scheme 14. Synthesis of hexa(4-phenyl-2-benzimidazolyl)benzene **71** via condensation reaction between **49** and o-phenylenediamine **68** in polyphosphoric acid.*

5.1.3 Oxidation Reaction under Scholl Conditions

The Scholl oxidation with selected molecules, described in Chapter 5.1.1, was performed with either DDQ (together with triflic acid in dichloromethane) or $FeCl_3$ (together with nitromethane in dichloromethane) as oxidising agents. As already mentioned, HPB derivatives **41** with electron withdrawing groups in *para* position are less likely to the oxidation reaction. Therefore, the *C_6* symmetric hexa(*p*-carbomethoxyphenyl)benzene **53** and the hexa(*p*-carboxyphenyl)benzene **49** do not undergo a Scholl oxidation under the conditions specified above. Hexa(*p*-iodophenyl)benzene **30** and hexa(4-*tert*-butylphenyl)benzene **72** could be oxidized with $FeCl_3$ (together with nitromethane in dichloromethane) as oxidising agent. Arylethynylene(pentaaryl)benzene derivative **39** was transformed into the chiral pentaphene derivative **73** with $FeCl_3$ as Lewis acid catalyst as part of a collaboration with Philipp Rietsch.[281] This unprecedent ring-closing reaction proceeded in a similar fashion to the synthesis of HBCs. In comparison with hexa-*tert*-butyl-hexa-*peri*-hexabenzocoronene **29** and its 42 sp^2-carbon atoms show **73** a twisted geometry, similar to helicenes. The geometry differences are also responsible for a different packing in the crystal structures. The crystal structures of **73** and **29** are shown in Figure 17. It was however not possible for the *C_6* symmetric molecules **46** or **47** or **71** to undergo a Scholl oxidation reaction with either DDQ (together with triflic acid in dichloromethane) or FeCl$_3$ (together with nitromethane in dichloromethane) as oxidising agents.

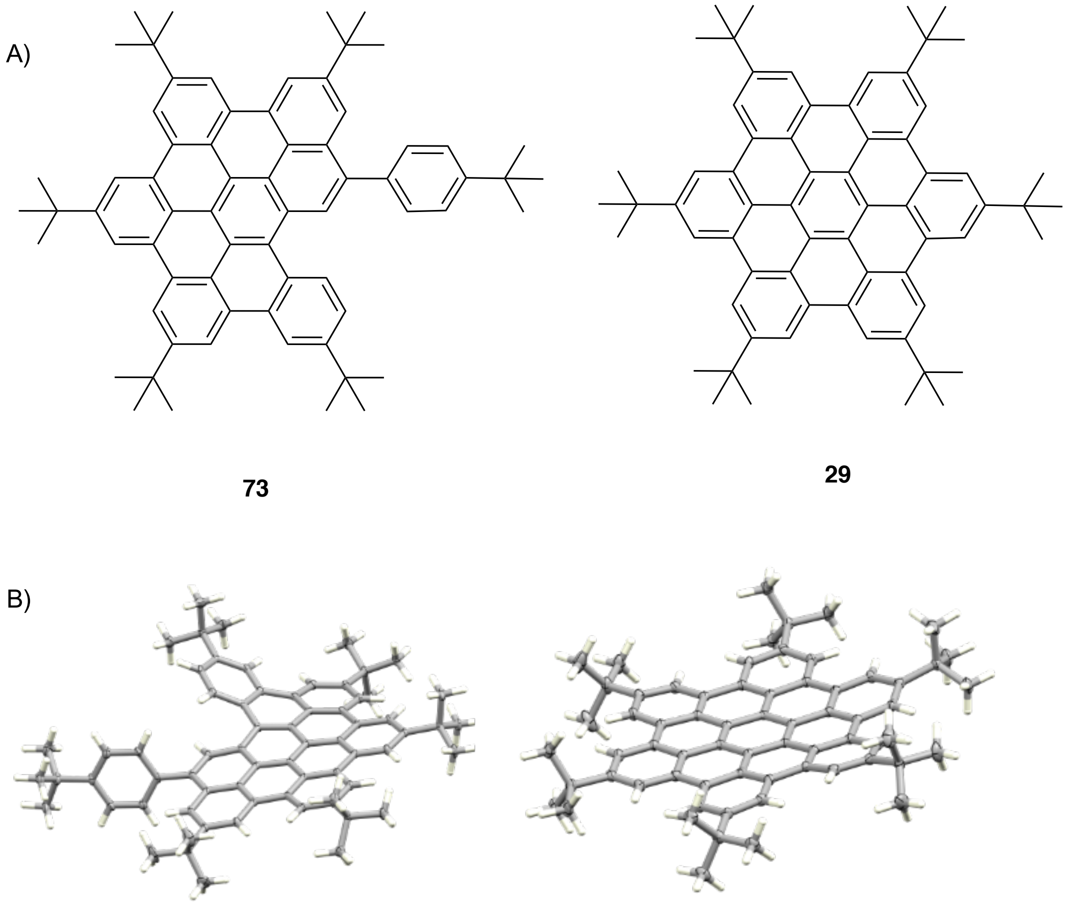

Figure 17. A) Lewis structures of unsymmetric hexaarylbenzene derivatives ***73*** *and* ***29*** *and B) single-crystal structures*[281] *of* ***73*** *and* ***29****. Reprinted with permission.*

5.1.4 Synthesis of Charged π-conjugated Systems

The previously described pyridine- and benzimidazole derivatives can undergo further functionalization such as the *N*-alkylation. In a first synthetic step, 2-phenyl-benzimidazole **55** was deprotonate with NaH and subsequently reacted with methyl iodide. In a second reaction step intermediate **74** reacts with an excess of methyl triflate forming the organic salt **(PhBim)**$^{+1}$**(OTf)**$^{-1}$ (**75**) (with the monocationic 1,3-dimethyl,2-phenyl-benzimidazolium ion **75**$^{1+}$ ((**PhBim)**$^{+1}$) as a white crystalline solid (Scheme 15). Monocationic 1,2,3-trimethyl benzimidazole **(TriMeBim)**$^{1+}$ (**76**$^{1+}$) was synthesized according to a similar protocol.[295]

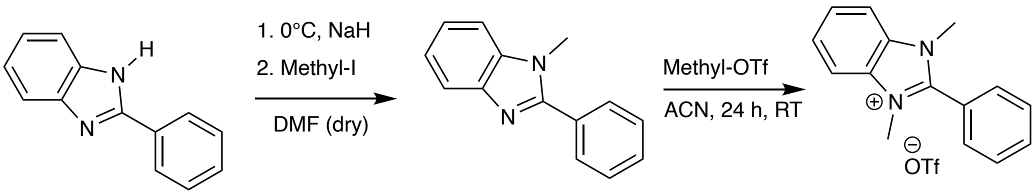

55 **74** **75**

Scheme 15. Synthesis of organic salt ***75*** *from its neutral derivatives* ***55*** *and* ***74****.*

1,3,5-tris(benzimidazolyl)benzene **56** is subjected to several *N*-alkylation reaction conditons with different alkylating agents to synthesize a series of tricationic compounds with various alkyl chain lengths and different counter ions (**77-83**, Scheme 16). These differences resulte in various solubilities of the obtained salts. While triflate salts show the best solubility in acetonitrile, halide salts dissolve best in more polar solvents like dimethyl sulfoxide. The synthesis of these organic molecules (**77-83**) is possible to complete in either a two-step or a one-pot synthesis. The first strategy is similar to the synthesis of **75**. The reaction sequence starts with a deprotonation step of **56** with subsequent quenching with methyl iodide to obtain methyl benzimidazole derivative **84**. In a second reaction, molecule **84** undergoes another *N*-alkylation reaction with an excess of alkylation agent. By using an excess of methyl iodide as alkylation agent and dry potassium carbonate as base at elevated temperature, a one-pot synthesis from 1,3,5-tris(benzimidazolyl)benzene **56** to 1,3,5-tris (*N*-methylbenzimidazolyl)benzene **77**$^{3+}$ is possible. The iodide counterion can be exchanged *via* ion exchange with silver salts. The latter protocol did not work with other alkylation agents, such as trimethyloxonium tetrafluoroborate or ethyl iodide.

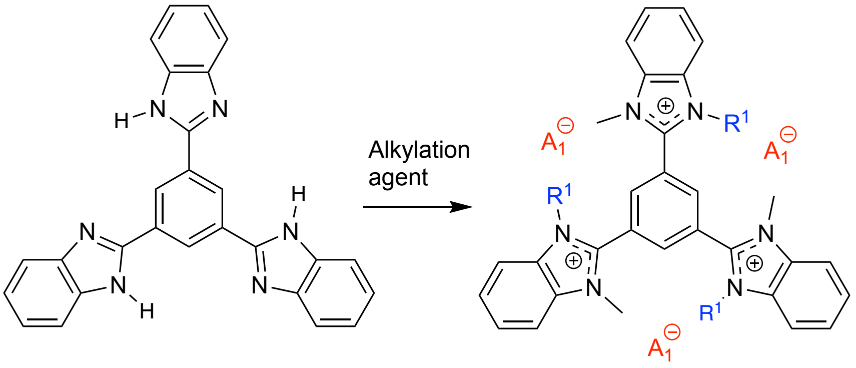

56

77: R^1 = -methyl, A = -I^-
78: R^1 = -methyl, A = -OTf^-
79: R^1 = -methyl, A = -BF_4^-
80: R^1 = -ethyl, A = -I^-
81: R^1 = -ethyl, A = -OTf^-
82: R^1 = -ethyl, A = -BF_4^-
83: R^1 = -octyl, A = -OTf^-

Scheme 16. Chemical modification of 1,3,5-tris(N-methylbenzimidazolyl)benzene ***56****.*

By using the respective triflate alkylating agent the triflate salts (**TriDiMeBim)$^{3+}$(OTf)$_3$**$^{1-}$ (**78**), **81** and **83** were obtained. Trimethyloxonium tetrafluoroborate and triethyloxonium tetrafluoroborate were used to obtain the tetrafluoroborate salts **79** and **82**, respectively. Using methyl or ethyl iodide as alkylating agents organic salts **77** and **80** were obtained.

Hexa(4-phenyl-2-benzimidazolyl)benzene **71** was transformed into a hexacationic molecule in a similar fashion to the synthesis of tricationic molecules. **71** was dissolved in DMF, deprotonated by sodium hydride and subsequently reacted with methyl iodide to obtain hexa(4-phenyl-2-methylbenzimidazolyl)benzene **HexaMeBim** (**85**)(Scheme 17) in 42 % yield.

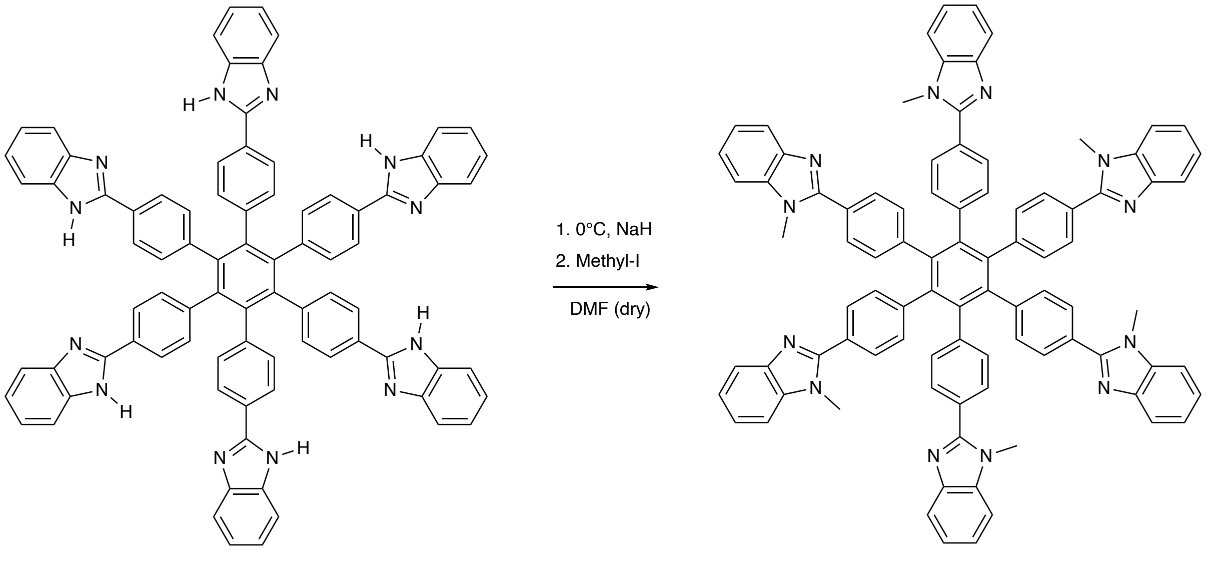

71 **85**

*Scheme 17. Synthesis of hexa(4-phenyl-2-methylbenzimidazolyl)benzene **85**.*

In a second reaction **85** was dissolved in acetonitrile and reacted with an excess of methyl triflate to give the organic salt **(HexaDiMeBim)$^{6+}$(OTf)$_6$$^{1-}$** (**86**)(Scheme 18).

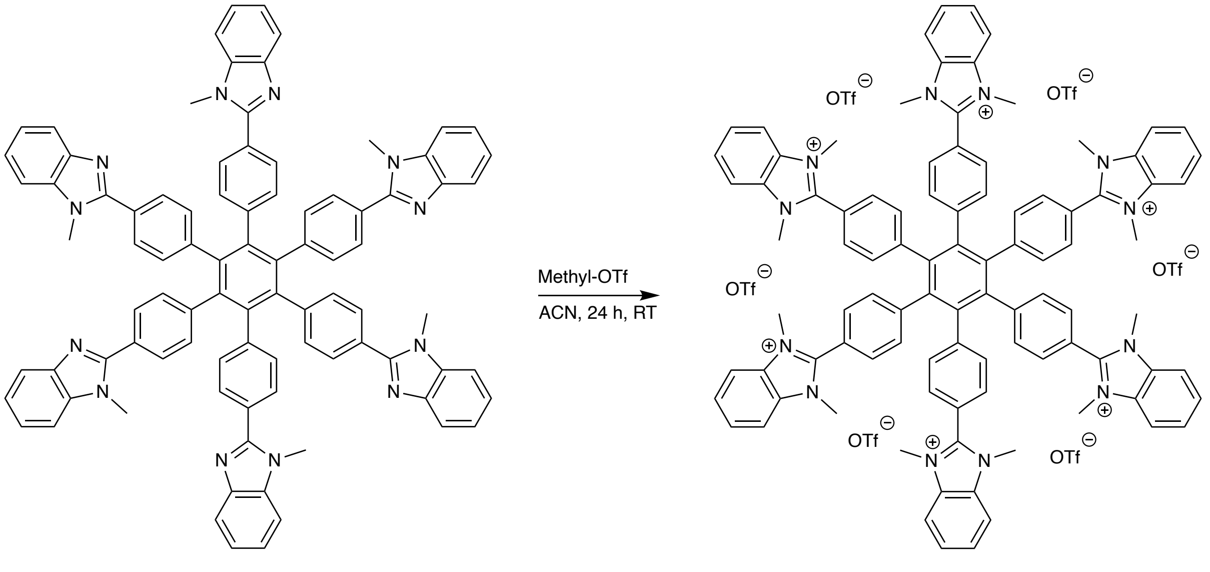

85 **86**

*Scheme 18. Synthesis of the organic salt (hexa(4-phenyl-2-dimethyl-benzimidazolyl)benzene **86**.*

A one-step reaction from hexa(4-phenyl-2-benzimidazolyl)benzene **71** to **86** is not successful with alkylating agents such as methyl triflate or methyl iodide. Proton NMR studies of DMSO-*d*6 samples of the reaction mixture showed a shift of all peaks in the spectrum compared to the ^{1}H NMR spectrum of the starting material **71** (both in DMSO-*d*6). However, no peak for the expected *N*-methyl groups was found. Also, mass spectroscopy did not show any signals that could be assigned to the organic salt **86**. The C_6 symmetric pyridine molecules **46** and **47** were used to synthesize two more organic salts **(HexaMePy)$^{6+}$(OTf)$_6^{1-}$** (**87**) and **(HexaMePyCC)$^{6+}$(OTf)$_6^{1-}$** (**88**) with different geometries. The *N*-alkylation of both molecules was in principle comparable with the synthesis of the previously discussed C_3 symmetric molecules (Scheme 19).

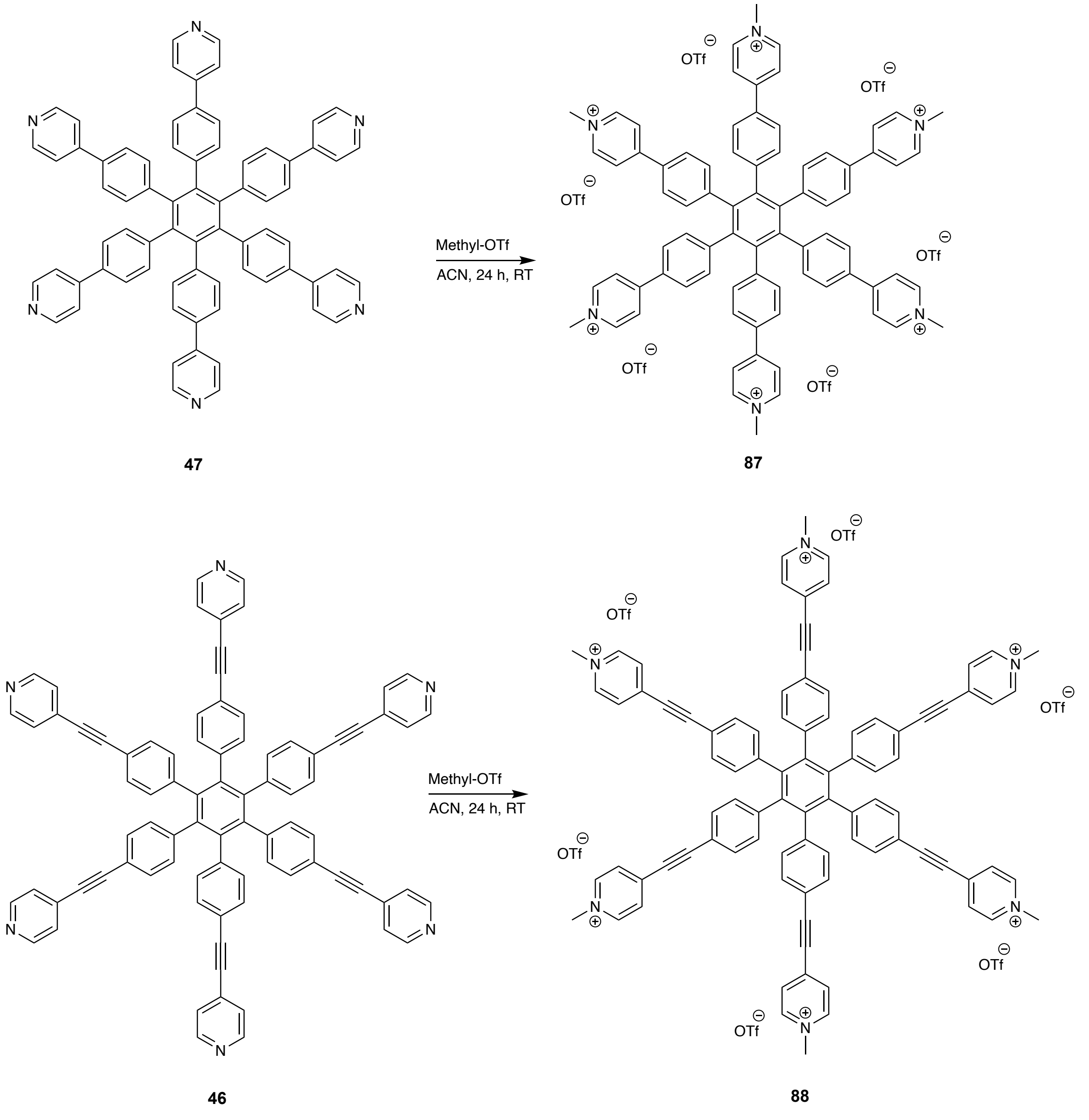

47

87

46

88

*Scheme 19. Synthesis of hexapyridyl organic salts **87** and **88**.*

Table 1 gives an overview of all performed *N*-alkylation reactions to obtain monocationic, tricationic and hexacationic molecules. The product yields vary between 38% and 88%. Lower product yields are observed by using methyl triflate as alkylation agents instead of trimethyloxonium tetrafluoroborate. By increasing the size of the alkyl chain (-methyl, -ethyl, -octyl) a decreasing of the product yield of the respective triflate- and tetrafluoroborate salts was observed. In contrast to that a higher yield was obtained with ethyl iodide compared with methyl iodide. Comparing the methylation reactions of 2-methylbenzimidazole **54** and 2-

phenylbenzimidazole **55** with the synthesis of the organic salts **78**, **86,** **87** and **88** (always methyl triflate as alkylation agent), no significant decrease of the overall product yield was observed even though six alkylation reactions were completed in one synthetic step, instead of just one.

Table 1. Overview of all performed N-alkylation reactions to form cationic molecules. The neutral precursors were suspended in dry acetonitrile before the alkylating agent was added. The reaction mixture was stirred for 24 hour at room temperature

Molecule	Cation charge	Alkylation agent	Yield (in %)
54	1+	Methyl triflate	60
55		Methyl triflate	38
78	3+	Methyl triflate	60
81		Ethyl triflate	59
83		Octyl triflate	30
79		Trimethyloxonium tetrafluoroborate	88
82		Triethyloxonium tetrafluoroborate	58
77		Methyl iodide	30
80		Ethyl iodide	58
86	6+	Methyl triflate	72
87		Methyl triflate	66
88		Methyl triflate	47

5.1.5 Theoretical Characterization of Charged π-conjugated Systems

Information about the molecular geometries and the electronic structures of the compounds were obtained by DFT calculations (PBE[296], GGA functional/ CASTEP basis set within Material Studios framwork). The geometry optimized structures of **MeBim** (**54**), **PhBim** (**55**), **TriBim** (**56**) and **HexaBim** (**71**) are shown in Figure 18. 2-Methylbenzimidazole **MeBim** and 2-phenylbenzimidazole **55** are planar molecules, indicated by a dihedral angle of 7.4° between the phenyl and the benzimidazole plane for **55** (Table 2). Its planar geometry would suggest an increased interaction *via* intermolecular interactions that scale with size, such as dispersion forces, compared with 2-methylbenzimidazole **54**. The polybenzimidazole system **56** is characterized by an average dihedral angle of 5.4° and therefore almost flat. The C_6 symmetric **71** has a higher average dihedral angle of 8.3° and in addition an average dihedral angle between the core benzene and the six surrounded phenyl rings of 60° and is therefore propeller shaped.

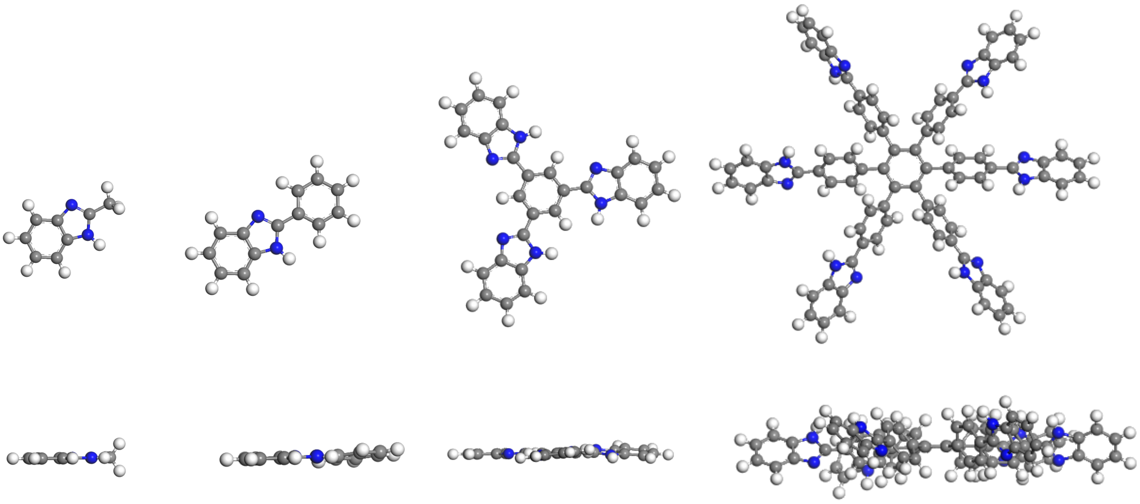

MeBim (54) **PhBim (55)** **TriBim (56)** **HexaBim (71)**

*Figure 18. Optimized structures (PBE[296], GGA functional/ CASTEP basis set within Material Studios framework) of neutral molecules **MeBim (54)**, **PhBim (55)**, **TriBim (56)** and **HexaBim (71)**.*

The polybenzimidazole systems are propeller shaped. The average dihedral angle between the phenyl and the benzimidazole plane varies significantly within the series of molecules. The dependence of the average dihedral angle on the redox state was explored by performing geometry optimizations of the all systems after addition of an additional electron, i.e. after reduction (Table 2). The neutral molecule **54** and its reduced derivative **54**$^{1-}$ does not show any significant structural change. The other neutral molecules **55**, **56** and **71** however get more planer after a one-electron transfer, which is characterized by a decrease of the average dihedral angle.

This planarization effect is strongest for **55**, defined by the highest ratio between the average dihedral angles before and after a one-electron transfer. Also, the monobenzimidazolium and polybenzimidazolium molecules were studied computationally before and after reduction (one-electron transfer). The monocationic molecule **(TriMeBim)**$^{1+}$ (**76**$^{1+}$) shows no structural change after a one-electron transfer. The optimized geometry of **(DiMePhBim)**$^{1+}$ (**75**$^{1+}$) is strongly twisted, characterized by an average dihedral angle of 56° between the benzene ring and the appended benzimidazolium moieties (Table 2, Figure 19). In contrast to the neutral molecule **56** is the tricationic molecule **(TriDiMeBim)**$^{3+}$ (**78**$^{3+}$) propeller-shaped with an average dihedral angle of 58°. Hexacationic **(HexaDiMeBim)**$^{6+}$ (**86**$^{6+}$) is twisted between the benzimidazolium moiety and its neighboring benzene ring with an average dihedral angle of 51°. The hexa-benzene core is propeller-shaped with an average dihedral angle of 75° (Table 3).

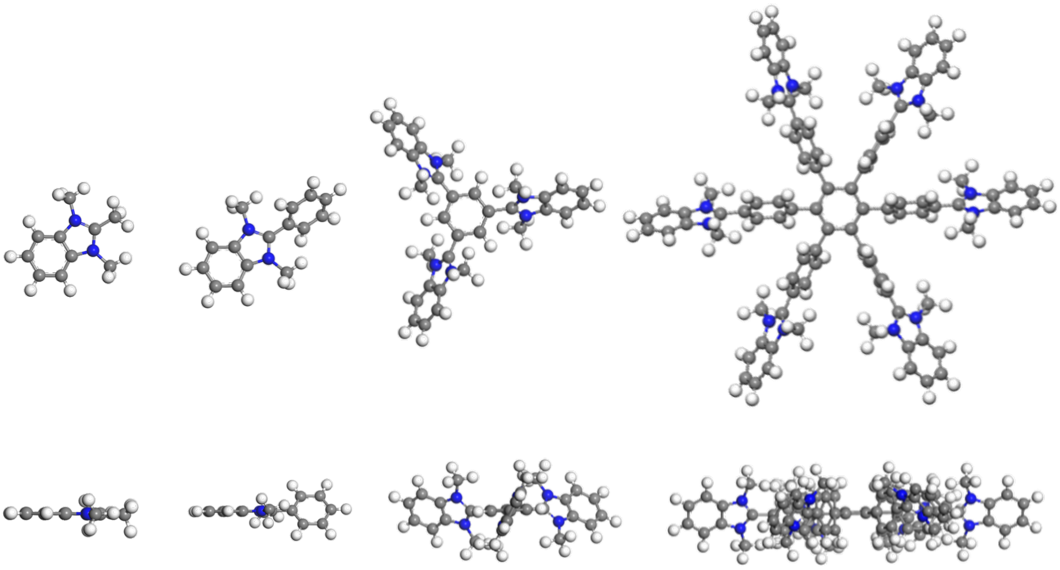

(TriMeBim)$^{1+}$ (76^{1+}) **(DiMePhBim)$^{1+}$ (75^{1+})** **(TriDiMeBim)$^{3+}$ (78^{3+})** **(HexaDiMeBim)$^{6+}$ (86^{6+})**

*Figure 19. Optimized structures (PBE[296], GGA functional/ CASTEP basis set within Material Studios framework) of monocationic **(TriMeBim)$^{1+}$** (76^{1+}) and **(DiMePhBim)$^{1+}$** (75^{1+}) as well as tricationic **(TriDiMeBim)$^{3+}$** (78^{3+}) and hexacationic **(HexaDiMeBim)$^{6+}$** (86^{6+}).*

Table 2. Overview of the average dihedral angles between the benzimidazolium moieties and the benzene ring in 2´-position

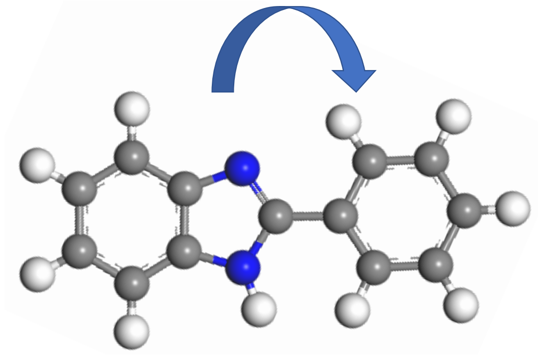

	Avarage dihedral angles (in°)		
Compound	n+	(n-1)+	n+/(n-1)+
75	56	30	1.9
78	58	50	1.2
86	51	45	1.1
55	7.4	0.3	22.0
56	5.4	1.6	3.4
71	8.3	8.4	0.9

Table 3. Overview of the average dihedral angles between the central benzene ring and its six surrounded benzene rings in C₆ symmetric ***HexaBim*** *and* ***(HexaDiMeBim)***$^{6+}$

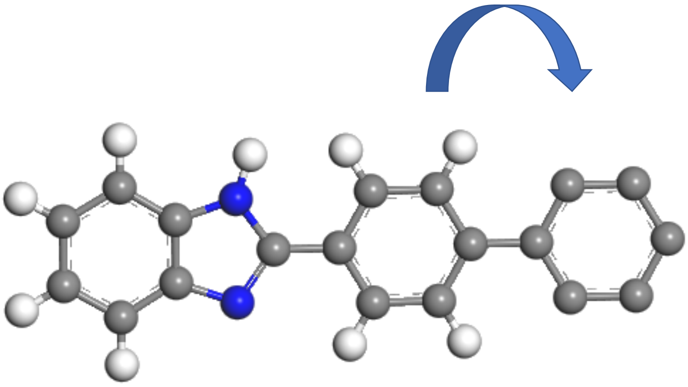

	Avarage dihedral angles (in°)		
Compound	n+	(n-1)+	n+/(n-1)+
71	60	55	1.1
86	75	64	1.2

The monocationic ion **75**$^{1+}$ shows the strongest flattening effect when compared to **78**$^{3+}$ and **86**$^{6+}$. The LUMO of tricationic molecule **78**$^{3+}$ is mainly bonding between the central benzene and the benzimidazolium moieties (Figure 20A). The bonding trait of the LUMO is responsible for a flattening of the overall geometry, when one electron is added. This will be discussed later on.

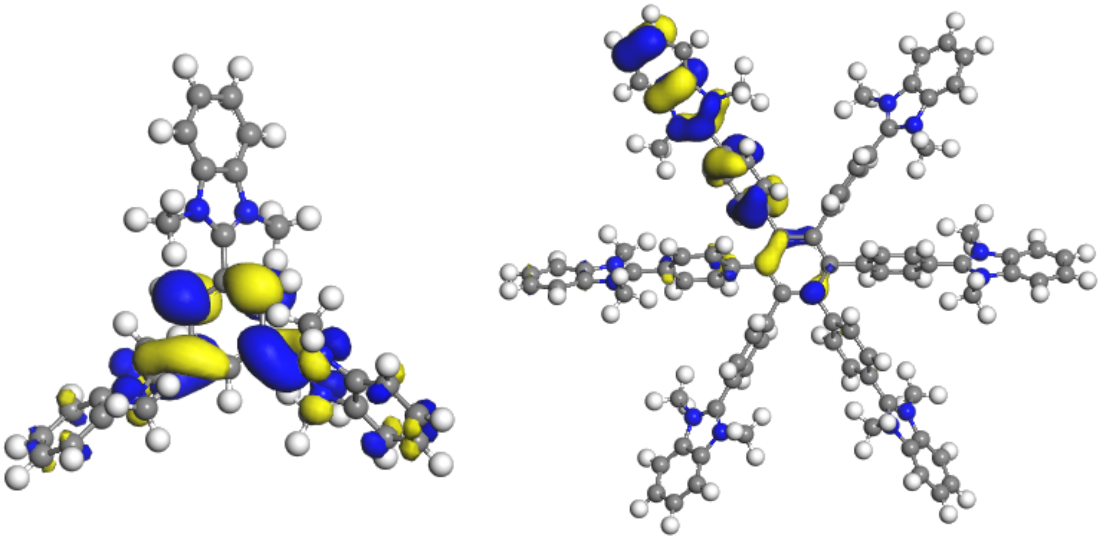

Figure 20. LUMO of A) tricationic ***78***$^{3+}$ *(PBE*[296]*, GGA functional/ CASTEP basis set within Material Studios framework) with singlet spin multiplicity and B) hexacationic* ***86***$^{6+}$ *with triplet spin multiplicity (blue: positive phase of MO, yellow: negative phase of MO).*

The same flattening effect is observed in the case of molecule **86**$^{6+}$. The LUMO of **86**$^{6+}$ is bonding mainly on one of the six molecular branches (Figure 20B). The addition of one electron to the hexacation **86**$^{6+}$ is therefore resulting in both a decrease of, the outer and inner average dihedral angles. The overall geometry of **86**$^{5+}$ is however still very twisted. An overall flatter geometry of these π-conjugated molecules is more likely to strengthen the interaction with graphene, because the distance between graphene and the molecules is decreased, leading to an increase of intermolecular interactions.[294] The electron affinities of the neutral and cationic π-conjugated molecules were calculated and are discussed together with the electrochemical analysis of these compounds in the next chapters.

5.1.6 Photophysical Characterization of π-conjugated Systems

The synthesized organic salts such as **(TriDiMeBim)**$^{3+}$**(OTf)**$_3^{-1}$ (**78**), **(HexaMePy)**$^{6+}$**(OTf)**$_6^{-1}$ (**87**), **(HexaMePyCC)**$_6^{6+}$**(OTf)**$^{-1}$ (**88**) and **(HexaDiMeBim)**$^{6+}$**(OTf)**$_6^{-1}$ (**86**) and their neutral precursors were studied photophysically as part of a collaboration with Philipp Rietsch. An overview of the photophysical data of these compounds is shown in Table 4. All compounds show an absorption in the UV region and emit between 374 nm and 392 nm. The emission spectrum of hexacationic molecule **87** is bathochromically shifted to 452 nm. The fluorescence quantum yields were studied in solid state and solution (DMSO). Interestingly, the organic salts are generally non-emissive in solution (Φ_{fl}), but emissive in the solid state (Φ_{fl}^{SS}), whereas the opposite is observed for the neutral molecules. This phenomena can be ascribed to aggregation-induced-emission, due to the restriction of intramolecular rotations and the restriction of intramolecular vibrations, which can be caused by π-π stacking.[297] For instance, the neutral-organic salt pair of **TriBim** (**56**) and **78** has Φ_{fl} of 43 % and <1 %, respectively, but reversed Φ_{fl}^{SS} of 2 % (**56**) and 26 % (**78**). There are however two exceptions: The two hexa-cationic compounds **88** and **86**. The organic salt **88** is emissive both in solution (Φ_{fl} = 43 %) and the solid state (Φ_{fl}^{SS} = 18 %). And the organic salt **86** shows very weak emission in solution (Φ_{fl} = 2 %) and the solid state (Φ_{fl}^{SS} = < 1 %). The low Φ_{fl}^{SS} of the neutral compounds is most likely caused by π-π stacking, leading to non-radiative relaxation through excimer formation. The counterions and different crystalline structures probably limit that relaxation pathway in the cationic compounds. The lifetimes of the two C_3 symmetric compounds **56** and **78** are remarkably long, 8.0 ns and 6.9 ns, compared to the relative short lifetimes of all other compounds, which are between 1.0 ns (**46** and **88**) and 1.6 ns (**71**). The fluorescence lifetime in the solid state (τ_{ss}) is emission wavelength dependent for **46**, **88** and **56**. As one example, **88** shows a τ_{ss} of 2.5 ns at 400 nm and 3.8 ns at 500 nm. Weather two emissive species are formed in the crystal, or different transitions arise due to the restriction of rotations will be part of future investigations.

Table 4. Overview of the photophysical properties of the title compounds ***56 (TriBim)****,* ***71 (HexaBim)****,* ***85 (HexaMeBim)****,* ***47 (HexaPy)*** *and* ***46 (HexaPyCC)*** *as well as organic salts* ***78 (TriDiMeBim)$^{3+}$(OTf)$_3$$^{1-}$****,* ***87 (HexaMePy)$^{6+}(OTf)_6$$^{1-}$****,* ***88 (HexaMePyCC)$^{6+}$(OTf)$_6$$^{1-}$*** *and* ***86 (HexaDiMeBim)$^{6+}$(OTf)$_6$$^{1-}$****. The value for the normalized Dimroth-Reichardt parameter ENT was taken from literature.*[298]

				Solid		In solution[a]	
Compound	λ_{abs} (nm) (ε (M-1cm-1))	E_{gap}[f] (eV)	λ_{em} (nm)	Φ_{Fl}^{SS} (%)	τ (ns)	Φ_{Fl} (%)	τ (ns)
56	317 (6329)	3.56	380	2	0.4-3.0	43.0	8.0
78	290 (4126)	3.64	392	26	2.8	<1	6.9
71	319 (23070)	3.49	392	<1	n.a.	56.0	1.6
85	304 (19921)	3.57	391	<1	n.a.	33.0	1.4
86	284 (18445)	3.67	391	<1	n.a.	2.0	1.3
47	278 (17785)	3.80	374	<1	n.a.	55.0	1.3
87	321 (21377)	3.21	452	26	6.9	0.0	n.a.
46	294/312 (13082/13581)	3.68/3.58	380	5	0.8[b]-1.5[c]	54.0	1.0
88	270/350 (8257/10495)	3.81/3.40	387	18	2.5[d]-3.8[e]	43.0	1.0

[a] In DMSO Emission. [b] Emission 400 nm, Excitation 330 nm. [c] Emission 460 nm, Excitation 330 nm. [d] Emission 400 nm, Excitation 330 nm. [e] Emission 500 nm, Excitation 330 nm. [f] Calculated optical band gap.[299]

5.1.7 Electrochemical Characterization of π-conjugated Systems

To examine the effect of **(TriMeBim)$^{1+}$(OTf)$^{1-}$** (**76**), **(DiMePhBim)$^{1+}$(OTf)$^{1-}$** (**75**), **(TriDiMeBim)$^{3+}$(OTf)$_3$$^{1-}$** (**78**) and **(HexaDiMeBim)$^{6+}$(OTf)$_6$$^{1-}$** (**86**), as well as their neutral precursors, on the adsorption strength and doping effect on graphene, their redox potentials were investigated by cyclic voltammetry. The reduction potentials obtained for the series of imidazolium ions are given in Table 5. In comparison, the neutral precursor molecules have their reduction potential at less negative potentials compared with the cationic molecules. In the series of cationic π-conjugated molecules, the tricationic molecule **78^{3+}** and the monocationic molecule **75^{1+}** have the least negative reduction potential at $E_{red,1}$ = -1.70 V (**78^{3+}**) and $E_{red,1}$ = -1.65 V (**75^{1+}**) an can therefore be reduced most effectively by graphene, after deposition, in comparison to the other molecules (Figure 21).

The simulated CV spectra of tricationic molecule **78^{3+}** shows three separate reduction peaks and first electron transfer is pseudo reversible (at high sweep rates). No other molecules show reversible electrochemistry due to chemical follow-up reactions, probably related to conformational changes. A chemical step follows the first reduction peak (EC mechanism) associated with a small rate constant and the subsequent second and third electron transfer take place at different potentials. From the simulations a diffusion coefficient of $2.5 \cdot 10^{-6}$ cm^2/s was obtained. As previously discussed is the LUMO of **78^{3+}** localized between the central benzene and the benzimidazolium moieties (Figure 20). The electron added during reduction is therefore localized in the core of the molecule. A second electron transfer reaction would however disturb this symmetry and therefore is the second reduction potential of **78**$^{3+}$ at less negative potentials than the first reduction potential. Therefore, we see three different reduction peaks for **78**$^{3+}$.

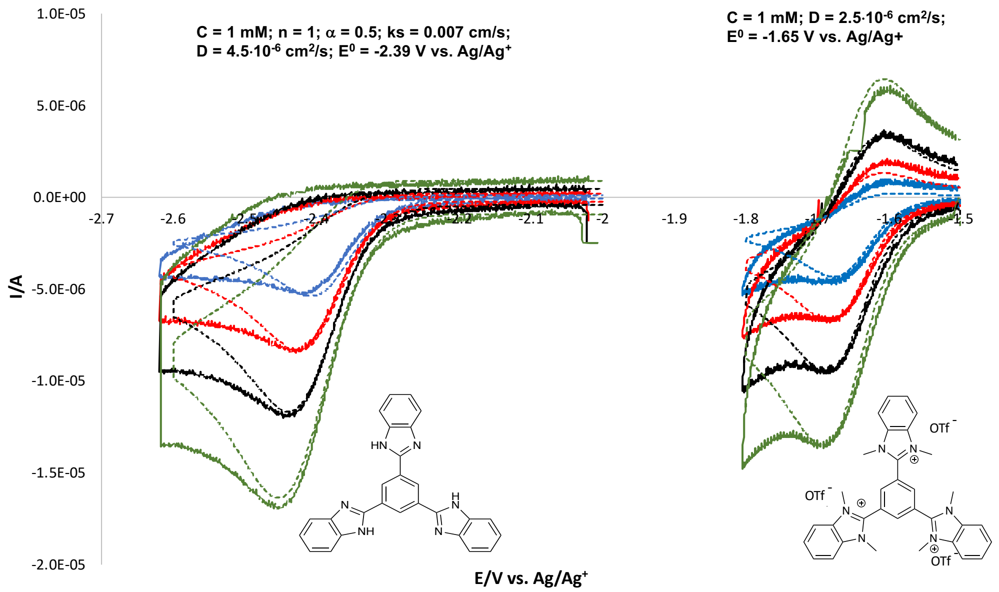

Figure 21. Cyclic voltammograms of the first reduction peak of ***TriBim*** *(left side) and* ***(TriDiMeBim)***$^{3+}$ *(right side) at different sweep rates (green: 1000 mVs*$^{-1}$*, black: 500 mVs*$^{-1}$*, red: 250 mVs*$^{-1}$*, blue: 100 mVs*$^{-1}$*) in DMF with 0.1 M (TBA-BF*$_4$*) vs. Ag/Ag*$^+$*. The dashed lines show the simulated cyclic voltammograms. An EC mechanism was used in the simulation with a first order chemical reaction following the electron transfer step for both molecules.*

Table 5. Experimental reduction potentials $E_{1/2}$ *(in V) and electron affinities EA (in eV) calculated in the absence of counter ions. [a] obtained by simulation.*

Compound	$E_{1/2}$ vs Ag/Ag+ (V)	E^0 [a] vs Ag/Ag+ (V)	*EA* (eV)
Neutral			
TriMeBim	-2.95	-2.6 – -2.8	1.1
DiMePhBim	-2.70	-2.68	-0.2
TriBim	-2.45	-2.39	1.5
HexaBim	-2.64	-2.3 – -2.4	0.7
Cationic			
(TriMeBim)$^{1+}$	-2.45	-2.28	-4.0
(DiMePhBim)$^{1+}$	-1.65	-1.58	-4.2
(TriDiMeBim)$^{3+}$	-1.70	-1.65	-6.9
(HexaDiMeBim)$^{6+}$	-2.00	-1.90	-9.5

The first reduction event of **86**$^{6+}$ and its neutral derivative **HexaBim (71)** come at less negative potentials compared with the C_3 symmetric derivatives **78**$^{3+}$ and **TriBim (56)**. The simulated CV spectra of hexacationic **86**$^{6+}$ shows no reversibility for the first electron transfer at high sweep rates. It was assumed that the electrochemical reduction events of hexacationic **86**$^{6+}$ follow the same diffusion coefficient as obtained for tricationic molecule **78**$^{3+}$ and the data could be therefore fitted into six consecutive electron transfer reactions followed by a chemical step. All six electron transfer reactions occur on similar redox potentials. An explanation here can be also the already discussed LUMO of hexacationic **86**$^{6+}$, which is localized on one of the six molecular branches of the molecule (Figure 22). This shows that the MO from the molecular branches are more or less independent from each other and could therefore possibly react in a similar manner upon an electron transfer reaction. A second electron transfer reaction would affect another molecular branch and still leaves the molecular core largely unaffected. The same goes one for further electron transfer reactions. The monocationic molecule **75**$^{1+}$ shows no reversibility with a considerably higher diffusion coefficient of $7\cdot10^{-6}$ cm^2 s^{-1}, which is not unusually high for organic compounds. The other monocationic molecule **76**$^{1+}$ shows an irreversible reduction potential at even more negative potentials compared with the other cationic π-conjugated molecules. The results show that the redox potential are coupled in some way to the number of electrons. The tricationic molecule **78**$^{3+}$ is more easily reduced by graphene then hexacationic **86**$^{6+}$. However, also the geometrical aspects play an important role in the reduction of these cationic π-conjugated systems as previously discussed.

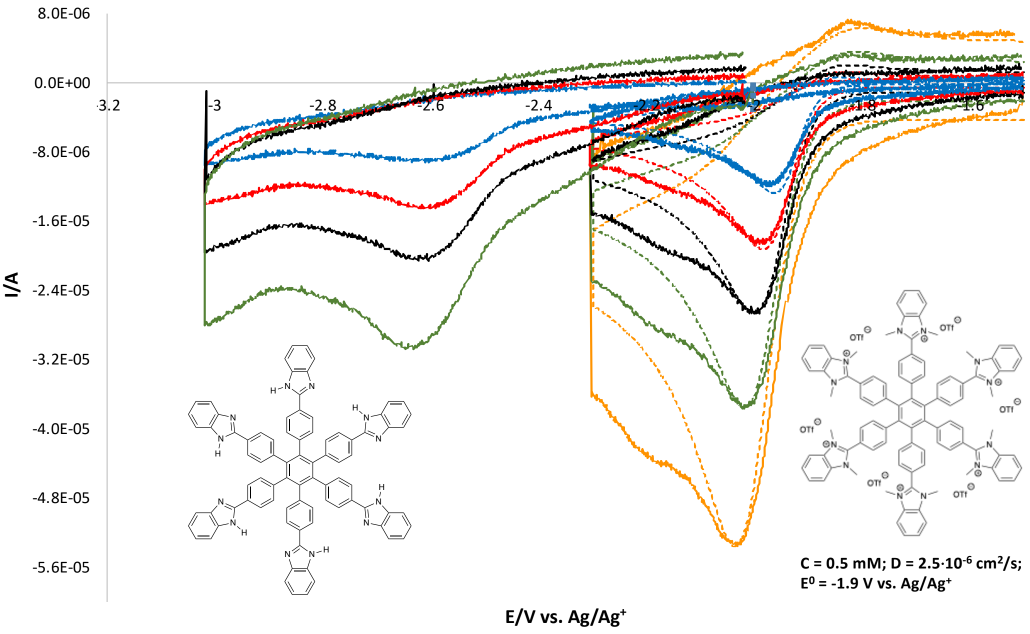

Figure 22. Cyclic voltammograms of the first reduction peak of ***HexaBim*** *(left side) and* ***(HexaDiMeBim)***$^{6+}$ *(right side) at different sweep rates (orange: 2000 mVs*$^{-1}$*, green: 1000 mVs*$^{-1}$*, black: 500 mVs*$^{-1}$*, red: 250 mVs*$^{-1}$*, blue: 100 mVs*$^{-1}$*) in DMF with 0.1 M (TBA-BF*$_4$*) vs. Ag/Ag*$^+$*. The dashed lines show the simulated cyclic voltammograms. Six consecutive one electron transfers were followed by a first order chemical reaction following the last electron transfer step (EEEEEEC mechanism).*

5.2 Study of Interactions between Charged π-conjugated Systems and Graphene

5.2.1 Non-Covalent Functionalization of Graphene

As a next step, the obtained molecular structures from chapter 4.1 are deposited onto graphene or MoS_2 and the properties of these two-dimensinal hybrid materials were studied. Polycyclic aromatic hydrocarbons,[300] imidazolium and pyridinium salts have a relatively high vapour pressure. Sublimation of these molecules cannot be performed easily with standard laboratory pumps. Drop-casting a solution of the organic salt **(TriDiMeBim)$^{3+}$(OTf)$_3^{1-}$** (**78**) onto the graphene sample is also not the method of choice, because the molecules crystallize at the edges of the silica wafer during the evaporation of the solvent, leaving behind a heterogenous layer on the graphene sample. Instead, a CVD graphene wafer can be non-covalently functionalized by incubation of the graphene sample in a solution of the molecule (Figure 23). The attraction between the π-conjugated molecules and graphene leads to a homogeneous deposition of the molecules on graphene surface. For that purpose a 12 mM solution of the respective analyte in triple distilled methanol was prepared and the graphene sample was incubated in the solution.

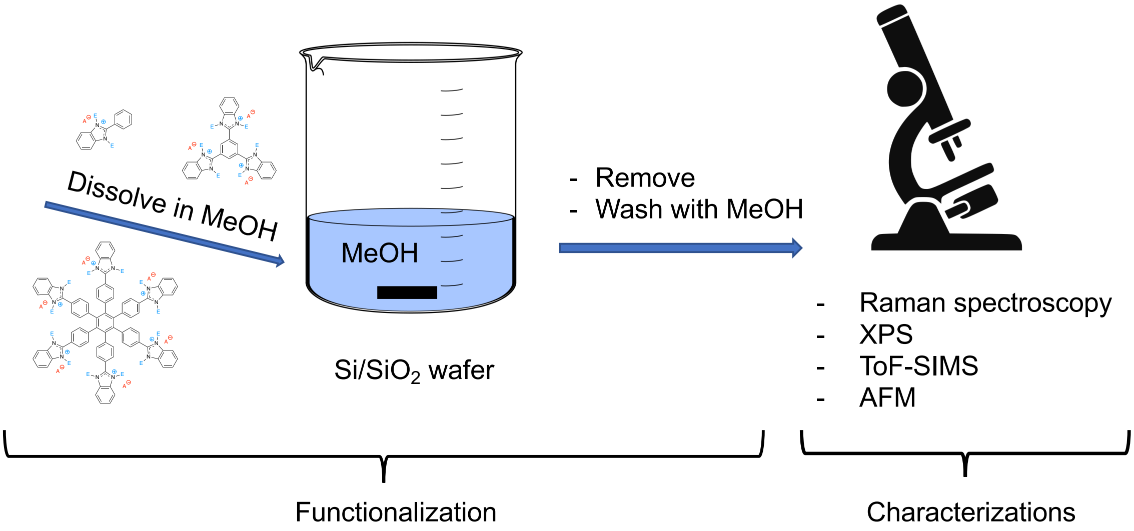

Figure 23. Functionalization of a graphene wafer via non-covalent functionalization with organic salts. The cationic molecules and their derivatives were dissolved in methanol and a graphene wafer was incubated in the solution at room temperature. The wafer was removed after two hours and was rinsed with methanol before subsequent further analyzation.

I found that an incubation time of two hours at room temperature was sufficient to non-covalently functionalize the graphene substrates. After incubation, the sample was removed from the methanolic solution and washed twice by rinsing the wafer with triply distilled methanol to remove excess of molecules and other impurities like dust from the silica wafer. The prepared samples were stored at 4 °C in a fridge before further characterization. Raman and AFM studies of MoS_2 samples before and after non-covalent functionalization with the same protocol resulted in a change in position of the exfoliated MoS_2 flakes on the wafer.

Therefore, a modified protocol of the already described procedure was used. A wafer with mechanically exfoliated MoS_2 was drop casted with a 12 mM methanolic solution of the appropriate molecule. After 10 seconds, the excess of the solution was absorbed by tissue paper. Using this modified method of the sample preparation Raman and PL studies with the same flakes before and after functionalization could be successfully performed.

5.2.2 Atomic Force Microscopy Studies of Functionalized Graphene

AFM studies were performed to analyze non-covalently functionalized graphene. Silica wafer coated with oxo-G were subsequently reduced. The here used r-oxo-G is graphene with a density of lattice defects of approximately 0.5-0.8%, according to statistical Raman spectroscopy.[131] Before further functionalization, the thickness of r-oxo-G is 2.5 nm (Figure 24). The literature value for one single layer of graphene ranges between 0.4 and 1.7 nm for different sample preparations.[301] The observed thickness of the graphene sample is most likely higher due to species trapped between the substrate and the basal plane of reduced oxo-G or by adsorbed byproducts or residues from the reduction process. Since oxo-G is reduced on the substrate, which leads to C-O cleavage of functional groups between the substrate and the basal plane, water (from epoxy and hydroxyl groups) and sulfate-species (from organosulfate) are partially trapped.

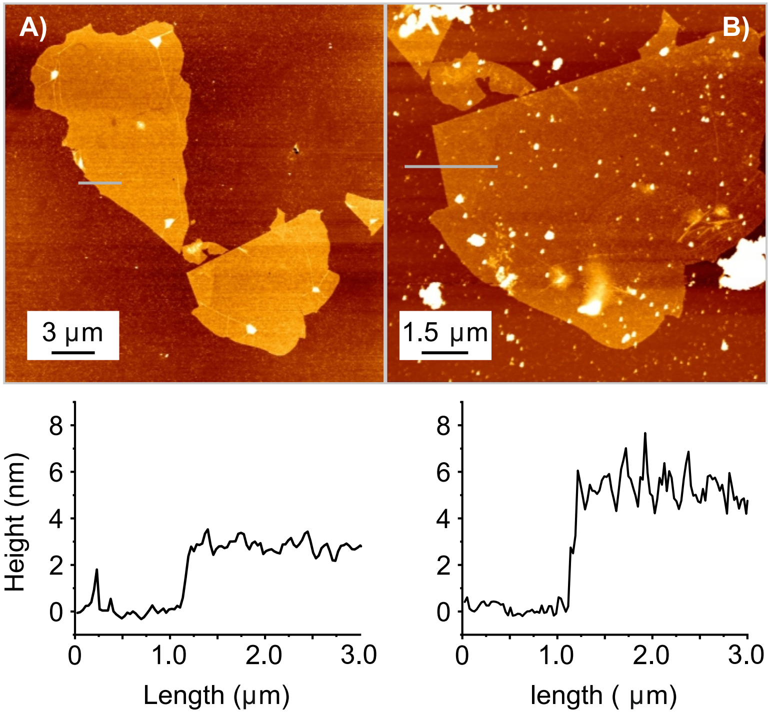

Figure 24: AFM image of a silica wafer (Si/300nm SiO_2) A) coated with oxo-G and B) after functionalization with the organic salt ***(TriDiMeBim)$^{3+}$(OTf)$_3^{1-}$ (78)****. The respective height profiles of an oxo-G flake along the grey line is shown below the AFM images.*

Previous studies on reduced oxo-G showed that under ambient conditions species that lead to a decrease of thickness to 1.2 nm can be removed.[238] Although the measured height appears to be quite high, adsorption of molecules is still possible. After functionalizing r-oxo-G non-covalently with organic salt **(TriDiMeBim)$^{3+}$(OTf)$_3$$^{1-}$** (**78**), the thickness of the hybrid material r-oxo-G/**78** increases to about 5 nm.

The surface of the r-oxo-G flake is overall homogeneously functionalized, which can be seen from the surface roughness. In addition to the cations there is also the counterions of **78** on the surface of the graphene sample (see chapter 5.2.6). This shows that the protocol of non-covalently functionalizing graphene results in a surface functionalization and not the formation of clusters on the surface. AFM studies with the neutral C_3 symmetric molecule **TriBim** (**56**) show that it also binds non-covalently to r-oxo-G flakes. The thickness of the graphene flakes increases from 2.5 nm to 3.5 nm. The smaller overall thickness compared with r-oxo-G/**78** is in agreement with the flatter structure of molecule **56** compared with tricationic **78** and the fact that no additional counterions are on the r-oxo-G/**56** materials.

5.2.3 Raman Analysis of Functionalized Graphene

Molecules non-covalently bound to graphene can dope graphene.[302-303] Therefore, the doping effect of cationic π-conjugated molecules on graphene was studied.[217, 230] Raman spectra of CVD graphene and functionalized CVD graphene were compared with Raman spectra of the molecules itself on a silica wafer. The Raman spectra of the organic salts **(TriMeBim)$^{1+}$(OTf)$^{1-}$** (**76**), **(DiMePhBim)$^{1+}$(OTf)$^{1-}$** (**75**) and **(TriDiMeBim)$^{3+}$(OTf)$_3$$^{1-}$** (**78**) on a silica substrate are different but also show similar trends (Figure 25, A-C). All cationic molecules show aromatic C-H bond vibrations in the region between 2980-3020 cm^{-1}, C=N bond vibrations between 1610-1680 cm^{-1} and aromatic ring vibrations between 1450-1610 cm^{-1}. The bond vibrational signals at 1170-1410 cm^{-1} and between 670-780 cm^{-1} stem from the C-F and C-S bonds, respectively, in the triflate counterions. CVD graphene on silica substrate shows two distinct Raman peaks, the G peak at around 1584 cm^{-1} and the 2D peak at around 2700 cm^{-1} (Figure 25D).

CVD graphene non-covalently functionalized with **76** looks like the Raman spectrum of CVD graphene and no significant change in position or geometry of the characteristic G and 2D peaks was observed (Figure 25E). On the other hand, the samples with cationic molecules **75** and **78** non-covalently bound to CVD graphene give rise to spectra featuring new signals and shifts and broading of the characteristic graphene signals. For both molecules broad and overlapping signals between 1200-1600 cm^{-1} are observed in the (Figure 25F-G). Broadening could be due to molecular decomposition but this was avoided by adjusting the applied laser power (1.7 mW). Usually an inhomogeneous broadening is observed for amorphous samples, where the chemical composition, crystal size, morphology or local environmental can vary significantly for different areas on the sample. A change in these parameters, which can be also caused by the interaction with graphene itself, causes a slightly different Raman scattering, which leads to a shifted Raman signal. The overlapping of these slightly different signals is observed as a peak broadening. The broadening of the molecular peaks might instead arise from the interaction of the tricationic molecules with graphene and are therefore not as sharp as in the case of silica as the substrate. The assignment of Raman peaks of small molecules bound non-covalently to graphene have not yet been intensively studied in the literature.[304] The absence of these peaks in the case of the functionalized graphene with monocationic **76** might mirror the weaker attractions between the smaller and less charged molecule and graphene. Analysis of the shift of the position of the G peak, which is sensitive to doping,[235] is not reliable due to the overlapping signals.

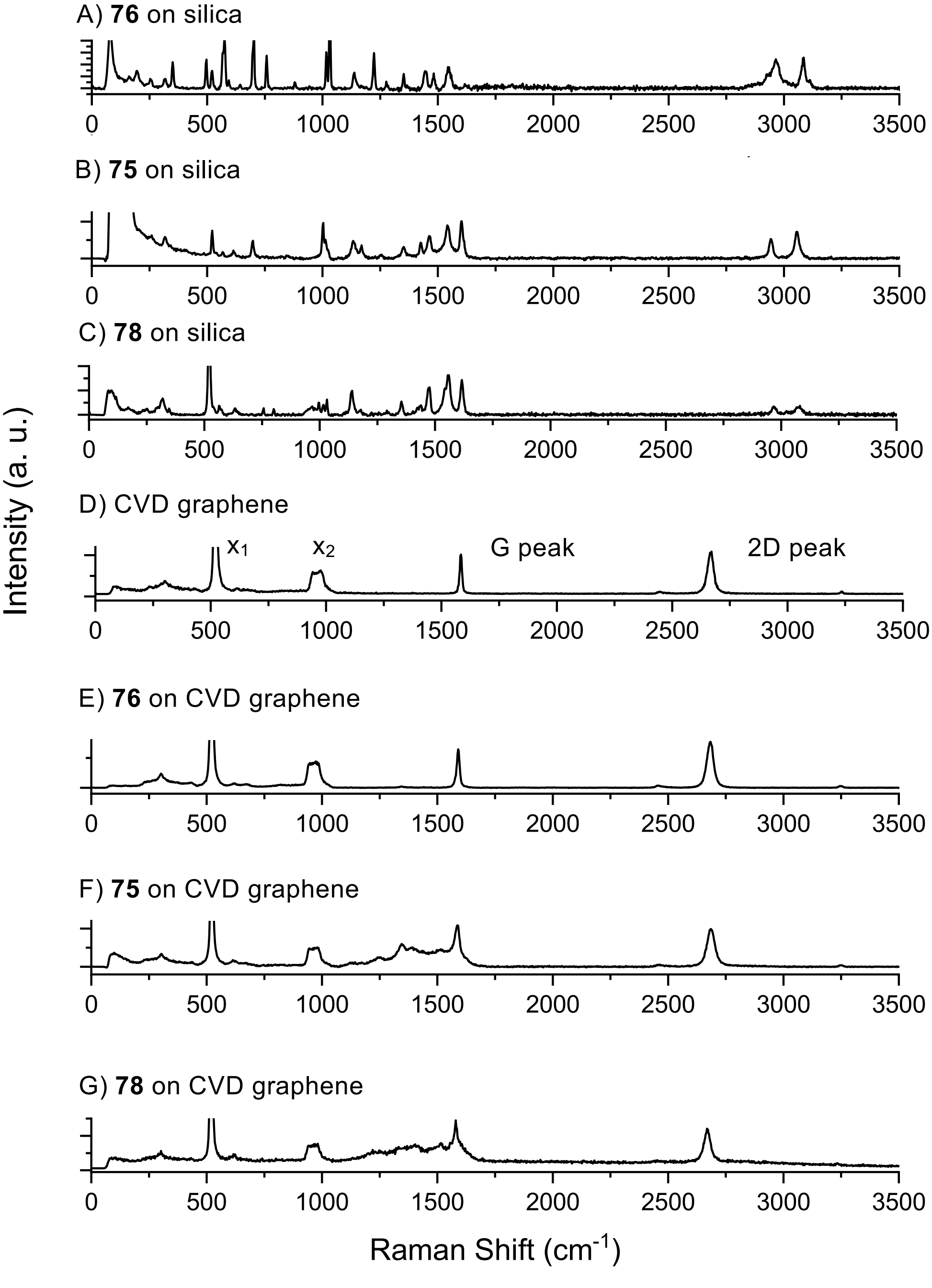

Figure 25. Raman spectra of organic salts A) ***76*** ***(TriMeBim)$^{1+}$(OTf)$^{1-}$***, *B)* ***75*** ***(DiMePhBim)$^{1+}$(OTf)$^{1-}$*** *and C)* ***78*** ***(TriDiMeBim)$^{3+}$(OTf)$_3$$^{1-}$*** *as well as D) CVD graphene. E) Organic salt* ***76*** *on CVD graphene, F) organic salt* ***75*** *on CVD graphene and G) organic salt* ***78*** *on CVD graphene. As substrate for all samples silica wafer (300 nm of SiO_2 on surface) were used showing at x^1 = 520 cm^{-1} the signal for crystalline silicon and at x^2 = 900-1000 cm^{-1} the signal for amorphous silicon dioxide on the silicon surface.[235] The signal intensities from x^1 are not fully shown. For all Raman studies was CVD graphene used.*

Instead, the 2D peak is analyzed statistically for CVD graphene and functionalized CVD graphene, respectively. Only the sample with CVD graphene functionalized with organic salt **78** shows a significant shift of the peak position of the 2D peak by 23 cm^{-1} (median value). In the same way, a significant increase in the FWHM Γ_{2D} of the 2D peak is only observed for this sample (broadening by 11 cm^{-1}). The change in position and geometry of the 2D peak corresponds to p-doping of CVD graphene by **78**. Since no p-doping was observed based on the shift and shape of the 2D peak of CVD graphene functionalized with the monocationic organic salts **76** and **75**, it can be speculated that both molecules interact less with graphene, compared with tricationic organic salt **78** or are not bound to the CVD graphene at all. The organic salt **(HexaDiMeBim)$^{6+}$(OTf)$_6$$^{1-}$** showed on both the silica substrate and CVD graphene substrate a high fluorescent background and therefore a further Raman study with the available laser (523 nm) was impossible.

5.2.4 Raman Analysis of Functionalized MoS_2

The doping of monolayer MoS_2 should be reflected in a shift of the $E_{2g}{}^1$ and A_{1g} bands of MoS_2. Recorded spectra for all prepared MoS_2 samples display the $E_{2g}{}^1$ peak at 384.2 cm^{-1} and the A_{1g} band at 404.0 cm^{-1},which is in good agreement with the reported values.[69] The difference in peak position between $E_{2g}{}^1$ and A_{1g} bands is 19.8 cm^{-1} and confirms that the prepared MoS_2 samples consisted of monolayer MoS_2.[69, 92, 248] None of the neutral molecules **HexaPy** (**47**), **HexaBim** (**71**) or **HexaMeBim** (**85**) induced any significant shift of the characteristic $E_{2g}{}^1$ and A_{1g} bands when adsorbed on the MoS_2 monolayers. The C_3 symmetric trication **(TriDiMeBim)$^{3+}$(OTf)$_3$$^{1-}$** (**78**) induces a small shift in the peak position of the A_{1g} band (shift of 1.9 cm^{-1} towards higher wavenumbers) when non-covalently bound to MoS_2 (Figure 26). Similarly, both hexacationic derivatives **(HexaMePy)$^{6+}$(OTf)$_6$$^{1-}$** (**87**) and **(HexaDiMeBim)$^{6+}$(OTf)$_6$$^{1-}$** (**86**) induce small shifts of 1.8 cm^{-1} in the peak position of the A_{1g} band (also towards higher wavenumbers). The non-covalent functionalization of MoS_2 with oleylamine, which is known to n-dope MoS_2,[305] shows a shifting of 3 cm^{-1} of the A_{1g} band towards lower wavenumbers.[306] The treatment of monolayer MoS_2 with oxygen plasma shows due to adsorption of oxygen the p-doping effect to MoS_2. This corresponds to a shifting of the A_{1g} band towards higher wavenumbers.[307] The p-doped MoS_2 samples were further non-covalently functionalized with Rhodamine 6G and also Raman peaks, corresponding to the dye, were observed. The shifting of the A_{1g} band towards higher wavenumbers band in our studies can be therefore also interpreted as p-doping effect to MoS_2. However were no molecular peaks from the molecules itself found in the MoS_2 Raman spectra in contrast to results in the literature.[307]

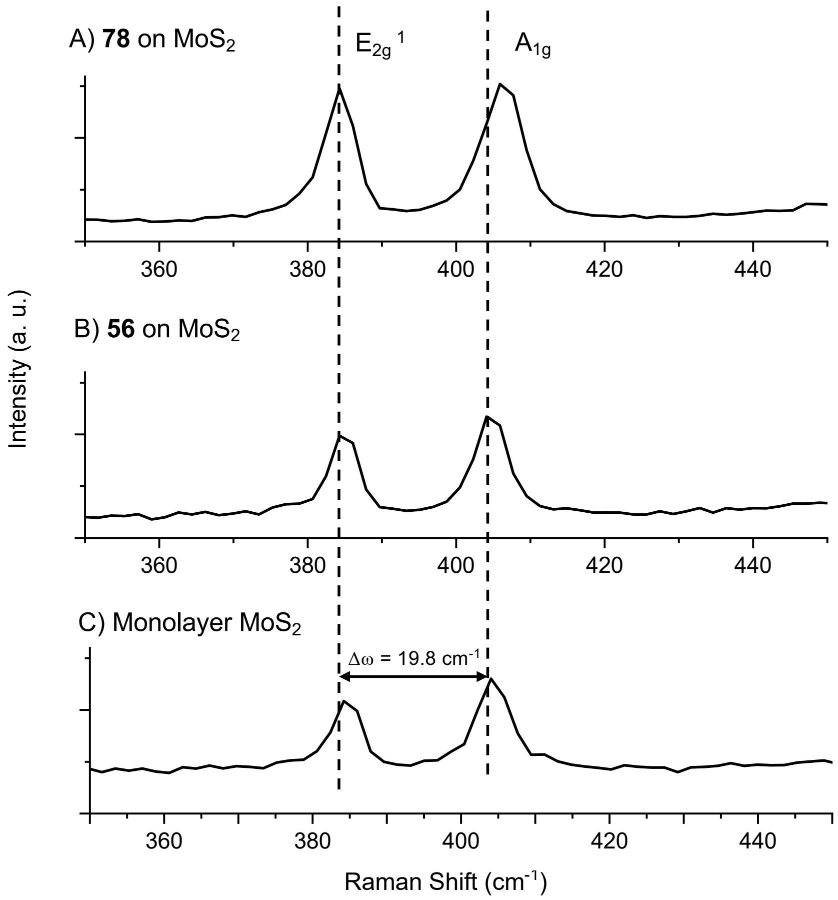

*Figure 26. Raman spectra of A) organic salt **78** on MoS$_2$, B) neutral molecule **56** on MoS$_2$ and monolayer MoS$_2$. The dashed lines represent the Raman peaks positions of the characteristic $E_{2g}{}^1$ and A_{1g} bands from monolayer MoS$_2$ (difference: 19.8 cm^{-1}).*

5.2.5 XPS Analysis of Functionalized Graphene

X-ray photoelectron spectroscopy was used to study the interaction between the adsorbates and graphene, as well as to determine the elemental composition of the surface of the CVD-graphene/hybrid materials.[308] All neutral imidazole systems contain two sets of chemically distinctly different nitrogen atoms, i.e. imine nitrogen atoms ($R_2C{=}NR$) and secondary amine type of nitrogen atoms (R_2-NH). Therefore, these systems are expected to display two N1s signals in the XPS spectra. On the other hand, all nitrogen atoms in the organic salts are chemically equivalent. A single N1s peak corresponding to an imidazolium nitrogen is therefore expected to be found in the XPS spectra of these systems.

The recorded N1s spectra for both the neutral and the charged systems on silica substrate are in line with what is expected for these systems. However, the peak positions corresponding to the two different binding state are different for all molecules. For example, the spectrum of **TriBim** (**56**) exhibits two deconvoluted peaks in a 1:1 area ratio and with the binding energies of 398.6 and 400.7 eV, respectively, while the spectrum of the organic salt **(TriDiMeBim)$^{3+}$(OTf)$_3$$^{1-}$** (**78**) shows one major peak at 402.1 eV. Comparing the nitrogen concentration of all neutral molecules on the CVD graphene substrate, the molecule **56** has a 3-times higher concentration, indicating a stronger binding of **56** to graphene. This is in agreement with the overall planar geometry of **56**, which leads to strong dispersion interactions between **56** and graphene. Even though the larger size of **HexaBim** (**71**), the binding of **71** to graphene is disfavored due to its twisted molecular geometry (Table 2-3). An overview of all N1s spectra recorded for both silica and CVD graphene substrates incubated with the organic salts **(TriMeBim)$^{1+}$(OTf)$^{1-}$**, **(DiMePhBim)$^{1+}$(OTf)$^{1-}$**, **(TriDiMeBim)$^{3+}$(OTf)$_3$$^{1-}$** and **(HexaDiMeBim)$^{6+}(OTf)_6$$^{1-}$** is shown in Figure 27. All four organic salts on silica substrate show one major peak in the N1s signal, which is consistent with the fact that the two imidazolium nitrogen atoms are chemically equivalent.[309] Non-covalently bound to CVD graphene, all organic salts except **(HexaDiMeBim)$^{6+}$(OTf)$_6$$^{1-}$** shows two peaks, with more or less the same signal intensity in the N1s region.

This observation can be explained by a combination of two reasons. Due to the twisted geometry of **(DiMePhBim)$^{1+}$** and **(TriDiMeBim)$^{3+}$**, half of the nitrogen atoms are facing to the surface of graphene, while the other nitrogen atoms are pointing away from graphene. Thus, the two sets of nitrogen atoms sets of nitrogen atoms experience different chemical environments, which results in different binding energies. However, the highly twisted hexacationic molecule **(HexaDiMeBim)$^{6+}$** shows just one peak in the N1s signal. A more reasonable explanation is, that different adsorbates are not equally influenced by their counterions. Computational quantum mechanical modelling shows that the hexacationic system **(HexaDiMeBim)$^{6+}$** can bind six triflate ions **(OTf)$^{1-}$** in its six pincer-like clefts. Upon binding, the anions form tight ion pairs with the benzimidazolium units that constitute the walls of the clefts. Therefore, each three triflate ions tend to lie on the upper side and lower side of the molecule. Together with the six bound triflate ions, **(HexaDiMeBim)$^{6+}$(OTf)$_6$$^{1-}$** forms an uncharged disk-shaped entity (Figure 28) that is more like a large neutral species. The **(HexaDiMeBim)$^{6+}$(OTf)$_6$$^{1-}$** entity would therefore favor to bind non-covalently to graphene *via* London dispersion interactions. That also explains the observation that the N1s signal of **(HexaDiMeBim)$^{6+}$(OTf)$_6$$^{1-}$** on CVD graphene shows a substantially higher nitrogen content compared to the other organic salts on CVD graphene. Thus, graphene shows a higher affinity for this system than any other of the systems studied.

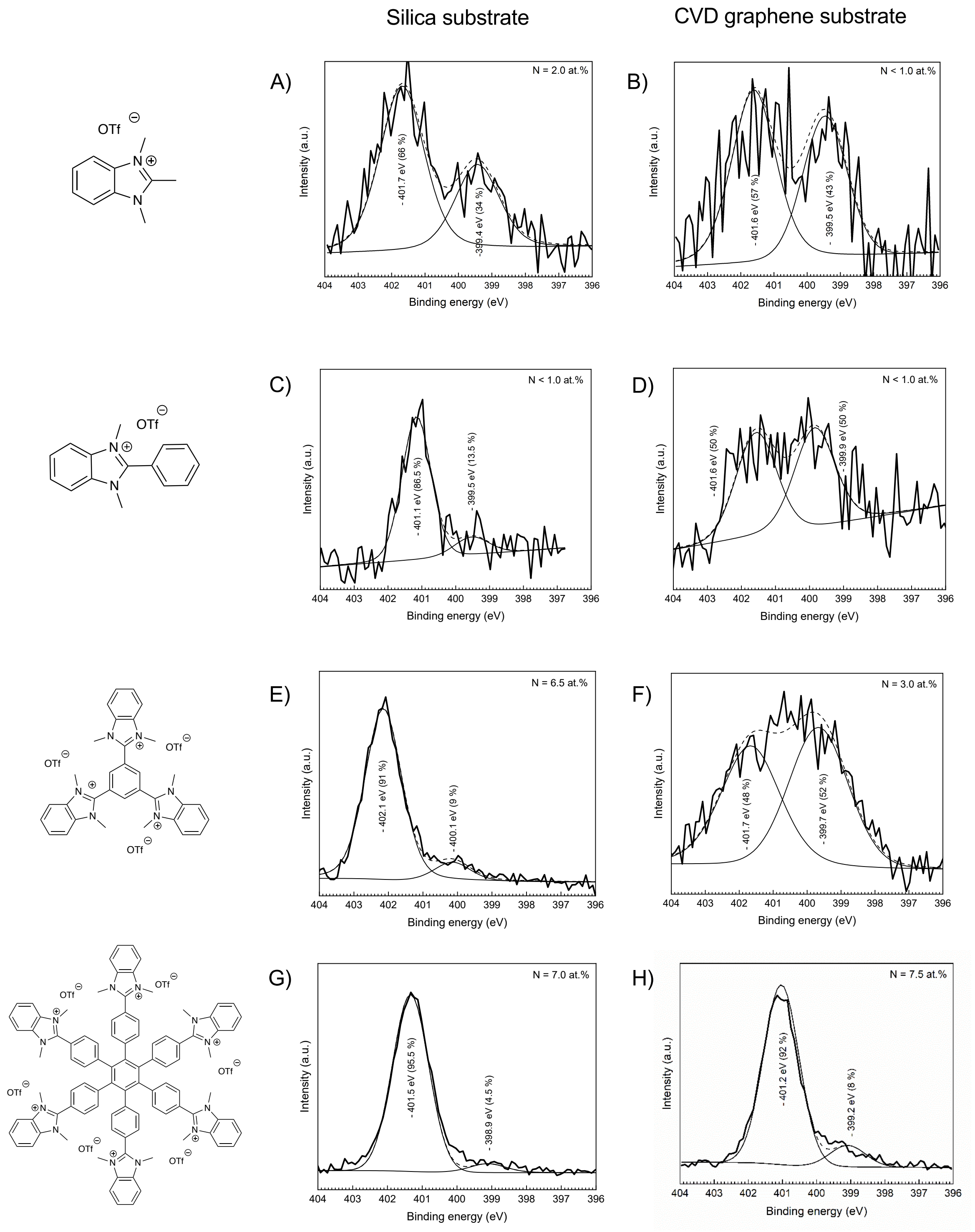

Figure 27. High resolution scan of the N1s region of A) ***(TriMeBim)$^{1+}$(OTf)$^{1-}$*** *(**76**) on silica and B) on CVD graphene; C)* ***(DiMePhBim)$^{1+}$(OTf)$^{1-}$*** *(**75**) on silica and D) on CVD graphene; E)* ***(TriDiMeBim)$^{3+}$(OTf)$_3$$^{1-}$*** *(**78**) on silica and F) on CVD graphene; G)* ***(HexaDiMeBim)$^{6+}$(OTf)$_6$$^{1-}$*** *(**78**) on silica and H) on CVD graphene.*

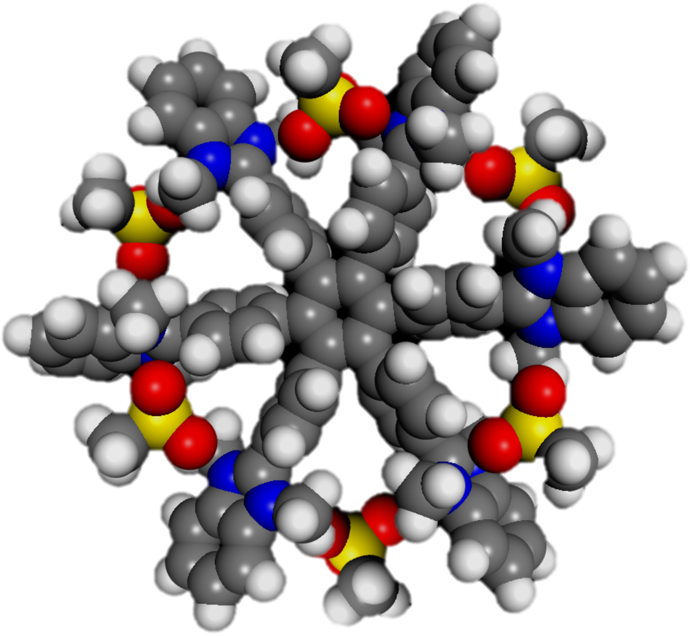

Figure 28. Optimized structure *(PBE*[296]*, GGA functional/ CASTEP basis set within Material Studios framework) of the hexacation (***Hexa*****DiMeBim)**$^{6+}$ *together with six triflate ions.*

As previously mentioned, the elemental composition of surfaces can be analyzed with XPS. The XPS spectra of all organic salts on both substrates were analyzed with respect to the N1s and F1s signals to calculate the ratio between the number of anions and cations on the surfaces. This is possible because nitrogen atoms are only present in the cations of the organic salts and fluorine atoms are only present in the triflate anions. All samples give a peak at 688.4 eV in the F1s, corresponding to an organic fluoride. The ratio between the areas for the nitrogen and fluorine signals (N:F) is in agreement with the molecular formula of the organic salts on silica substrate. Surprisingly, XPS spectra of the monocationic and tricationic organic salts on CVD graphene substrate indicate a lower fluorine content than expected. This observation suggests a loss of some counterions in the process of binding to graphene. The counterions can either be exchanged (ion exchange) during the sample incubation or by a partial charge transfer between graphene and the cations. This will be discussed in chapter 5.2.7. Sulfur is also only present in the anion and an analogous analysis based on this element gives the same result. The XPS spectra of CVD functionalized with **(HexaDiMeBim)**$^{6+}$**(OTf)**$_{6}$$^{1-}$ show no very little loss of triflate anions. This is due to the already discussed tight ion pairing between the hexacation **(HexaDiMeBim)**$^{6+}$ and its counterions.

5.2.6 ToF-SIMS Analysis of Functionalized Graphene

In this thesis time-of-flight secondary ion mass spectrometry (ToF-SIMS) was used to study and confirm the existence of positively charged and negatively charged ions on the surface of non-covalently functionalized graphene surfaces. Samples of r-oxo-G were non-covalently functionalized with the organic salts **(DiMePhBim)$^{1+}$(OTf)$^{1-}$** (**75**), **(TriDiMeBim)$^{3+}$(OTf)$_3$$^{1-}$** (**78**) and **(HexaDiMeBim)$^{6+}$(OTf)$_6$$^{1-}$** (**86**). Previous Raman and XPS studies showed, that the cationic molecules are not interaction with the silica substrate. Using r-oxo-G as substrate we expected to detect the molecular cations and anions just on the surface of the graphene flakes and not on the silica substrate. In agreement, chemical imaging by ToF-SIMS ofSi/SiO$_2$ wafers submersed in methanol solutions of organic salts reveal that the tricationic molecules do not bind to the Si/SiO$_2$ surface. Chemical imaging of r-oxo-G samples functionalized with organic salt **75** shows the presence of the cation and its counterion on flake like areas expected to be found on r-oxo-G samples. The observed areas fit well with the size and shape of flakes of r-oxo-G observed by other techniques, such as optical microscopy. Therefore, we suggest that the observed areas of molecular cation and counter ion mass hits represent the functionalized r-oxo-G flakes on the sample. Using CVD graphene instead of r-oxo-G results in molecular mass hits of both the cation and the anion on the whole surface, which indicates a homogeneous non-covalent functionalization all over the CVD graphene surface. Chemical imaging by ToF-SIMS of samples with the organic salt **78** non-covalently bound to r-oxo-G show similar results. The calculated mass for the C_3 symmetric cation **78**$^{3+}$ is m/z = 513.28 and the calculated mass for the triflate anion is m/z = 148.95. The most prominent signal in positive ion mode was found at m/z = 811.16. This corresponds to the trication **78**$^{3+}$ plus two triflate anions. Also, although with lower signal intensity, signals were observed at m/z = 662.73 and m/z = 513.28 corresponding to the mass of the reduced trication without 2 and 3 counterions, respectively (Figure 29A). Figure 29B shows the chemical images recorded in negative ion mode of r-oxo-G non-covalently functionalized with organic salt **78**. The highest signal intensity of m/z = 148.95 can be assigned to the triflate counterions of the organic triflate salt. In agreement with the studies in positive ion mode, the mass hits corresponding to the triflate counterions are observed as a flake-like pattern. Figure 29C shows the optical image of a silica wafer coated with r-oxo-G flakes with a size of approximately 5 and 20 µm. Also, r-oxo-G samples functionalized with the organic salt **86** were studied with ToF-SIMS. Studies in negative ion mode show the signal for the triflate counter ions at m/z = 148.95 in a flake-like pattern and only mass hits corresponding to the silica substrate is detected around the flake-like pattern. The analysis of the cation **86**$^{6+}$ is however not trivial. ToF-SIMS is a destructive method and lots of fragments are possible. HR-ESI-MS experiments show that the reduced derivatives of **86**$^{6+}$ can be detected. However, none of these mass hits was detected for the cation **86**$^{6+}$ with ToF-SIMS. The most prominent signals are m/z = 126.93, 360.80, 362.80, 596.66 and can be observed in a flake-like pattern in the same way as the triflate counterions. These mass peaks must be related to fragments of **86**$^{6+}$. The structure of these fragments is however not known.

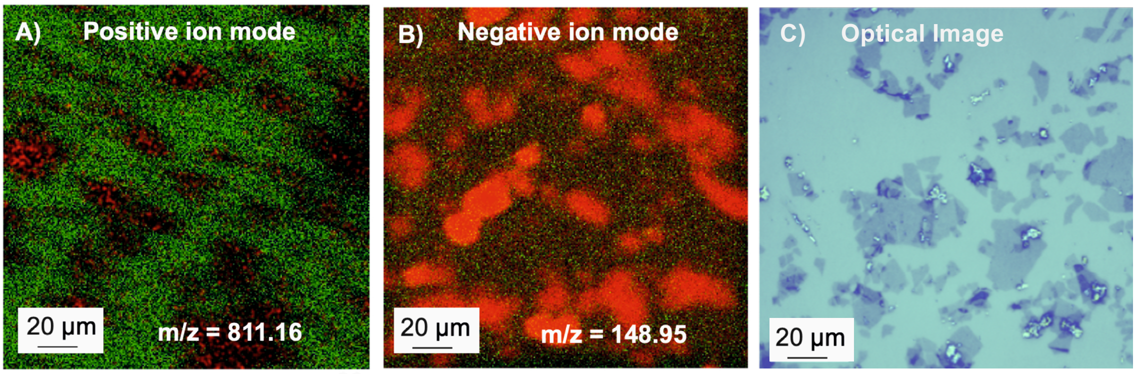

*Figure 29. A) ToF-SIMS imagine in positive ion mode showing the trication **78**$^{3+}$ together with two counterions on reduced oxo-G on silica substrate in flake like pattern. Red: m/z 811.16, green: Si+. B) ToF-SIMS imagine in negative ion mode showing the triflate anion from the organic salt **78** on reduced oxo-G on silica substrate in flake like pattern. Red: m/z 148.95, green: Si-. C) Optical image of r-oxo-G flakes functionalized with organic salt **78**. The flake size varies between 5 and 20 µm.*

5.2.7 Computational Studies of Functionalized Graphene

The XPS analysis of non-covalently functionalized graphene with the organic salts **(TriMeBim)$^{1+}$(OTf)$_1$$^{1-}$** (**76**), **(DiMePhBim)$^{1+}$(OTf)$_1$$^{1-}$** (**75**), **(TriDiMeBim)$^{3+}$(OTf)$_3$$^{1-}$** (**78**) and **(HexaDiMeBim)$^{6+}$(OTf)$_6$$^{1-}$** (**86**) and their uncharged precursor indicated, that a partial charge can be transfered between graphene and the non-covalently bound molecules. To gain more insights about the interaction between graphene and charged molecules, computational quantum mechanical modelling was performed together with Valentina Cantatore. DFT calculations were applied (PBE[296], GGA functional/ CASTEP basis set within Material Studios framework) to study the overall electron distribution in a unit cell tricationic molecule **78**$^{3+}$ on top of a 9 × 9 supercell of graphene.

The optimized structure of **78**$^{3+}$ is as previously discussed in chapter 5.1.5 propeller shaped (Figure 30A). The addition of an electron to the trication **78**$^{3+}$ forms the dication **78**$^{2+}$ with an overall charge of +2. The additional electron causes also a flattening of the molecular geometry as previously discussed from 58° to 50°. On top of graphene, a decrease of the dihedral angle from 58° to 24° was observed (Figure 30B). The overall planar geometry of **78**$^{2+}$ contributed to the strong interactions between **78**$^{2+}$ and graphene.[294] The computational calculations show that approximately half an electron is transferred from graphene to the trication **78**$^{3+}$. Some stabilizing effects can be derived from this partial electron transfer. The increased electron density at the central benzene (LUMO of **78**$^{3+}$, Figure 20) ring decreases the coulombic repulsion between the cationic benzimidazolium moieties. This results in a planarization of dication **78**$^{2+}$. The planar geometry of **78**$^{2+}$ allows a shorter distance between **78**$^{2+}$ and graphene. A further decrease of the overall charge of the unit cell does not show a larger partial electron transfer from graphene to the trication **78**$^{3+}$. The observed charge transfer from graphene to the trication **78**$^{3+}$ explains also the observations in XPS studies of graphene samples that were non-covalently functionalized with the organic salt **(TriDiMeBim)$^{3+}$(OTf)$_3$$^{1-}$** (**78**). The trication **78**$^{3+}$ is surrounded by three counterions in the organic salt unit **(TriDiMeBim)$^{3+}$(OTf)$_3$$^{1-}$** (**78**).

This corresponds to an elemental ratio of nitrogen atoms and fluorine atoms of 1:3, which was found for the organic salt **78** on silica substrate. The trication non-covalently bound to graphene is getting partially reduced by the charge transfer. This leads to a more delocalized positive charge. As a consequence, the positive charge density decreases as well as the Coulomb interactions between the trication **78**$^{3+}$ and its anions decreases. Some counterions become therefore superfluous and are rinsed off during the sample preparation. This could be the reason why less counterions are observed in non-covalent functionalized graphene (lower elemental ratio between nitrogen and fluorine atoms) compared with samples of the cationic molecules on silica substrate.

A) **(TriDiMeBim)**$^{3+}$ in vacuo

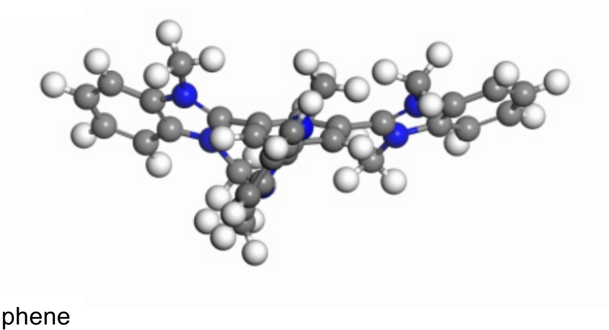

B) **(TriDiMeBim)**$^{2+}$ on graphene

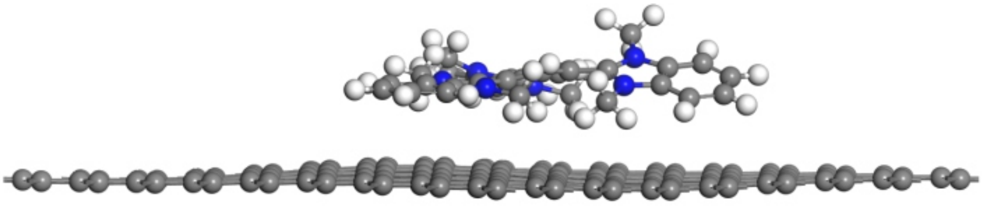

Figure 30. Optimized geometry (PBE[296], GGA functional/ CASTEP basis set within Material Studios framework) of A) tricationic molecule ***(TriDiMeBim)***$^{3+}$*(78*$^{3+}$*) in vacuo and B)* ***(TriDiMeBim)***$^{2+}$*(78*$^{2+}$*) non-covalently bound to graphene.*[294]

5.2.8 Applications of Functionalized Graphene

Previous characterizations with non-covalent functionalized graphene showed a p-doping effect of the cationic π-conjugated molecules on graphene. The organic salt **(TriDiMeBim)$^{3+}$(OTf)$_3^{-1}$**(**78**) and the neutral molecule **TriBim** (**56**) were used to fabricate together field-effect transistor device (FET) from with r-oxo-G as part of a cooperation with Zhenping Wang (Figure 31). Transfer curves (I_{ds}–V_{ds}) with unipolar character for FET device before and after non-covalent modification with **78** are shown in Figure 30. A hysteresis effect of the monolayer r-oxo-G on SiO_2 is observed after sweeping continuously from -50 to 50 V and then back to -50 V. Therefore, each two carrier mobilities for r-oxo-G and the functionalized r-oxo-G/**78** were calculated. The carrier mobilities were based on the minimum (blue dash lines) and the maximum slopes (green dash lines) of both curves. For the r-oxo-G, the fluctuation of its carrier mobilities is between 26.4 and 28.6 cm^2 V^{-1} s^{-1}. After functionalization with the organic salt **78**, the carrier mobilities of r-oxo-G/**78** are between 17.8 and 20.7 cm^2 V^{-1} s^{-1}. This shows that the effect of the hysteresis on carrier mobilities is less than the effect of non-covalently functionalization of r-oxo-G.

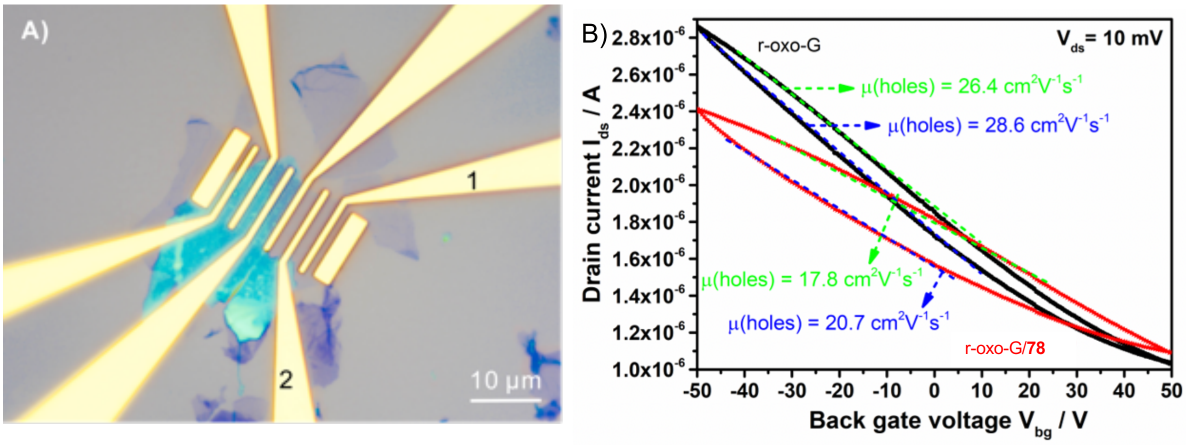

*Figure 31. Transport measurements of monolayer r-oxo-G-based FET. A) Optical image of the fabricated graphene device. A channel width of 20 µm and length of 3 µm between electrode 1 and 2. B) Comparison of each two carrier mobilities at the maximum (green dash lines) and minimum slopes (blue dash lines) for r-oxo-G (black) and r-oxo-G/**78**(red). V_{ds} = 10 mV.*[294] *Reprinted with permission.*

After doping r-oxo-G with organic salt **78** I_{ds}–V_{ds} curves still keep the unipolar character, but these curves lean to a higher p-doped direction. Reference experiments showed that neutral molecule **56** non-covalently bound to r-oxo-G also results in p-doping of the underlying graphene. However, the effect is weaker compared with the organic salt **78** on graphene. These results do not tell us which molecule interacts stronger with graphene in comparison, however the cationic nature of organic salt **78** together with the already discussed charge transfer from graphene to the cationic molecule is responsible for a stronger change in the charge density of graphene, which results in a stronger p-doping of graphene. Also, the reduction potential of the organic salt **78** is higher (-1.70 V) compared to neutral molecule **56** (-2.45 V). A charge transfer is therefore more likely between graphene and the cation of the organic salt **78**.

5.2.9 Photoluminescence Studies of Functionalized MoS_2

To study the influence of cationic π-conjugated molecules on monolayer MoS_2, the intensity of mechanically exfoliated MoS_2 was measured before and after non-covalent functionalization with the organic salts **(TriDiMeBim)$^{3+}$(OTf)$_3^{-1}$** (**78**), **(HexaDiMeBim)$^{6+}$(OTf)$_6^{-1}$** (**86**) and **(HexaMePy)$^{6+}$(OTf)$_6^{-1}$** (**87**), and their neutral precursors **TriBim** (**56**), **HexaBim** (**71**), **HexaMeBim** (**85**) and **HexaPy** (**47**). As already discussed in previous chapters, the trication molecule **78^{3+}** of the organic salt **78** caused a p-doping on graphene. The non-covalently functionalization of monolayer MoS_2 with the organic salt **78** caused a photoluminescence (PL) intensity enhancement by 475%, which corresponds to a p-doping of monolayer MoS_2.[92] Interestingly, already the neutral C_3 symmetric molecule **56** caused a photoluminescence (PL) intensity enhancement of monolayer MoS_2 by 250%. The lower PL intensity enhancement of functionalized MoS_2 with molecule **56** compared to the organic salt **78** can be explained by a lower p-doping character of the neutral molecule **56**. However was also a slight red-shift of the PL peak observed (Figure 32A), which corresponds to a n-doping of MoS_2.[310] The non-covalently functionalization of monolayer MoS_2 with the neutral C_6 symmetric polypyridine molecule **47** and the organic salt **87** showed a similar trend. Already the neutral molecule **47** caused a strong PL intensity enhancement of the MoS_2 by 560%. However the binding of the organic salt **87** to MoS_2 showed an even stronger PL intensity enhancement by 1140% (Figure 32B). It is therefore in the series of tested molecules the strongest p-dopant. No significant PL intensity maximum shifting was observed.

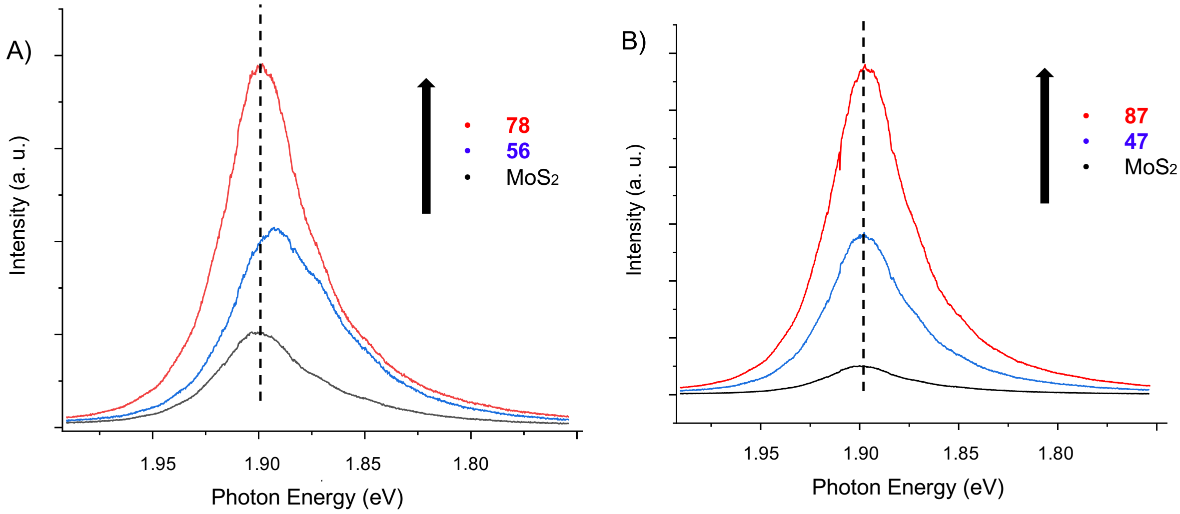

Figure 32. PL spectra of chemical functionalized MoS_2. A) Normalized PL spectra of MoS_2 (black color), with neutral ***TriBim (56)*** *functionalized MoS_2 (blue color) and with* ***(TriDiMeBim)$^{3+}$(OTf)$_3^{1-}$ (78)*** *functionalized MoS_2 (red color). B) Normalized PL spectra of MoS_2 (black color), with neutral* ***HexaPy (47)*** *functionalized MoS_2 (blue color) and with* ***(HexaMePy)$^{6+}$(OTf)$_6^{1-}$ (87)*** *functionalized MoS_2 (red color). No significant peak shifting is observed. The dashed line shows the position of the peak energy of the PL spectrum of MoS_2.*

The polybenzimidazole derivatives **71**, **85** and the organic salt **86** however displayed a different behavior, when non-covalently bound to MoS_2. The neutral C_6 symmetric molecule **71** was the only molecule in this series, which increased the PL intensity of MoS_2 by 130%. This was much lower than the other already discussed neutral molecules **47** and **56**. The neutral molecule **85** non-covalently bound to MoS_2 showed an decrease of the PL intensity (33% quenched). Surprisingly, binding the organic salt **86** non-covalently to MoS_2, a very strong quenching of the PL intensity (91% quenched) was observed. The PL intensity decrease for MoS_2 functionalized with **85** and **86** corresponds to a n-doping of MoS_2.[310] The red shifting of the PL intensity maxima for the MoS_2/**86** sample supports this assumption. The lower HOMO energy level of **86**$^{6+}$ (-15.3 eV) compared with the HOMO energy level of the tricationic molecule **78**$^{3+}$ (-13.4 eV) would suggest a p-doping of MoS_2 in the same way it was observed for MoS_2 samples, which were functionalized with the organic salt **78**. This assumption however does not take the counterions of **86** into account. And as previously discussed binds the hexacation **86**$^{6+}$ its counterions tight to form a large neutral species (Figure 28). The counterions of this disk-shaped entity shield the hexacation **86**$^{6+}$ and therefore, no p-doping of MoS_2 is observed. Computational studies show, that the other organic salts **78** and **87** are not as tight shielded by their counterions. Therefore is the p-doping character of the cations **78**$^{3+}$ and **87**$^{6+}$ not weakened to the same extent.

6. Conclusion and Outlook

Aim 1: Synthesis and characterization of a series of cationic π-conjugated systems (monocationic, trication and hexacationic) with different counterions.

Herein, the synthesis of a series of benzimidazole and pyridine derived π-conjugated systems of different sizes and with different amount of charges was shown. Benzimidazole derivatives with three benzimidazole moieties could be reacted in a microwave reactor according to a customized protocol. For the synthesis of π-conjugated systems with six benzimidazole moieties was the development of a different protocol necessary. Both benzimidazole and pyridine derived π-conjugated systems were alkylated to form monocationic, trication and hexacationic π-conjugated systems. The variation of the alkylation agent in the *N*-alkylation reaction did not have a significant overall change of the product yield, but had an impact on the solubility of the final compound. The molecules were purified and characterized. The photophysical and electrochemical properties of selected were studied and got support from computational studies of the same π-conjugated systems.

Aim 2: Develop a method to non-covalently functionalize graphene and MoS_2 non-covalently with cationic π-conjugated systems and their uncharged precursors.

A developed protocol was successfully used to non-covalently functionalize different types of graphene with both neutral and charged π-conjugated systems. The graphene samples were incubated in a methanolic solution of the respective molecule and subsequently rinsed with methanol to remove an excess of the molecules. The same protocol was not successful for the functionalization of MoS_2. A more advanced protocol was applied to non-covalently functionalize MoS_2. The MoS_2 samples were drop-casted with a methanolic solution of the respective molecule and the excess of solvent was removed from the sample surface.

Aim 3: Find analytical tools to characterize and study the non-covalent interactions between cationic π-conjugated systems and graphene (and MoS_2).

The successfully functionalized graphene and MoS_2 samples were characterized with different spectroscopic methods to obtain an overall picture of the functionalized materials. The combination of AFM spectroscopy, Raman spectroscopy and ToF-SIMS showed exclusively an overall homogeneous functionalization of the graphene surface with the π-conjugated systems. The doping effect on graphene was studied with XPS and computational analyses. A charge transfer from graphene to the tricationic molecule **(TriDiMeBim)**$^{3+}$ leads to a p-doping of graphene, when non-covalently functionalized with the organic salt **(TriDiMeBim)**$^{3+}$**(OTf)**$_3{}^{1-}$. The neutral molecules showed a weaker p-doping effect on graphene compared with the organic salts. The fabrication of a FET device confirmed the p-doping effect of both the neutral molecule **TriBim** and the organic salt **(TriDiMeBim)$^{3+}$(OTf)$_3$$^{1-}$**. Also photoluminescence studies of non-covalently functionalized MoS_2 showed that both the neutral molecule **TriBim** and the organic salt **(TriDiMeBim)$^{3+}$(OTf)$_3$$^{1-}$** have a p-doping effect on MoS_2. The tested hexacationic organic salts **(HexaMePy)$^{6+}$(OTf)$_6$$^{1-}$** and **(HexaDiMeBim)$^{6+}(OTf)_6$$^{1-}$** could either p or n-dope MoS_2.

Aim 4: Study the binding affinities between the π-conjugated systems and graphene.

Lastly, different structural parameter as well es different counter ions from the cationic π-conjugated molecules were studied on the binding affinity to graphene. In the series of neutral molecules, the flat C_3 symmetric molecule **TriBim** has the highest affinity. Due to a short binding distance, London dispersion interactions are favored. The even larger C_6 symmetric molecule **HexaBim** has a weaker interaction with graphene due to the longer binding distance enforced by its twisted geometry. Of the tested organic salts, the highest binding affinity to graphene was found for the hexacationic salt **(HexaDiMeBim)$^{6+}$(OTf)$_6$$^{1-}$**. In this organic salt, the hexacation **(HexaDiMeBim)$^{6+}$** forms a uncharged disk-shaped entity with its tightly bound counterions. Even though the high charge of the hexacation, the interaction with graphene is controlled by London dispersion interactions.

In summary it could be shown that the binding affinity of neutral and charged molecules is not favored by the amount of positive charges on the adsorbate, nor is it only dependent on the size of the π-conjugated system of the adsorbate molecules. However the geometry of the adsorbates plays a much more important role together with the binding strength between the cationic molecules and its counterions. A proper design of the organic cations can prevent the cations from losing their counterions and has therefore an influence on the doping of non-covalently functionalized graphene and MoS_2.

This thesis highlights that the process of non-covalent functionalization of 2D materials like graphene and MoS_2 is a promising field of research for the development of new 2D hybrid materials. This research field is young and needs to be explored more in depth and opens the door for many exciting research projects or developments. Planar HBC derivatives might lead to a very strong binding affinity to the surface of π-conjugated systems like graphene and would therefore be able to introduce either a strong p- or n-doping of graphene. The challenging part however remains the synthesis and purification of these organic molecules.

7. Acknowledgement

This thesis would have been not possible without the help and support from numerous people. The research presented in this thesis was founded by Chalmersska forskningsfonden. I also want to thank stiftelsen Lillemor Kündig and stiftelsen Åforsk for their support to attend conferences. I would also like to thank JSPS and STINT for their scholarship for my research exchange in Japan.

I first of all I want to thank my supervisor **Jerker Mårtensson** for taking me as a PhD student and believing in me. Your expertise, guidance, patience and willing to explore together new fields of research helped me to grow as a researcher. Thank you for the long and productive discussions we had.

I also want to thank my second supervisor **Siegfried Eigler** for his project ideas, support and discussions about results as well as chemical reactions, that did not want to work.

Nina Kann, thank you for your support. The chats with you about chemistry but also gardening always created a very friendly atmosphere. Thank you to **Itai Panas** and **Elisabet Ahlberg** for your support in our projects and our fruitful discussions.

Valentina Cantatore, thank you for being such a good co-worker and friend. I appreciated a lot your guidance regarding theoretical chemistry. Mille grazie.

I want to thank **Eric Tam** for his help with the XPS analysis and **Per Malmberg** for his help with the ToF-SIMS analysis. Thank you to **Ibrahim Kaya**, **Françoise M. Amombo Noa** and **Lars Öhrström** for our project discussions and successful collaborations.

Hideki Yorimitsu and **Atsushi Kaga**, thank you for your guidance during my time in Japan.
ありがとうございました

For proofreading and improving this thesis I would like to thank my college **Savannah Zacharias**.

I also would like to thank all former and present colleagues from the 5th and 9th floor for the shared moments during fika breaks, lunch or after works.

আমাদের মধ্যাহ্নভোজ মিটিং, রসায়ন, জীবন এবং অবশ্যই কালী সম্পর্কে আলোচনার জন্য তোমাদের অনেক ধন্যবাদ **নাজমুন** এবং দেবায়ণী।

I also want to thank the other professors from the division chemistry and biochemistry for their support during the teaching courses, PhD courses and seminars. I also would like to thank Gunilla, Lotta, Lynga and Sara for always being helpful and friendly.
I also want to thank my co-worker and colleagues Christian, Philipp, Zhenping and Qing from the Freie University for their support in experiments and our scientific discussions. Thank you to the rest of the Eigler group in Berlin.

I want to thank all people I met in Sweden, who turned out to be very good friends to me now.

Grazie al mio coinquilino e amico Giulio. Grazie per il support nelle situazioni difficili e per i buoni consigli, per motivarmi e ovviamente per il buon cibo.

Zum Schluss möchte ich von ganzem Herzen meinen Eltern Alexander und Karin, sowie meinen Schwestern Annika und Svenja danken, die immer für mich da sind und mich jederzeit unterstützt, gefördert und motiviert haben. Ich liebe euch. Tack hjärtat att du finns.

8. References

[1] M. Garcia-Hernandez, J. Coleman, *2D Mater.* **2016**, *3.1*, 019501.

[2] K. S. Novoselov, D. Jiang, F. Schedin, T. J. Booth, V. V. Khotkevich, S. V. Morozov, A. K. Geim, *Proc. Natl. Acad. Sci. U.S.A.* **2005**, *102*, 10451-10453.

[3] K. S. Novoselov, A. K. Geim, S. Morozov, D. Jiang, M. I. Katsnelson, I. Grigorieva, S. Dubonos, Firsov, AA, *Nature* **2005**, *438*, 197-200.

[4] H. P. Boehm, *Angew. Chem. Int. Ed.* **2010**, *49*, 9332-9335.

[5] D. R. Dreyer, R. S. Ruoff, C. W. Bielawski, *Angew. Chem. Int. Ed.* **2010**, *49*, 9336-9344.

[6] K. S. Novoselov, A. K. Geim, S. V. Morozov, D. Jiang, Y. Zhang, S. V. Dubonos, I. V. Grigorieva, A. A. Firsov, *Science* **2004**, *306*, 666-669.

[7] A. K. Geim, *Rev. Mod. Phys.* **2011**, *83*, 851.

[8] K. Novoselov, *Rev. Mod. Phys.* **2011**, *83*, 837.

[9] C. Lee, X. D. Wei, J. W. Kysar, J. Hone, *Science* **2008**, *321*, 385-388.

[10] I. Meric, M. Y. Han, A. F. Young, B. Ozyilmaz, P. Kim, K. L. Shepard, *Nat Nanotechnol.* **2008**, *3*, 654-659.

[11] A. A. Balandin, S. Ghosh, W. Bao, I. Calizo, D. Teweldebrhan, F. Miao, C. N. Lau, *Nano lett.* **2008**, *8*, 902-907.

[12] J. S. Bunch, S. S. Verbridge, J. S. Alden, A. M. Van Der Zande, J. M. Parpia, H. G. Craighead, P. L. McEuen, *Nano lett.* **2008**, *8*, 2458-2462.

[13] R. R. Nair, P. Blake, A. N. Grigorenko, K. S. Novoselov, T. J. Booth, T. Stauber, N. M. Peres, A. K. Geim, *Science* **2008**, *320*, 1308-1308.

[14] M. I. Katsnelson, *Graphene: carbon in two dimensions*, Cambridge university press, **2012**.

[15] D. D. L. Chung, *J. Mater. Sci* **2002**, *37*, 1475-1489.

[16] S. F. Acquah, A. V. Penkova, D. A. Markelov, A. S. Semisalova, B. E. Leonhardt, J. M. Magi, *ECS J. Solid State Sci. Technol* **2017**, *6*, M3155-M3162.

[17] C. Gao, Z. Guo, J.-H. Liu, X.-J. Huang, *Nanoscale* **2012**, *4*, 1948-1963.

[18] K. Subrahmanyam, S. Vivekchand, A. Govindaraj, C. Rao, *J. Mater. Chem.* **2008**, *18*, 1517-1523.

[19] C. e. N. e. R. Rao, A. e. K. Sood, K. e. S. Subrahmanyam, A. Govindaraj, *Angew. Chem. Int. Ed.* **2009**, *48*, 7752-7777.

[20] A. Ghosh, K. Subrahmanyam, K. S. Krishna, S. Datta, A. Govindaraj, S. K. Pati, C. Rao, *J. Phys. Chem. C* **2008**, *112*, 15704-15707.

[21] J. C. Meyer, A. K. Geim, M. I. Katsnelson, K. S. Novoselov, T. J. Booth, S. Roth, *Nature* **2007**, *446*, 60-63.

[22] A. K. Geim, K. S. Novoselov, in *Nanoscience and technology: a collection of reviews from nature journals*, World Scientific, **2010**, pp. 11-19.

[23] D. Neumaier, H. Zirath, *2D Mater.* **2015**, *2*.

[24] J. Bae, O. Seok Kwon, C.-S. Lee, *Recent pat. nanotech.* **2017**, *11*, 93-100.

[25] Y. H. Xu, J. Q. Liu, *Small* **2016**, *12*, 1400-1419.

[26] D. Chen, H. B. Feng, J. H. Li, *Chem. Rev.* **2012**, *112*, 6027-6053.

[27] Z. G. Zhu, L. Garcia-Gancedo, A. J. Flewitt, H. Q. Xie, F. Moussy, W. I. Milne, *Sensors* **2012**, *12*, 5996-6022.

[28] S. Wu, Q. He, C. Tan, Y. Wang, H. Zhang, *Small* **2013**, *9*, 1160-1172.

[29] F. Schedin, A. K. Geim, S. V. Morozov, E. W. Hill, P. Blake, M. I. Katsnelson, K. S. Novoselov, *Nat. Mater.* **2007**, *6*, 652-655.

[30] S. H. Hur, J. N. Park, *Asia-Pac. J. Chem. Eng.* **2013**, *8*, 218-233.

[31] B. Luo, S. M. Liu, L. J. Zhi, *Small* **2012**, *8*, 630-646.

[32] S. K. Hau, Y.-J. Cheng, H.-L. Yip, Y. Zhang, H. Ma, A. K.-Y. Jen, *ACS Appl. Mater. Interfaces* **2010**, *2*, 1892-1902.

[33] T. Spencer, B. Yoo, K. Kirshenbaum, *J. Chem. Educ.* **2006**, *83*, 1218.

[34] B. T. Marković, V. Jokanović, S. Jovanović, D. Kleut, M. Dramićanin, Z. Marković, *Appl. Surf. Sci.* **2009**, *255*, 7537-7541.

[35] R. M. Girón, J. Marco-Martínez, S. Bellani, A. Insuasty, H. C. Rojas, G. Tullii, M. R. Antognazza, S. Filippone, N. Martín, *J. Mater. Chem. A* **2016**, *4*, 14284-14290.

[36] V. N. Khabashesku, M. X. Pulikkathara, *Mendeleev Commun.* **2006**, *16*, 61-66.

[37] N. Karousis, N. Tagmatarchis, D. Tasis, *Chem. Rev.* **2010**, *110*, 5366-5397.

[38] Y. Li, L. a. Fernandez-Recio, P. Gerstel, V. Srot, P. A. v. Aken, G. Kaiser, M. Burghard, J. Bill, *Chem. Mater.* **2008**, *20*, 5593-5599.

[39] S. P. Lonkar, Y. S. Deshmukh, A. A. Abdala, *Nano Res.* **2015**, *8*, 1039-1074.

[40] J. Q. Liu, J. G. Tang, J. J. Gooding, *J. Mater. Chem.* **2012**, *22*, 12435-12452.

[41] Y.-H. Hwang, S. M. Lee, Y. J. Kim, Y. H. Kahng, K. Lee, *Carbon* **2016**, *100*, 7-15.

[42] M. Cardinali, L. Valentini, J. M. Kenny, *J. Phys. Chem. C* **2011**, *115*, 16652-16656.

[43] G. Eda, G. Fanchini, M. Chhowalla, *Nat. Nanotechnol.* **2008**, *3*, 270-274.

[44] F. Liu, J. Y. Choi, T. S. Seo, *Chem. Commun.* **2010**, *46*, 2844-2846.

[45] D.-W. Lee, T. Kim, M. Lee, *Chem. Commun.* **2011**, *47*, 8259-8261.

[46] J. Liu, L. Tao, W. Yang, D. Li, C. Boyer, R. Wuhrer, F. Braet, T. P. Davis, *Langmuir* **2010**, *26*, 10068-10075.

[47] J. Liu, W. Yang, L. Tao, D. Li, C. Boyer, T. P. Davis, *J. Polym. Sci. Pol. Chem.* **2010**, *48*, 425-433.

[48] H. Kim, S. Kobayashi, M. A. AbdurRahim, M. J. Zhang, A. Khusainova, M. A. Hillmyer, A. A. Abdala, C. W. Macosko, *Polym.* **2011**, *52*, 1837-1846.

[59] J. R. Lomeda, C. D. Doyle, D. V. Kosynkin, W.-F. Hwang, J. M. Tour, *J. Am. Chem. Soc.* **2008**, *130*, 16201-16206.

[50] A. Yoshikawa, H. Matsunami, Y. Nanishi, in *Wide Bandgap Semiconductors*, Springer, **2007**, pp. 1-24.

[51] G. Gui, J. Li, J. Zhong, *Phys. Rev. B* **2008**, *78*, 075435.

[52] B. Guo, L. Fang, B. Zhang, J. R. Gong, *Insciences J.* **2011**, *1*, 80-89.

[53] L. Mohapatra, K. Parida, *J. Mater. Chem. A* **2016**, *4*, 10744-10766.

[54] Y. Venkata Subbaiah, K. Saji, A. Tiwari, *Adv. Funct. Mater.* **2016**, *26*, 2046-2069.

[55] Y. Zhao, Y. Chen, Y.-H. Zhang, S.-F. Liu, *Mater. Chem. Phys.* **2017**, *189*, 215-229.

[56] M. Pumera, Z. Sofer, *Adv. Mater.* **2017**, *29*, 1605299.

[57] J.-W. Jiang, *Front. Phys.* **2015**, *10*, 287-302.

[58] S. Manzeli, D. Ovchinnikov, D. Pasquier, O. V. Yazyev, A. Kis, *Nat. Rev. Mater.* **2017**, *2*, 17033.

[59] M. Chhowalla, H. S. Shin, G. Eda, L.-J. Li, K. P. Loh, H. Zhang, *Nat. Chem.* **2013**, *5*, 263.

[60] B. Radisavljevic, A. Radenovic, J. Brivio, V. Giacometti, A. Kis, *Nat. Nanotechnol.* **2011**, *6*, 147.

[61] Y. Epshteyn, T. J. Risdon, in *12th Lubricating Grease Conference, Goa, India, Jan*, **2010**, pp. 28-30.

[62] R. Chen, T. Zhao, W. Wu, F. Wu, L. Li, J. Qian, R. Xu, H. Wu, H. M. Albishri, A. Al-Bogami, *Nano lett.* **2014**, *14*, 5899-5904.

[63] J. Luxa, V. Mazánek, D. Bouša, D. Sedmidubský, M. Pumera, Z. Sofer, *ChemElectroChem* **2016**, *3*, 565-571.

[64] J. I. Kim, B. S. Lee, C. Chun, J.-K. Cho, S.-Y. Kim, S.-C. Song, *Biomater.* **2012**, *33*, 2251-2259.

[65] S. Alkis, T. Öztaş, L. Aygün, F. Bozkurt, A. Okyay, B. Ortaç, *Opt. express* **2012**, *20*, 21815-21820.
[66] Z. He, W. Que, *Appl. Mater. Today* **2016**, *3*, 23-56.
[67] A. L. Elías, N. Perea-López, A. Castro-Beltrán, A. Berkdemir, R. Lv, S. Feng, A. D. Long, T. Hayashi, Y. A. Kim, M. Endo, *ACS Nano* **2013**, *7*, 5235-5242.
[68] K. Chang, M. Li, T. Wang, S. Ouyang, P. Li, L. Liu, J. Ye, *Adv. Energy Mater.* **2015**, *5*, 1402279.
[69] C. Lee, H. Yan, L. E. Brus, T. F. Heinz, J. Hone, S. Ryu, *ACS Nano* **2010**, *4*, 2695-2700.
[70] G. Yue, J.-Y. Lin, S.-Y. Tai, Y. Xiao, J. Wu, *Electrochim. Acta* **2012**, *85*, 162-168.
[71] M. Tsai, S. Su, J. Chang, D. Tsai, C. Chen, C. Wu, L. Li, L. Chen, J. He, *Lin, J. Wang, ZG Zhang, H. Bai, Y. Li, D. Zhu, X. Zhan, Adv. Mater.* **2015**, *27*, 1170-1174.
[72] G. Razzini, M. Lazzari, L. P. Bicelli, *J. Power Sources* **1981**, *6*, 371.
[73] X. Gu, W. Cui, H. Li, Z. Wu, Z. Zeng, S. T. Lee, H. Zhang, B. Sun, *Adv. Energy Mater.* **2013**, *3*, 1262-1268.
[74] E. Gourmelon, O. Lignier, H. Hadouda, G. Couturier, J. Bernède, J. Tedd, J. Pouzet, J. Salardenne, *Sol. Energy Mater. Sol.* **1997**, *46*, 115-121.
[75] S.-Y. Tai, C.-J. Liu, S.-W. Chou, F. S.-S. Chien, J.-Y. Lin, T.-W. Lin, *J. Mater. Chem.* **2012**, *22*, 24753-24759.
[76] T. Wang, R. Zhu, J. Zhuo, Z. Zhu, Y. Shao, M. Li, *Anal. Chem.* **2014**, *86*, 12064-12069.
[77] P. T. K. Loan, W. Zhang, C. T. Lin, K. H. Wei, L. J. Li, C. H. Chen, *Adv. Mater.* **2014**, *26*, 4838-4844.
[78] R. Bissessur, J. L. Schindler, C. R. Kannewurf, M. Kanatzidis, Molecular Crystals and Liquid Crystals Science and Technology. Section A. Molecular Crystals and Liquid Crystals **1994**, 245, 249-254.
[79] A. B. Farimani, K. Min, N. R. Aluru, *ACS Nano* **2014**, *8*, 7914-7922.
[80] T. Wang, H. Zhu, J. Zhuo, Z. Zhu, P. Papakonstantinou, G. Lubarsky, J. Lin, M. Li, *Anal. Chem.* **2013**, *85*, 10289-10295.
[81] R.-M. Kong, L. Ding, Z. Wang, J. You, F. Qu, *Anal. Bioanal. Chem.* **2015**, *407*, 369-377.
[82] X. Wang, F. Nan, J. Zhao, T. Yang, T. Ge, K. Jiao, *Biosens. Bioelectron.* **2015**, *64*, 386-391.
[83] B. K. Miremadi, R. C. Singh, S. R. Morrison, K. Colbow, *Appl. Phys. A* **1996**, *63*, 271-275.
[84] J.-S. Kim, H.-W. Yoo, H. O. Choi, H.-T. Jung, *Nano lett.* **2014**, *14*, 5941-5947.
[85] J. Huang, Y. He, J. Jin, Y. Li, Z. Dong, R. Li, *Electrochim. Acta* **2014**, *136*, 41-46.
[86] Q. Feng, K. Duan, X. Ye, D. Lu, Y. Du, C. Wang, *Sens. Actuat. B-Chem.* **2014**, *192*, 1-8.
[87] S. Eigler, *Chem. Eur. J.* **2016**, *22*, 7012-7027.
[88] S. Kobayashi, K. Müllen, Encyclopedia of Polymeric Nanomaterials-With 2021 Figures and 146 Tables, Springer, **2015**.
[89] L. Xu, L. Zhao, Y. Wang, M. Zou, Q. Zhang, A. Cao, *Nano Res.* **2019**, *12*, 1619-1624.
[90] L. Sun, X. Zhang, F. Liu, Y. Shen, X. Fan, S. Zheng, J. T. Thong, Z. Liu, S. A. Yang, H. Y. Yang, *Sci. Rep.* **2017**, *7*, 1-9.
[91] S. Presolski, M. Pumera, *Mater. Today* **2016**, *19*, 140-145.
[92] S. Mouri, Y. Miyauchi, K. Matsuda, *Nano lett.* **2013**, *13*, 5944-5948.
[93] W. Tu, J. Lei, S. Zhang, H. Ju, *Chem. Eur. J.* **2010**, *16*, 10771-10777.

[94] Y. Jiang, X. Zhang, C. Shan, S. Hua, Q. Zhang, X. Bai, L. Dan, L. Niu, *Talanta* **2011**, *85*, 76-81.

[95] H. R. Matte, K. Subrahmanyam, K. V. Rao, S. J. George, C. Rao, *Chem. Phys. Lett.* **2011**, *506*, 260-264.

[96] Q. Chen, W. Wei, J.-M. Lin, *Biosens. Bioelectron.* **2011**, *26*, 4497-4502.

[97] H. Chang, Z. Sun, K. Y.-F. Ho, X. Tao, F. Yan, W.-M. Kwok, Z. Zheng, *Nanoscale* **2011**, *3*, 258-264.

[98] K. Lee, R. Gatensby, N. McEvoy, T. Hallam, G. S. Duesberg, *Adv. Mater.* **2013**, *25*, 6699-6702.

[99] Y. Sun, L. Xu, G. I. Waterhouse, M. Wang, X. Qiao, Z. Xu, *Sens. Actuat. B-Chem.* **2019**, *281*, 107-114.

[100] D. Zhang, J. Qian, Y. Yi, O. J. Kingsford, G. Zhu, *J. Electroanal. Chem.* **2019**, *847*, 113229.

[101] A. Sinha, B. Tan, Y. Huang, H. Zhao, X. Dang, J. Chen, R. Jain, TRAC- *Trend Anal. Chem.* **2018**, *102*, 75-90.

[102] Y. Cai, H. Zhou, G. Zhang, Y.-W. Zhang, *Chem. Mater.* **2016**, *28*, 8611-8621.

[103] S.-L. Zhang, H.-H. Choi, H.-Y. Yue, W.-C. Yang, *Curr. Appl. Phys.* **2014**, *14*, 264-268.

[104] K.-J. Huang, Y.-J. Liu, Y.-M. Liu, L.-L. Wang, *J. Hazard. Mater.* **2014**, *276*, 207-215.

[105] M. Yi, Z. Shen, *J. Mater. Chem. A* **2015**, *3*, 11700-11715.

[106] K. Gacem, M. Boukhicha, Z. Chen, A. Shukla, *Nanotechnol.* **2012**, *23*, 505709.

[107] R. Ganatra, Q. Zhang, *ACS Nano* **2014**, *8*, 4074-4099.

[108] Z. Zeng, Z. Yin, X. Huang, H. Li, Q. He, G. Lu, F. Boey, H. Zhang, *Angew. Chem. Int. Ed.* **2011**, *50*, 11093-11097.

[109] J. N. Coleman, M. Lotya, A. O'Neill, S. D. Bergin, P. J. King, U. Khan, K. Young, A. Gaucher, S. De, R. J. Smith, *Science* **2011**, *331*, 568-571.

[110] A. O'Neill, U. Khan, J. N. Coleman, *Chem. Mater.* **2012**, *24*, 2414-2421.

[111] S. Eigler, *Phys. Chem. Chem. Phys.* **2014**, *16*, 19832-19835.

[112] C. Mattevi, H. Kim, M. Chhowalla, *J. Mater. Chem.* **2011**, *21*, 3324-3334.

[113] Y. Zhang, L. Y. Zhang, C. W. Zhou, *Acc. Chem. Res.* **2013**, *46*, 2329-2339.

[114] Y. Zhan, Z. Liu, S. Najmaei, P. M. Ajayan, J. Lou, *Small* **2012**, *8*, 966-971.

[115] Y.-C. Lin, W. Zhang, J.-K. Huang, K.-K. Liu, Y.-H. Lee, C.-T. Liang, C.-W. Chu, L.-J. Li, *Nanoscale* **2012**, *4*, 6637-6641.

[116] K.-K. Liu, W. Zhang, Y.-H. Lee, Y.-C. Lin, M.-T. Chang, C.-Y. Su, C.-S. Chang, H. Li, Y. Shi, H. Zhang, *Nano lett.* **2012**, *12*, 1538-1544.

[117] S. Wu, C. Huang, G. Aivazian, J. S. Ross, D. H. Cobden, X. Xu, *ACS Nano* **2013**, *7*, 2768-2772.

[118] S. Mizushima, Y. Fujibayashi, K. Shiiki, *J. Phys. Soc. Japan* **1971**, *30*, 299-299.

[119] Y. Fujibayashi, *J. Phys. Soc. Japan* **1973**, *34*, 989-993.

[120] Y. Fujibayashi, S. Mizushima, *J. Phys. Soc. Japan* **1973**, *34*, 281-281.

[121] T. W. Ebbesen, H. Hiura, *Adv. Mater.* **1995**, *7*, 582-586.

[122] Y. Ohashi, T. Koizumi, T. Yoshikawa, T. Hironaka, K. Shiiki, *Tanso* **1997**, *1997*, 235-238.

[123] X. Lu, H. Huang, N. Nemchuk, R. S. Ruoff, *Appl. Phys. Lett.* **1999**, *75*, 193-195.

[124] Y. Gan, W. Chu, L. Qiao, *Surf. Sci.* **2003**, *539*, 120-128.

[125] P. Blake, E. Hill, A. Castro Neto, K. Novoselov, D. Jiang, R. Yang, T. Booth, A. Geim, *Appl. Phys. Lett.* **2007**, *91*, 063124.

[126] S. Roddaro, P. Pingue, V. Piazza, V. Pellegrini, F. Beltram, *Nano lett.* **2007**, *7*, 2707-2710.

[127] K. Novoselov, A. C. Neto, *Phys. Scr.* **2012**, *2012*, 014006.
[128] S. Eigler, A. Hirsch, *Angew. Chem. Int. Ed.* **2014**, *53*, 7720-7738.
[129] H.-J. Butt, K. Graf, M. Kappl, *Physics and chemistry of interfaces*, John Wiley & Sons, **2013**.
[130] C. K. Chua, M. Pumera, *Chem. Soc. Rev.* **2014**, *43*, 291-312.
[131] S. Eigler, M. Enzelberger-Heim, S. Grimm, P. Hofmann, W. Kroener, A. Geworski, C. Dotzer, M. Rockert, J. Xiao, C. Papp, O. Lytken, H. P. Steinruck, P. Muller, A. Hirsch, *Adv. Mater.* **2013**, *25*, 3583-3587.
[132] F. Grote, C. Gruber, F. Boerrnert, U. Kaiser, S. Eigler, *Angew. Chem. Int. Ed.* **2017**, *56*, 9222-9225.
[133] Y. Zhang, L. Zhang, C. Zhou, *Acc. Chem. Res.* **2013**, *46*, 2329-2339.
[134] K. Kim, Y. Zhao, H. Jang, S. Lee, J. Kim, K. Kim, J. Ahn, *Nature* **2009**, *457*, 706.
[135] S. Kwon, C. Ciobanu, V. Petrova, V. Shenoy, *Nano Lett.* **2009**, *9*, 1607-1613.
[136] P. W. Sutter, J.-I. Flege, E. A. Sutter, *Nat. Mater.* **2008**, *7*, 406-411.
[137] J. Coraux, A. T. N 'Diaye, C. Busse, T. Michely, *Nano lett.* **2008**, *8*, 565-570.
[138] X. Li, W. Cai, J. An, S. Kim, J. Nah, D. Yang, R. Piner, A. Velamakanni, I. Jung, E. Tutuc, *Science* **2009**, *324*, 1312-1314.
[139] J.-H. Lee, E. K. Lee, W.-J. Joo, Y. Jang, B.-S. Kim, J. Y. Lim, S.-H. Choi, S. J. Ahn, J. R. Ahn, M.-H. Park, *Science* **2014**, *344*, 286-289.
[140] N. Agenet, O. Buisine, F. Slowinski, V. Gandon, C. Aubert, M. Malacria, *Org. React.* **2004**, *68*, 1-302.
[141] N. KANETA, T. HIRAI, M. MORI, *Chem. Lett.* **1995**, *1995*, 627-628.
[142] G. M. Whitesides, W. J. Ehmann, *J. Am. Chem. Soc.* **1969**, *91*, 3800-3807.
[143] D. R. McAlister, J. E. Bercaw, R. G. Bergman, *J. Am. Chem. Soc.* **1977**, *99*, 1666-1668.
[144] I. Amer, T. Bernstein, M. Eisen, J. Blum, K. P. C. Vollhardt, *J. Mol. Catal.* **1990**, *60*, 313-321.
[145] K. Kirchner, M. J. Calhorda, R. Schmid, L. F. Veiros, *J. Am. Chem. Soc.* **2003**, *125*, 11721-11729.
[146] N. Agenet, V. Gandon, K. P. C. Vollhardt, M. Malacria, C. Aubert, *J. Am. Chem. Soc.* **2007**, *129*, 8860-8871.
[147] J. H. Hardesty, J. B. Koerner, T. A. Albright, G.-Y. Lee, *J. Am. Chem. Soc.* **1999**, *121*, 6055-6067.
[148] B. E. Schilling, R. Hoffmann, D. L. Lichtenberger, *J. Am. Chem. Soc.* **1979**, *101*, 585-591.
[149] R. K. Bansal, *Heterocyclic chemistry*, New Age International, **2008**.
[150] J. B. Wright, *Chem. Rev.* **1951**, *48*, 397-541.
[151] R. S. Keri, A. Hiremathad, S. Budagumpi, B. M. Nagaraja, *Chem. Biol. Drug Des.* **2015**, *86*, 19-65.
[152] Y. Bansal, O. Silakari, *Bioorg. Med. Chem.* **2012**, *20*, 6208-6236.
[153] F. Hobrecker, *Chem. Ges*, *5*, 290.
[154] M. Philips, *J. Chem. Soc.* **1928**, 2393-2399.
[155] V. Fischer, *Ber.* **1905**, *38*, 320.
[156] N. Chandrashekhar, B. Thomas, V. Gayathri, K. V. Ramanathan, N. M. N. Gowda, *Magn. Reson. Chem.* **2008**, *46*, 769-774.
[157] H. Y. Lee, J. Park, M. S. Lah, J. I. Hong, *Chem. Commun.* **2007**, 5013-5015.
[158] J. F. Xiong, S. H. Luo, J. P. Huo, J. Y. Liu, S. X. Chen, Z. Y. Wang, *J. Org. Chem.* **2014**, *79*, 8366-8373.
[159] B. Zhang, Y. Gao, J. L. Li, Z. Shi, *Chinese Chem. Lett.* **2006**, *17*, 1165-1168.

[160] K. C. Ranjeesh, R. Illathvalappil, S. D. Veer, J. Peter, V. C. Wakchaure, Goudappagouda, K. V. Raj, S. Kurungot, S. S. Babu, *J. Am. Chem. Soc.* **2019**, *141*, 14950-14954.
[161] C. C. Johansson Seechurn, M. O. Kitching, T. J. Colacot, V. Snieckus, *Angew. Chem. Int. Ed.* **2012**, *51*, 5062-5085.
[162] E. i. Negishi, *Angew. Chem. Int. Ed.* **2011**, *50*, 6738-6764.
[163] A. Suzuki, *Angew. Chem. Int. Ed.* **2011**, *50*, 6722-6737.
[164] R. Chinchilla, C. Nájera, *Chem. Rev.* **2007**, *107*, 874-922.
[165] A. de Meijere, Handbook of organopalladium chemistry for organic synthesis, John Wiley & Sons, **2003**.
[166] F. Diederich, P. J. Stang, *Metal-catalyzed cross-coupling reactions*, John Wiley & Sons, **2008**.
[167] P. Bertus, F. Fécourt, C. Bauder, P. Pale, *New J. Chem.* 2004, *28*, 12-14.
[168] Accessed 2020-07-01: https://chem.libretexts.org/Bookshelves/Physical_and_Theoretical_Chemistry_Textbook_Maps/Map%3A_Physical_Chemistry_for_the_Biosciences_(Chang)/13%3A_Intermolecular_Forces/13.1%3A_Intermolecular_Interactions
[169] P. A. Kollman, L. C. Allen, *Chem. Rev.* **1972**, *72*, 283-303.
[170] J. Liang, Y. Huang, L. Zhang, Y. Wang, Y. Ma, T. Guo, Y. Chen, *Adv. Funct. Mater.* **2009**, *19*, 2297-2302.
[171] M. A. Rafiee, J. Rafiee, Z. Wang, H. Song, Z.-Z. Yu, N. Koratkar, *ACS Nano* **2009**, *3*, 3884-3890.
[172] T. Ramanathan, A. Abdala, S. Stankovich, D. Dikin, M. Herrera-Alonso, R. D. Piner, D. Adamson, H. Schniepp, X. Chen, R. Ruoff, *Nat. Nanotechnol.* **2008**, *3*, 327-331.
[173] H. Wang, Q. Hao, X. Yang, L. Lu, X. Wang, *ACS Appl. Mater. Interfaces* **2010**, *2*, 821-828.
[174] J. Björk, F. Hanke, C.-A. Palma, P. Samori, M. Cecchini, M. Persson, *J. Phys. Chem. Lett.* **2010**, *1*, 3407-3412.
[175] C. R. Martinez, B. L. Iverson, *Chem. Sci.* **2012**, *3*, 2191-2201.
[176] C. A. Hunter, J. K. Sanders, *J. Am. Chem. Soc.* **1990**, *112*, 5525-5534.
[177] C. A. Hunter, *Philos. Trans. R. Soc. Lond.* **1993**, *345*, 77-85.
[178] P. Chakrabarti, R. Bhattacharyya, *Prog. Biophys. Mol. Bio.* **2007**, *95*, 83-137.
[179] G. B. McGaughey, M. Gagné, A. K. Rappé, *J. Bio.l Chem.* **1998**, *273*, 15458-15463.
[180] J. H. Williams, J. K. Cockcroft, A. N. Fitch, *Angew. Chem. Int. Ed.* **1992**, *31*, 1655-1657.
[181] J. Kim, L. J. Cote, F. Kim, J. Huang, *J. Am. Chem. Soc.* **2010**, *132*, 260-267.
[182] T. Sreeprasad, M. S. Maliyekkal, K. Deepti, K. Chaudhari, P. L. Xavier, T. Pradeep, *ACS Appl. Mater. Interfaces* **2011**, *3*, 2643-2654.
[183] F. Liu, K. S. Choi, T. J. Park, S. Y. Lee, T. S. Seo, *BioChip J.* **2011**, *5*, 123-128.
[184] K. Zhang, S. Yu, B. Jv, W. Zheng, *Phys. Chem. Chem. Phys.* **2016**, *18*, 28418-28427.
[185] S. K. Kolev, H. A. Aleksandrov, V. A. Atanasov, V. N. Popov, T. I. Milenov, *J. Phys. Chem. C* **2019**, *123*, 21448-21456.
[186] P. J. Stang, M. Hanack, L. Subramanian, *Synth.* **1982**, *1982*, 85-126.
[187] H. Meerwein, G. Hinz, P. Hofmann, E. Kroning, E. Pfeil, *Journal für praktische Chemie* **1937**, *147*, 257-285.
[188] H. Meerwein, E. Battenberg, H. Gold, *J. Prakt. Chem.* **1939**, *154*, 83-156.
[189] V. Vij, V. Bhalla, M. Kumar, *Chem. Rev.* **2016**, *116*, 9565-9627.
[190] A. Almenningen, O. Bastiansen, P. Skancke, *Acta Chem. Scand.* **1958**, *12*, 5.
[191] M. D. Watson, A. Fechtenkötter, K. Müllen, *Chem. Rev.* **2001**, *101*, 1267-1300.
[192] P. Herwig, C. W. Kayser, K. Müllen, H. W. Spiess, *Adv. Mater.* **1996**, *8*, 510-513.

[193] A. Stabel, P. Herwig, K. Müllen, J. P. Rabe, *Angew. Chem. Int. Ed.* **1995**, *34*, 1609-1611.

[194] A. Fechtenkötter, K. Saalwächter, M. A. Harbison, K. Müllen, H. W. Spiess, *Angew. Chem. Int. Ed.* **1999**, *38*, 3039-3042.

[195] A. Fechtenkötter, N. Tchebotareva, M. Watson, K. Müllen, *Tetrahedron* **2001**, *57*, 3769-3783.

[196] P. Samorí, A. Fechtenkötter, F. Jäckel, T. Böhme, K. Müllen, J. P. Rabe, *J. Am. Chem. Soc.* **2001**, *123*, 11462-11467.

[197] M. Lee, J.-W. Kim, S. Peleshanko, K. Larson, Y.-S. Yoo, D. Vaknin, S. Markutsya, V. V. Tsukruk, *J. Am. Chem. Soc.* **2002**, *124*, 9121-9128.

[198] R. Bushby, O. Lozman, *Curr. Opin. Solid State Mater. Sci.* **2002**, *6*, 569-578.

[199] H. Seyler, B. Purushothaman, D. J. Jones, A. B. Holmes, W. W. Wong, *Pure Appl. Chem.* **2012**, *84*, 1047-1067.

[200] M. Kastler, W. Pisula, R. J. Davies, T. Gorelik, U. Kolb, K. Müllen, *Small* **2007**, *3*, 1438-1444.

[201] A. Van De Craats, J. Warman, *Adv. Mater.* **1999**, *11*, 1469.

[202] J. P. Hill, W. Jin, A. Kosaka, T. Fukushima, H. Ichihara, T. Shimomura, K. Ito, T. Hashizume, N. Ishii, T. Aida, *Science* **2004**, *304*, 1481-1483.

[203] W. Jin, T. Fukushima, M. Niki, A. Kosaka, N. Ishii, T. Aida, *Proc. Natl. Acad. Sci.* **2005**, *102*, 10801-10806.

[204] T. Emrick, E. Pentzer, *NPG Asia Mater.* **2013**, *5*, e43-e43.

[205] V. S. Iyer, M. Wehmeier, J. D. Brand, M. A. Keegstra, K. Müllen, *Angew. Chem. Int. Ed.* **1997**, *36*, 1604-1607.

[206] V. S. Iyer, K. Yoshimura, V. Enkelmann, R. Epsch, J. P. Rabe, K. Müllen, *Angew. Chem. Int. Ed.* **1998**, *37*, 2696-2699.

[207] M. Müller, C. Kübel, K. Müllen, *Chem. Eur. J.* **1998**, *4*, 2099-2109.

[208] S. Ito, M. Wehmeier, J. D. Brand, C. Kübel, R. Epsch, J. P. Rabe, K. Müllen, *Chem. Eur. J.* **2000**, *6*, 4327-4342.

[209] P. T. Herwig, V. Enkelmann, O. Schmelz, K. Müllen, *Chem. Eur. J.* **2000**, *6*, 1834-1839.

[210] J. Wu, M. D. Watson, L. Zhang, Z. Wang, K. Müllen, *J. Am. Chem. Soc.* **2004**, *126*, 177-186.

[211] D. J. Jones, B. Purushothaman, S. Ji, A. B. Holmes, W. W. Wong, *Chem. Commun.* **2012**, *48*, 8066-8068.

[212] M. M. Martin, M. Dill, J. Langer, N. Jux, *J Org. Chem.* **2018**, *84*, 1489-1499.

[213] F. b. A. de Souza, A. R. Ambrozio, E. S. Souza, D. F. Cipriano, W. L. Scopel, J. C. Freitas, *J. Phys. Chem. C* **2016**, *120*, 27707-27716.

[214] F. Priante, M. Salim, L. Ottaviano, F. Perrozzi, *Nanotechnol.* **2018**, *29*, 075704.

[215] M. S. Dresselhaus, A. Jorio, R. Saito, *Annu. Rev. Condens. Matter Phys., Vol 1* **2010**, *1*, 89-108.

[216] J.-B. Wu, M.-L. Lin, X. Cong, H.-N. Liu, P.-H. Tan, *Chem. Soc. Rev.* **2018**, *47*, 1822-1873.

[217] A. C. Ferrari, D. M. Basko, *Nat. Nanotechnol.* **2013**, *8*, 235.

[218] A. C. Ferrari, *Solid State Comm.* **2007**, *143*, 47-57.

[219] C. Musumeci, *Crystals* **2017**, *7*, 216.

[220] R. R. Ernst, *Angew. Chem. Int. Ed.* **1992**, *31*, 805-823.

[221] D. I. Hoult, B. Bhakar, *Concepts Magn.Reson.* **1997**, *9*, 277-297.

[222] R. M. Silverstein, G. C. Bassler, *J. Chem. Educ.* **1962**, *39*, 546.

[223] A. Milani, M. Tommasini, V. Russo, A. L. Bassi, A. Lucotti, F. Cataldo, C. S. Casari, *Beilstein J. Nanotechnol.* **2015**, *6*, 480-491.

[224] A. C. Ferrari, J. Meyer, V. Scardaci, C. Casiraghi, M. Lazzeri, F. Mauri, S. Piscanec, D. Jiang, K. Novoselov, S. Roth, *Phys. Rev. lett.* **2006**, *97*, 187401.

[225] F. Tuinstra, J. L. Koenig, *J. Chem. Phys.* **1970**, *53*, 1126-1130.

[226] J. W. Ager III, D. K. Veirs, G. M. Rosenblatt, *Phys. Rev. B* **1991**, *43*, 6491.

[227] M. S. Dresselhaus, A. Jorio, M. Hofmann, G. Dresselhaus, R. Saito, *Nano lett.* **2010**, *10*, 751-758.

[228] A. C. Ferrari, J. Robertson, *Phys. Rev. B* **2000**, *61*, 14095.

[229] E. M. Ferreira, M. V. Moutinho, F. Stavale, M. M. Lucchese, R. B. Capaz, C. A. Achete, A. Jorio, *Phys. Rev. B* **2010**, *82*, 125429.

[230] A. Das, S. Pisana, B. Chakraborty, S. Piscanec, S. K. Saha, U. V. Waghmare, K. S. Novoselov, H. R. Krishnamurthy, A. K. Geim, A. C. Ferrari, A. K. Sood, *Nat. Nanotechnol.* **2008**, *3*, 210-215.

[231] P. Vecera, J. C. Chacón-Torres, T. Pichler, S. Reich, H. R. Soni, A. Görling, K. Edelthalhammer, H. Peterlik, F. Hauke, A. Hirsch, *Nat. Commun.* **2017**, *8*, 1-9.

[232] X. Wu, G. Siu, S. Tong, X. Liu, F. Yan, S. Jiang, X. Zhang, D. Feng, *Appl. Phys. Lett.* **1996**, *69*, 523-525.

[233] P. A. Temple, C. Hathaway, *Phys. Rev. B* **1973**, *7*, 3685.

[234] M. M. Khayyat, G. K. Banini, D. G. Hasko, M. M. Chaudhri, *J. Phys. D: Appl. Phys.* **2003**, *36*, 1300.

[235] K. Uchinokura, T. Sekine, E. Matsuura, *Solid State Commun.* **1972**, *11*, 47-+.

[236] R. Saito, M. Hofmann, G. Dresselhaus, A. Jorio, M. Dresselhaus, *Adv. Phys***2011**, *60*, 413-550.

[237] A. C. Ferrari, *Solid State Commun.* **2007**, *143*, 47-57.

[238] S. Eigler, F. Hof, M. Enzelberger-Heim, S. Grimm, P. Muller, A. Hirsch, *J. Phys. Chem. C* **2014**, *118*, 7698-7704.

[239] S. Eigler, F. Hof, M. Enzelberger-Heim, S. Grimm, P. Müller, A. Hirsch, *J. Phys. Chem. C* **2014**, *118*, 7698-7704.

[240] L. G. Cançado, A. Jorio, E. M. Ferreira, F. Stavale, C. A. Achete, R. B. Capaz, M. V. d. O. Moutinho, A. Lombardo, T. Kulmala, A. C. Ferrari, *Nano lett.* **2011**, *11*, 3190-3196.

[241] H. Li, Q. Zhang, C. C. R. Yap, B. K. Tay, T. H. T. Edwin, A. Olivier, D. Baillargeat, *Adv. Funct. Mater.* **2012**, *22*, 1385-1390.

[242] J. Verble, T. Wieting, *Phys. Rev. lett.* **1970**, *25*, 362.

[243] J. Chen, C. Wang, *Solid State Commun.* **1974**, *14*, 857-860.

[244] A. Bagnall, W. Liang, E. Marseglia, B. Welber, *Phys. B+ C* **1980**, *99*, 343-346.

[245] M. Viršek, A. Jesih, I. Milošević, M. Damnjanović, M. Remškar, *Surf. Sci.* **2007**, *601*, 2868-2872.

[246] B. C. Windom, W. Sawyer, D. W. Hahn, *Tribology Letters* **2011**, *42*, 301-310.

[247] P. Bertrand, *Phys. Rev. B* **1991**, *44*, 5745.

[248] S.-L. Li, H. Miyazaki, H. Song, H. Kuramochi, S. Nakaharai, K. Tsukagoshi, *ACS Nano* **2012**, *6*, 7381-7388.

[249] M. Seah, *Surf. Interface Anal.* **1980**, *2*, 222-239.

[250] T. Susi, T. Pichler, P. Ayala, *Beilstein J. Nanotechnol.* **2015**, *6*, 177-192.

[251] K. Prince, I. Ulrych, M. Peloi, B. Ressel, V. Chab, C. Crotti, C. Comicioli, *Phys. Rev. B* **2000**, *62*, 6866.

[252] G. Speranza, L. Minati, M. Anderle, *J.Appl. Phys.* **2007**, *102*, 043504.

[253] K. Emtsev, F. Speck, T. Seyller, L. Ley, J. D. Riley, *Phys. Rev. B* **2008**, *77*, 155303.

[254] C. K. Chua, M. Pumera, *Chem. Eur. J.* **2013**, *19*, 2005-2011.

[255] T. I. T. Okpalugo, P. Papakonstantinou, H. Murphy, J. McLaughlin, N. M. D. Brown, *Carbon* **2005**, *43*, 153-161.

[256] W. F. S. J. F. Moulder, P. E. Sobol and K. D. Bomben, *Perkin-Elmer Corp., Norwalk* **1995**.

[257] D. Choudhury, B. Das, D. D. Sarma, C. N. R. Rao, *Chem. Phys. Lett.* **2010**, *497*, 66-69.

[258] C. Tengstedt, M. Unge, M. P. de Jong, S. Stafstrom, W. R. Salaneck, M. Fahlman, *Phys. Rev. B* **2004**, *69*.

[259] D. Choudhury, B. Das, D. Sarma, C. Rao, *Chem. Phys. Lett.* **2010**, *497*, 66-69.

[260] L. Valade, J. Fraxedas, D. de Caro, J. P. Savy, I. Malfant, C. Faulmann, M. Almeida, *J. Low Temp. Phys.* **2006**, *142*, 141-146.

[261] C. Bellitto, M. Bonamico, V. Fares, P. Imperatori, S. Patrizio, *J. Chem. Soc.* **1989**, 719-727.

[262] J. C. Vickerman, D. Briggs, *Tof-SIMS: materials analysis by mass spectrometry*, im publications, **2013**.

[263] L. Przybilla, J.-D. Brand, K. Yoshimura, H. J. Räder, K. Müllen, *Anal. Chem.* **2000**, *72*, 4591-4597.

[264] J. Wu, A. Fechtenkötter, J. Gauss, M. D. Watson, M. Kastler, C. Fechtenkötter, M. Wagner, K. Müllen, *J. Am. Chem. Soc.* **2004**, *126*, 11311-11321.

[265] A. J. Bard, L. R. Faulkner, Wiley, New York, **1980**.

[266] D. Gosser, *New York* **1993**.

[267] J. F. Rusling, S. L. Suib, *Adv. Mater.* **1994**, *6*, 922-930.

[268] P. Zanello, C. Nervi, F. F. De Biani, *Inorg. Electrochem: theory, practice and application*, Royal Society of Chemistry, **2011**.

[269] P. Song, A. C. Fisher, J. D. Wadhawan, J. J. Cooper, H. J. Ward, N. S. Lawrence, *RSC Adv.* **2016**, *6*, 70237-70242.

[270] J. M. Hollas, *Modern spectroscopy*, John Wiley & Sons, **2004**.

[271] C. F. Klingshirn, *Semiconductor optics*, Springer Science & Business Media, **2012**.

[272] J. R. Lakowicz, *Principles of fluorescence spectroscopy*, Springer Science & Business Media, **2013**.

[273] A. Splendiani, L. Sun, Y. Zhang, T. Li, J. Kim, C.-Y. Chim, G. Galli, F. Wang, *Nano lett.* **2010**, *10*, 1271-1275.

[274] K. F. Mak, C. Lee, J. Hone, J. Shan, T. F. Heinz, *Phys. Rev. lett.* **2010**, *105*, 136805.

[275] S. Catalán-Gómez, S. Garg, A. Redondo-Cubero, N. Gordillo, A. de Andrés, F. Nucciarelli, S. Kim, P. Kung, J. L. Pau, *Nanoscale Adv.* **2019**, *1*, 884-893.

[276] G. Binnig, C. F. Quate, C. Gerber, *Phys. Rev. Lett.* **1986**, *56*, 930.

[277] M. R. Grimmett, *Imidazole and benzimidazole synthesis*, Academic press, **1997**.

[278] L. Yong, H. Butenschön, *Chem. Commun.* **2002**, 2852-2853.

[279] W. Dilthey, W. Schommer, W. Höschen, H. Diedrichs, *Ber. Dtsch. Chem Ges.* **1935**, *68*, 1159-1162.

[280] D. Lungerich, D. Reger, H. Hoelzel, R. Riedel, M. M. Martin, F. Hampel, N. Jux, *Angew. Chem. Int. Ed.* **2016**, *55*, 5602-5605.

[281] P. Rietsch, J. Soyka, S. Brülls, J. Er, K. Hoffmann, J. Beerhues, B. Sarkar, U. Resch-Genger, S. Eigler, *Chem. Commun.* **2019**, *55*, 10515-10518.

[282] R. Scholl, J. Mansfeld, *Ber. Dtsch. Chem Ges.* **1910**, *43*, 1734-1746.

[283] G. Kränzlein, **1932**.

[284] C. A. Thomas, **1941**.

[285] L. Bratz, S. Von Niementowski, *Ber. Dtsch. Chem Ges.* **1919**, *52*, 189-194.

[286] K. Kobayashi, N. Kobayashi, M. Ikuta, B. Therrien, S. Sakamoto, K. Yamaguchi, *J. Org. Chem.* **2005**, *70*, 749-752.

[287] B. Zhu, H. Chen, W. Lin, Y. Ye, J. Wu, S. Li, *J. Am. Chem. Soc.* **2014**, *136*, 15126-15129.

[288] M. Hoffmann, J. Kärnbratt, M. H. Chang, L. M. Herz, B. Albinsson, H. L. Anderson, *Angew. Chem. Int. Ed.* **2008**, *47*, 4993-4996.
[298] P. T. Nguyen, H. T. Nguyen, H. Q. Pham, J. Kim, K. E. Cordova, H. Furukawa, *Inorg. Chem.* **2015**, *54*, 10065-10072.
[290] T. Gadzikwa, G. Lu, C. L. Stern, S. R. Wilson, J. T. Hupp, S. T. Nguyen, *Chem. Commun.* **2008**, 5493-5495.
[291] K. Kobayashi, T. Shirasaka, E. Horn, N. Furukawa, *Tetrahedron Lett.* **2000**, *41*, 89-93.
[292] F. J. Zúniga, L. Palatinus, P. Cabildo, R. M. Claramunt, J. Elguero, *Z. Krist.-Cryst. Mater.* **2006**, *221*, 281-287.
[293] H. Y. Lee, J. Park, M. S. Lah, J.-I. Hong, *Chem. Commun.* **2007**, 5013-5015.
[294] S. M. Brülls, V. Cantatore, Z. Wang, P. L. Tam, P. Malmberg, J. Stubbe, B. Sarkar, I. Panas, J. Mårtensson, S. Eigler, *Chem. Eur. J.* **2020**, *26*, 6694-6702.
[295] R. Feng, L. Li, B. Li, J. Li, D. Peng, Y. Yu, Q. Mu, N. Zhao, X. Yu, Z. Wang, *New J. Chem.* **2018**, *42*, 14325-14331.
[296] J. P. Perdew, K. Burke, M. Ernzerhof, *Phys. Rev. lett.* **1996**, *77*, 3865.
[297] J. Mei, Y. Hong, J. W. Lam, A. Qin, Y. Tang, B. Z. Tang, *Adv. Mater.* **2014**, *26*, 5429-5479.
[298] C. Reichardt, *Chem. Rev.* **1994**, *94*, 2319-2358.
[299] H. Mustroph, S. Ernst, B. Senns, A. D. Towns, *Color. Technol.* **2015**, *131*, 9-26.
[300] J. J. Murray, R. F. Pottie, C. Pupp, *Can. J.Chem.* **1974**, *52*, 557-563.
[301] C. J. Shearer, A. D. Slattery, A. J. Stapleton, J. G. Shapter, C. T. Gibson, *Nanotechnol.* **2016**, *27*, 125704.
[302] E. V. Basiuk, M. Martínez-Herrera, E. Álvarez-Zauco, L. V. Henao-Holguín, I. Puente-Lee, V. A. Basiuk, *Dalton Transactions* **2014**, *43*, 7413-7428.
[303] E.-Y. Choi, T. H. Han, J. Hong, J. E. Kim, S. H. Lee, H. W. Kim, S. O. Kim, *J. Mater. Chem.* **2010**, *20*, 1907-1912.
[304] V. Valeš, K. Drogowska-Horná, V. L. Guerra, M. Kalbáč, *Sci. Rep.* **2020**, *10*, 1-9.
[305] S. Najmaei, X. Zou, D. Er, J. Li, Z. Jin, W. Gao, Q. Zhang, S. Park, L. Ge, S. Lei, *Nano Lett.* **2014**, *14*, 1354-1361.
[306] C. J. Lockhart de la Rosa, R. Phillipson, J. Teyssandier, J. Adisoejoso, Y. Balaji, C. Huyghebaert, I. Radu, M. Heyns, S. De Feyter, S. De Gendt, *Appl. Phys. Lett.* **2016**, *109*, 253112.
[307] L. Sun, H. Hu, D. Zhan, J. Yan, L. Liu, J. S. Teguh, E. K. Yeow, P. S. Lee, Z. Shen, *small* **2014**, *10*, 1090-1095.
[308] M. P. Seah, *Vacuum* **1984**, *34*, 463-478.
[309] D. Q. Yang, E. Sacher, *Surf. Sci.* **2003**, *531*, 185-198.
[310] L. P. Mawlong, A. Bora, P. Giri, *Sci. Rep.* **2019**, *9*, 1-14.